Winter 2015

Laser scanner jitter characterization, page content analysis for optimal rendering, and understanding image graininess

Yi-Ting Chen
Purdue University

Graduate School Form 30
(Updated 11/20/2014)

PURDUE UNIVERSITY
GRADUATE SCHOOL
Thesis/Dissertation Acceptance

This is to certify that the thesis/dissertation prepared

By Yi-Ting Chen

Entitled
Laser Scanner Jitter Characterization, Page Content Analysis for Optimal Rendering, and Understanding Image Graininess

For the degree of Doctor of Philosophy

Is approved by the final examining committee:

Jan P. Allebach

GEORGE T. CHIU

MARY L. COMER

MIREILLE BOUTIN

To the best of my knowledge and as understood by the student in the Thesis/Dissertation Agreement, Publication Delay, and Certification/Disclaimer (Graduate School Form 32), this thesis/dissertation adheres to the provisions of Purdue University's "Policy on Integrity in Research" and the use of copyrighted material.

Jan P. Allebach

Approved by Major Professor(s): _____

_____

Approved by: Michael R. Melloch 02/04/2015

Head of the Department Graduate Program Date

LASER SCANNER JITTER CHARACTERIZATION, PAGE CONTENT ANALYSIS FOR OPTIMAL RENDERING, AND UNDERSTANDING IMAGE GRAININESS

A Dissertation

Submitted to the Faculty

of

Purdue University

by

Yi-Ting Chen

In Partial Fulfillment of the

Requirements for the Degree

of

Doctor of Philosophy

May 2015

Purdue University

West Lafayette, Indiana

[To Dad, Mom, Jia-Hsuan and Andre.]

ACKNOWLEDGMENTS

I would like to express my gratitude to the people that are significant to me while pursuing my PhD at Purdue University. First of all, I deeply express my sincere gratitude to my major advisor, Prof. Jan P. Allebach. His patience, encouragement, and advice guided me through my PhD life at Purdue. As a student of Prof. Allebach is a great turning point in my life, and it is also my great honor to be his student. Next, I also want to thank my committee members Prof. Mireille Boutin, Prof. Mary Comer and Prof. George Chiu as well for their advice and careful guidance.

I would like express my highest gratitude to my dad and mom for their endless love and patience. Without their support, I will not be at Purdue to pursue my degree. In addition, I would like to express my deeply gratitude to my wife, Jia-Hsuan. She is the most important person while studying at Purdue. She shared the most of delightful and hard times with me at Purdue. The life at Purdue is also an eyewitness of our love where we met, married and had our son.

I also would like to thank to my EISL colleagues for their support. Finally, I want to thank Hewlett-Packard Company for the support during my Ph.D. study at Purdue.

TABLE OF CONTENTS

Page

LIST OF TABLES

LIST OF FIGURES

Figure Page

Figure Page

Figure Page

Figure Page

Figure Page

ABBREVIATIONS

OPC	optical photoconductive drum
CSFT	continuous-space Fourier transform
DSFT	discrete space Fourier transform
EP	electrophotographic
RIP	raster image processor
PDL	page description language
MAP	maximum a posteriori
PWM	pulse width modulation
OCR	optical character recognition
PIP	Photo imaging plate
BSB	Basic screen block
HVS	Human visual system
DFT	Discrete Fourier transform
IDFT	Inverse discrete Fourier transform
CAT	Chromatic adaption transformation

ABSTRACT

Chen, Yi-Ting Ph.D., Purdue University, May 2015. Laser Scanner Jitter Characterization, Page Content Analysis for Optimal Rendering, and Understanding Image Graininess. Major Professor: Jan P. Allebach.

In Chapter 1, the electrophotographic (EP) process is widely used in imaging systems such as laser printers and office copiers. In the EP process, laser scanner jitter is a common artifact that mainly appears along the scan direction due to the condition of polygon facets. Prior studies have not focused on the periodic characteristic of laser scanner jitter in terms of the modeling and analysis. This chapter addresses the periodic characteristic of laser scanner jitter in the mathematical model. In the Fourier domain, we derive an analytic expression for laser scanner jitter in general, and extend the expression assuming a sinusoidal displacement. This leads to a simple closed-form expression in terms of Bessel functions of the first kind. We further examine the relationship between the continuous-space halftone image and the periodic laser scanner jitter. The simulation results show that our proposed mathematical model predicts the phenomenon of laser scanner jitter effectively, when compared to the characterization using a test pattern, which consists of a flat field with 25% dot coverage However, there is some mismatches between the analytical spectrum and spectrum of the processed scanned test target. We improve experimental results by directly estimating the displacement instead of assuming a sinusoidal displacement. This gives a better prediction of the phenomenon of laser scanner jitter.

In Chapter 2, we describe a segmentation-based object map correction algorithm, which can be integrated in a new imaging pipeline for laser electrophotographic (EP) printers. This new imaging pipeline incorporates the idea of object-oriented halftoning, which applies different halftone screens to different regions of the page, to im-

prove the overall print quality. In particular, smooth areas are halftoned with a low-frequency screen to provide more stable printing; whereas detail areas are halftoned with a high-frequency screen, since this will better reproduce the object detail. In this case, the object detail also serves to mask any print defects that arise from the use of a high frequency screen. These regions are defined by the initial object map, which is translated from the page description language (PDL). However, the information of object type obtained from the PDL may be incorrect. Some smooth areas may be labeled as raster causing them to be halftoned with a high frequency screen, rather than being labeled as vector, which would result in them being rendered with a low frequency screen. To correct the misclassification, we propose an object map correction algorithm that combines information from the incorrect object map with information obtained by segmentation of the continuous-tone RGB rasterized page image. Finally, the rendered image can be halftoned by the object-oriented halftoning approach, based on the corrected object map. Preliminary experimental results indicate the benefits of our algorithm combined with the new imaging pipeline, in terms of correction of misclassification errors.

In Chapter 3, we describe a study to understand image graininess. With the emergence of the high-end digital printing technologies, it is of interest to analyze the nature and causes of image graininess in order to understand the factors that prevent high-end digital presses from achieving the same print quality as commercial offset presses. We want to understand how image graininess relates to the halftoning technology and marking technology. This chapter provides three different approaches to understand image graininess. First, we perform a Fourier-based analysis of regular and irregular periodic, clustered-dot halftone textures. With high-end digital printing technology, irregular screens can be considered since they can achieve a better approximation to the screen sets used for commercial offset presses. This is due to the fact that the elements of the periodicity matrix of an irregular screen are rational numbers, rather than integers, which would be the case for a regular screen. From the analytical results, we show that irregular halftone textures generate new

frequency components near the spectrum origin; and these frequency components are low enough to be visible to the human viewer. However, regular halftone textures do not have these frequency components. In addition, we provide a metric to measure the nonuniformity of a given halftone texture. The metric indicates that the nonuniformity of irregular halftone textures is higher than the nonuniformity of regular halftone textures. Furthermore, a method to visualize the nonuniformity of given halftone textures is described. The analysis shows that irregular halftone textures are grainier than regular halftone textures. Second, we analyze the regular and irregular periodic, clustered-dot halftone textures by calculating three spatial statistics. First, the disparity between lattice points generated by the periodicity matrix, and centroids of dot clusters are considered. Next, the area of dot clusters in regular and irregular halftone textures is considered. Third, the compactness of dot clusters in the regular and irregular halftone textures is calculated. The disparity of between centroids of irregular dot clusters and lattices points generated by the irregular screen is larger than the disparity of between centroids of regular dot clusters and lattices points generated by the regular screen. Irregular halftone textures have higher variance in the histogram of dot-cluster area. In addition, the compactness measurement shows that irregular dot clusters are less compact than regular dot clusters. But, a clustered-dot halftone algorithm wants to produce clustered-dot as compact as possible. Lastly, we exam the current marking technology by printing the same halftone pattern on different substrates, glossy and polyester media. The experimental results show that the current marking technology provides better print quality on glossy media than on polyester media. With above three different approaches, we conclude that the current halftoning technology introduces image graininess in the spatial domain because of the non-integer elements in the periodicity matrix of the irregular screen and the finite addressability of the marking engine. In addition, the geometric characteristics of irregular dot clusters is more irregular than the geometric characteristics of regular dot clusters. Finally, the marking technology provides inconsistency of print quality between substrates.

1. LASER SCANNER JITTER CHARACTERIZATION

1.1 Introduction

The electrophotographic (EP) process is widely used in imaging systems, such as laser printers and office copiers. It can be categorized into six basic steps: charging, exposure, development, transfer, fusing, and cleaning. Fig 1.1 shows the architecture of EP process. The diode laser emits the pulsed laser beam controlled by the formatter. The pulsed laser beam is exposed onto the optical photoconductive drum (OPC), which is electro-statically charged by a charged roller, and that beam then scans through the spinning polygon mirror facet. The charges of the OPC surface are then discharged according to the target image. Subsequently, the toner is attached to the OPC surface where areas exposed by the laser beam are discharged. The roller conveys the developed image onto the output media (such as paper), and the output media are transferred to the fuser where they are fused with the toner particles by heat and pressure. Finally, the OPC and rollers are cleaned for the next page to be printed [1].

In the EP process, the overall print quality is determined by the stability of the imaging process. Different mechanical issues contribute to various image artifacts such as fine-pitch banding and laser scanner jitter. Fine-pitch banding is analogous to laser scanner jitter. The only difference being in the direction in which it occurs: fine-pitch banding is due to fluctuations in the process direction, and laser scanner jitter is due to fluctuations in the scan direction. Fine-pitch banding has been widely studied [2–5]. However, little work has been done on laser scanner jitter in terms of a characterization and analysis that exploits its periodic nature.

A few studies on laser scanner jitter have focused on its root cause [6], ways to reduce it [7], and its characterization [8,9]. Horikawa et al [6] demonstrated that laser

scanner jitter has two typical root causes: rotational variation of the spindle motor and the condition of the facets of the polygon mirror. The first cause is directly related to the rotation speed of the polygon mirror. Therefore, the non-regular variation of the spindle motor influences the low-frequency jitter components in the frequency domain. On the other hand, the condition of the facets of the polygon mirror introduces high-frequency jitter components [6]. Horikawa et al. demonstrated that the high-frequency jitter components were essentially caused by the radius variation of the mirror facets and the curve of the mirror facets [6]. To reduce the effect of laser scanner jitter, Stutz presented a pixel placement correction system, which contains an encoder or clock track to examine the position of the scanner [7].

As for the characterization aspect, Eid et al [8, 9] proposed a characterization method that combined two-dimensional analysis of Gabor pre-filtering to detect and localize the artifacts, and spectral analysis. However, the root cause in [8, 9] is due to oscillatory disturbances of the OPC drum and developer roller. This is different from the causes of the jitter examined in the papers [6, 7]. Most importantly, Eid et al [8, 9] did not investigate the periodic characteristic of laser scanner jitter in their analysis.

In this chapter, we focus on laser scanner jitter that is periodic, since the jitter we consider is introduced by the condition of the polygon mirror facets, as discussed in [6, 7]. We present a new method for characterizing the Fourier spectrum of the periodic laser scanner jitter. We view the image as a two-dimensional signal, which has a periodic displacement in the scan direction, and derive an analytic expression for its Fourier spectrum. The laser scanner jitter phenomenon and its periodic characteristic are illustrated in Fig. 1.2. In Fig. 1.2, straight lines are printed along the process direction. However, they appear to be wiggly lines instead of straight lines; and we can clearly see the periodic characteristic of the laser scanner jitter. The length of each straight line is 100 printer-addressable pixels or printer scan lines; and the periodic pattern repeats every 10 pixels because the polygon mirror in our target laser printer has 10 facets. Guided by the periodicity of the jitter pattern, we incorporate this

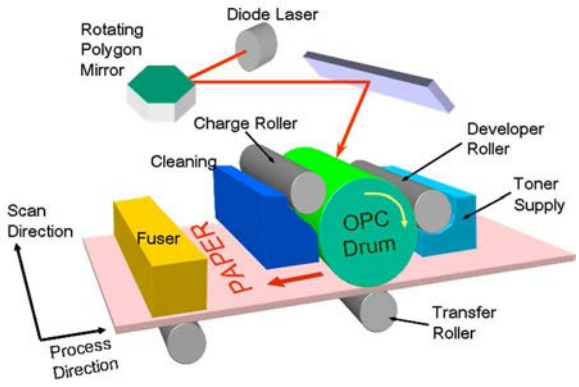

Fig. 1.1. Architecture of a typical electrophotographic printer. [1]

characteristic into our mathematical model to more accurately capture the behavior of laser scanner jitter. A brief description of our work can be found in [10]. In this article, it is illustrated with much more details, and it provides a new approach to improve the experimental result.

In this chapter, we mainly focus on characterizing the behavior of the laser scanner jitter, and do not provide a solution to reducing the impact of the jitter in the EP process. The rest of this paper is organized as follows. The next section describes the mathematical model of laser scanner jitter, and then extends the model to the special case where the periodic displacement is a sinusoidal function in Section 1.3. Then, we investigate in the Fourier domain the relationship between the halftone image and the periodic laser scanner jitter in Section 1.4. In Section 1.5, we present an evaluation of the mathematical model. In Section 1.6, we provide a new approach to improve our mathematical model to better predict the phenomenon of laser scanner jitter. Finally, we conclude in the Section 1.7.

1.2 Mathematical Model of Laser Scanner Jitter

We first develop the general mathematical model of periodic laser scanner jitter in a two-dimensional continuous-space for a continuous-tone image, and extend it to the special case of a sinusoidal displacement in the next section. We denote the

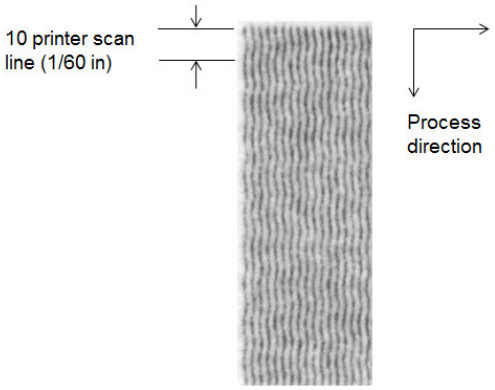

Fig. 1.2. Straight lines printed in the process direction appear to be wiggly instead of straight. The length of each straight line is 100 printer-addressable pixels, and the periodic pattern repeats every 10 pixels because the polygon mirror in our target laser printer has 10 facets. The printer resolution is 600 dpi.

continuous-tone image by $f(x, y)$. Here x corresponds to the process (vertical) direction, and y corresponds to the scan (horizontal) direction. We define a new image $g(x, y)$, with periodic laser scanner jitter, according to

$$g(x, y) \;=\; f\big(x, y - d(x)\big)\,, \tag{1.1}$$

where the displacement $d(x)$ is periodic in x. Let $F(u, v)$ denote the two-dimensional Continuous-Space Fourier Transform (CSFT) of $f(x, y)$ defined according to

$$F(u, v) \;=\; \int_{-\infty}^{+\infty} \int_{-\infty}^{+\infty} f(x, y) e^{-j2\pi(ux+vy)} \mathrm{d}x\,. \tag{1.2}$$

The CSFT $G(u, v)$ of $g(x, y)$ is defined similarly. To derive a closed form expression for $G(u, v)$ in terms of $F(u, v)$, we use the separability of the CSFT. Namely, we use the fact that $G(u, v)$ can be realized as a one-dimensional CSFT with respect to the y coordinate followed by a one-dimensional CSFT with respect to the x coordinate. Thus we can write

$$\widetilde{F}(x, v) \;=\; \int_{-\infty}^{+\infty} f(x, y) e^{-j2\pi vy} \mathrm{d}y\,. \tag{1.3}$$

$$F(u, v) \;=\; \int_{-\infty}^{+\infty} \widetilde{F}(x, v) e^{-j2\pi ux} \mathrm{d}x\,. \tag{1.4}$$

Applying this idea to Eq. (1.1), we obtain

$$\begin{aligned} \widetilde{G}(x, v) \;&=\; \int_{-\infty}^{+\infty} f\big(x, y - d(x)\big) e^{-j2\pi vy} \mathrm{d}y \\ &=\; \widetilde{F}(x, v) e^{-j2\pi v d(x)}\,, \end{aligned} \tag{1.5}$$

where we have used the shifting property of the one-dimensional Fourier transform. Let

$$c(x; v) \;=\; e^{-j2\pi v d(x)}\,. \tag{1.6}$$

It follows from the periodicity of $d(x)$ that $c(x; v)$ is also periodic in x with period X. Thus, Eq. (1.6) can be expressed as a Fourier series

$$c(x; v) \;=\; \sum_{k=-\infty}^{\infty} C_k(v) e^{j2\pi kx/X}\,, \tag{1.7}$$

where the Fourier coefficients are given by

$$\begin{aligned} C_k(v) &= \frac{1}{X}\int_{-\frac{X}{2}}^{+\frac{X}{2}} c(x;v)e^{-j2\pi kx/X}\mathrm{d}x \\ &= \frac{1}{X}\int_{-\frac{X}{2}}^{+\frac{X}{2}} e^{-j2\pi kx/X}e^{-j2\pi vd(x)}\mathrm{d}x \\ &= \frac{1}{X}\int_{-\frac{X}{2}}^{+\frac{X}{2}} e^{-j2\pi\left(kx/X+vd(x)\right)}\mathrm{d}x\,. \end{aligned} \tag{1.8}$$

Now, completing the Fourier transform of $g(x,y)$, we obtain

$$\begin{aligned} G(u,v) &= \int_{-\infty}^{+\infty} \widetilde{G}(x,v)e^{-j2\pi ux}\mathrm{d}x \\ &= \int_{-\infty}^{+\infty} \widetilde{F}(x,v)e^{-j2\pi vd(x)}e^{-j2\pi ux}\mathrm{d}x \\ &= \int_{-\infty}^{+\infty} \widetilde{F}(x,v)\sum_{k=-\infty}^{\infty} C_k(v)e^{j2\pi kx/X}e^{-j2\pi ux}\,. \end{aligned} \tag{1.9}$$

Interchanging integration and summation in the last line of Eq. (1.9), we get

$$\begin{aligned} G(u,v) &= \sum_{k=-\infty}^{\infty} C_k(v)\int_{-\infty}^{+\infty} \widetilde{F}(x,v)e^{-j2\pi(u-k/X)x} \\ &= \sum_{k=-\infty}^{\infty} C_k(v)F\left(u-k/X,v\right)\,. \end{aligned} \tag{1.10}$$

From Eq. (1.10), we see that the periodic laser scanner jitter causes replication of the spectrum $F(u,v)$ of the original image in the process (u) frequency direction with interval $\frac{1}{X}$, which is the reciprocal of the period of the jitter. Each replication is weighted differently by a function that varies in the scan (v) frequency direction. Specifically, the k-th replication is weighted by $C_k(v)$, which is given by Eq. (1.7).

Letting

$$b(x;v) = \frac{1}{X}e^{-j2\pi vd(x)}rect\left(x/X\right)\,, \tag{1.11}$$

we can write

$$C_k(v) = \widetilde{B}\left(k/X;v\right)\,, \tag{1.12}$$

where the k-th weighting function $C_k(v)$ is the 1–D CSFT $\widetilde{B}(u;v)$ of $b(x;v)$ with respect to x, evaluated at frequency $u = \frac{k}{X}$. Note that $b(x;v)$ is complex-valued. Therefore, in general, $\widetilde{B}(u;v)$ will have no particular symmetry with respect to u.

The function $b(x;v)$ has the form of a frequency modulation (FM) signal with zero carrier frequency. The spectral properties of FM signals have been well studied, and can be delineated into two categories – wideband or narrowband, according to the magnitude of the frequency deviation, which here is proportional to the parameter, i.e., the horizontal frequency. In general, there is no simple closed form expression for the FM spectrum in terms of the modulated baseband signal. However, for the special case where the baseband signal is a sinusoid, i.e., $d(x) = \sin(2\pi x/X)$, the spectrum can be written in terms of Bessel functions [11].

1.3 Periodic Laser Scanner Jitter with Sinusoidal Displacement

In this section, we extend the model to the special case where the periodic displacement is a sinusoid function $d(x) = A\sin(2\pi x/X)$. Here A is a constant scale factor that is the peak jitter displacement, and X is the period of the laser scanner jitter. With an approach similar to that used in the previous section, we can derive the Fourier coefficients. Applying this idea to Eq. (1.6), we obtain

$$c(x;v) = e^{-j2\pi Av\sin(2\pi x/X)}\,. \tag{1.13}$$

We express Eq. (1.13) as a Fourier series and we have

$$e^{-j2\pi Av\sin(2\pi x/X)} \;=\; \sum_{k=-\infty}^{\infty} C_k(v)e^{j2\pi kx/X}\,, \tag{1.14}$$

where the Fourier coefficients are given by

$$\begin{aligned} C_k(v) &= \frac{1}{X}\int_{-\frac{X}{2}}^{+\frac{X}{2}} c(x;v)e^{-j2k\pi x/X}\mathrm{d}x \\ &= \frac{1}{X}\int_{-\frac{X}{2}}^{+\frac{X}{2}} e^{-j2\pi Av\sin(2\pi x/X)}e^{-j2k\pi x/X}\mathrm{d}x \\ &= \frac{1}{X}\int_{-\pi}^{+\pi} e^{(-j2\pi Av)(\sin z)}e^{-jkz}\,(X/2\pi)\,\mathrm{d}z \\ &= \frac{1}{2\pi}\int_{-\pi}^{+\pi} e^{\left(j(-2\pi Av)(\sin z)-kz\right)}\mathrm{d}z \\ &= J_k(-2\pi Av)\,, \end{aligned} \tag{1.15}$$

where the Fourier coefficients are articulated by the k-th order Bessel function of the first kind [11].

To obtain the Fourier transform of $g(x, y)$, we substitute Eq. (1.15) into Eq. (1.10), yielding

$$G(u,v) = \sum_k J_k(-2\pi Av)F(u-k/X,v)\,. \tag{1.16}$$

In Eq. (1.16), the periodic laser scanner jitter introduces replications in the process (u) frequency direction with interval $\frac{1}{X}$. Each replication is weighted by the k-th order Bessel function, $J_k(-2\pi Av)$, that changes in the scan (v) frequency direction. The key difference between Eq. (1.10) and Eq. (1.16) is because of the sinusoidal displacement; and we can derive a closed form for Fourier series coefficients, which is the k-th order Bessel function.

To illustrate the structure of the spectrum given by Eq. (1.16) and in particular, the v-axis dependence of the Fourier coefficients due to the k-th order Bessel function, we use an example in Fig. 1.3 to demonstrate the phenomena. The image in Fig. 1.3(a) is an infinitely long vertical sinc-strip image $f(x, y) = \mathrm{sinc}(600y)$, where $\mathrm{sinc}(\xi) = \sin(\pi\xi)/(\pi\xi)$. This strip does not vary in the process direction, and is centered at $y = 0$. It has zero crossings spaced apart by 1/600 inch in the y direction. The Fourier transform of this image is the function $F(u, v) = (1/600)\mathrm{rect}(v/600)\delta(u)$, which is a portion of an impulse sheet oriented along the v-axis. Here, $\mathrm{rect}(\xi) = 1, |\xi| < 1/2$,

and rect(ξ) = 0, otherwise. This spectrum is shown in Fig. 1.3(b). Fig 1.3(c) shows the sinc-strip image with laser scanner jitter. The maximum displacement of the jitter is 1/1200 inches. The Fourier spectrum of the sinc-strip image is shown in Fig. 1.3(d). We can see clearly in Fig. 1.3(d) that the constant amplitude impulse sheet in Fig. 1.3(b) is replicated along the u-axis at multiples of the fundamental frequency 60 cycles/inch of the periodic jitter, and that along the v-axis, the Fourier coefficients $J_k(-2\pi Av)$ continuously modulate the amplitude of each replication of this impulse sheet.

1.4 Fourier Analysis of a Continuous-space Halftone Image with Laser Scanner Jitter

In this section, we investigate in Fourier domain the relationship between a halftone image and periodic laser scanner jitter. We first derive in the Fourier domain the halftone image generated by the screening process. We use boldface lower case to represent vectors, and boldface upper case to denote matrices. In the following derivation, we use $(\mathbf{x}) = (x, y)^T$ and $[\mathbf{m}] = [m, n]^T$ to indicate continuous and discrete coordinates, respectively, where the units of $(\mathbf{x})$ and $[\mathbf{m}]$ are inches and printer-addressable pixels, respectively. Here m corresponds to the process (vertical) direction, and n corresponds to the scan (horizontal) direction.

The screening process generates the halftone image by thresholding the discrete-space continuous-tone image $g[\mathbf{m}]$ with a threshold array $t[\mathbf{m}]$ pixel by pixel. The threshold array is defined by two independent tile vectors $\mathbf{n}_1$ and $\mathbf{n}_2$; and the screen matrix $\mathbf{N}$ can be written as $\mathbf{N} = [\mathbf{n}_1|\mathbf{n}_2]$. Therefore, the discrete-space halftone image $h[\mathbf{m}; a]$ can be written as follow:

$$h[\mathbf{m}] = \begin{cases} 1, & \text{if } g[\mathbf{m}] \geq t[\mathbf{m}] \\ 0, & \text{else} \end{cases}, \tag{1.17}$$

where $t[\mathbf{m}]$ is the threshold array and its periodicity is based on the periodicity matrix N, i.e., $T[\mathbf{m} + \mathbf{Nq}] = T[\mathbf{m}], \forall \mathbf{q} \in Z^2$.

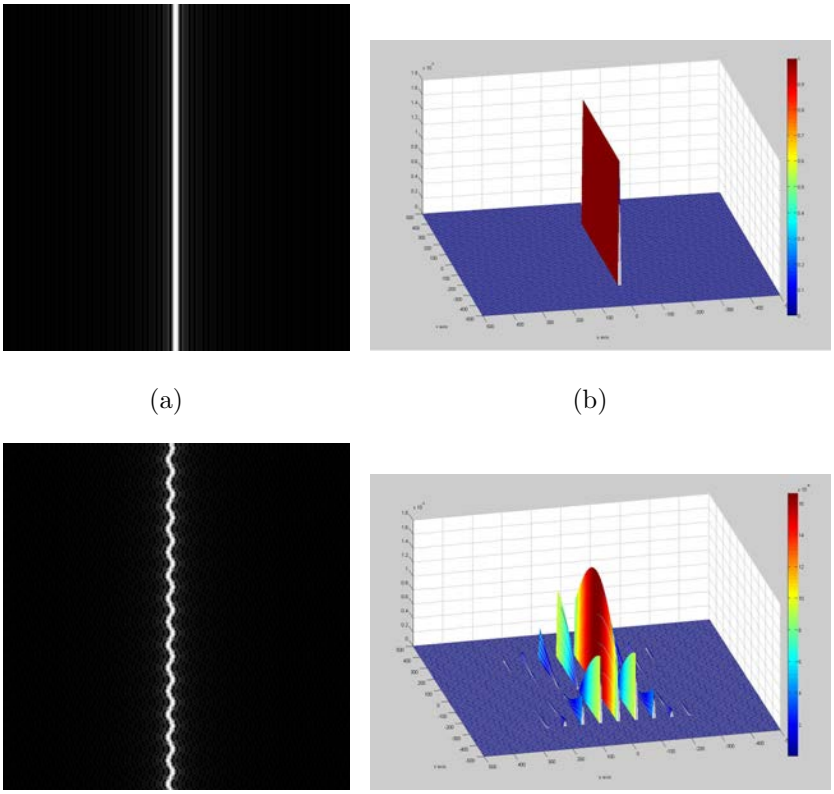

(a) (b)

(c) (d)

Fig. 1.3. Illustration of the infinitely long vertical sinc-strip image with laser scanner jitter that shows the v-dependent attenuation in the frequency domain. (a) The infinitely long vertical sinc-strip centered at y = 0 with zero crossings in the y direction separated by 1/600 inch. (b) The Fourier spectrum of the infinitely long vertical sinc-strip image, which is an impulse sheet with a rect function profile along the v-axis. (c) The infinitely long vertical sinc-strip image with laser scanner jitter. (d) The Fourier spectrum of the image in (a) with laser scanner jitter.

To simplified the derivation, we focus on a constant-tone image for the following analysis. If we halftone a constant-tone image, the resulting hafltone image is $h[\mathbf{m}; a]$ where the variable a is the absorptance between 0 (white) and 1 (black). Therefore, $h[\mathbf{m}; a]$ can also be expressed as

$$h[\mathbf{m}; a] = \begin{cases} 1, & \text{if } a \geq t[\mathbf{m}] \\ 0, & \text{else} \end{cases} . \tag{1.18}$$

The printer model is embodied by the printer dot profile $p_{\text{dot}}(\mathbf{x})$. For the ideal case, we do not consider the dot-gain effects in this study. Therefore, $p_{\text{dot}}(\mathbf{x})$ is exactly the printer-addressable pixel and we define the printer dot profile as

$$\begin{aligned} p_{\text{dot}}(\mathbf{x}) &= \text{rect}\left(\mathbf{x}/R\right), \\ &= \text{rect}(x/R)\text{rect}(y/R) . \end{aligned} \tag{1.19}$$

where the parameter R is the horizontal and vertical distance between printer-addressable pixels in units of inches. The resulting continuous-space halftone image $h(\mathbf{x}; a)$ can be expressed [12] as

$$h(\mathbf{x}; a) = \sum_{\mathbf{m} \in Z^2} h[\mathbf{m}; a]\ p_{\text{dot}}(\mathbf{x} - \mathbf{m}R) . \tag{1.20}$$

For periodic, clustered-dot screening, the colorant dots are placed compactly within each unit halftone cell Ω. If we let $c[\mathbf{m}; a]$ be the discrete-space halftone dot-cluster function within a unit halftone cell, it can be expressed as

$$c[\mathbf{m}; a] = \begin{cases} 1, & \text{if } a \geq t[\mathbf{m}] \text{ and } \mathbf{m} \in \Omega \\ 0, & \text{else} \end{cases} , \tag{1.21}$$

Due to its periodicity, the discrete-space halftone image $h[\mathbf{m}; a]$ can be also represented as

$$h[\mathbf{m}; a] = \sum_{\mathbf{t} \in Z^2} c[\mathbf{m} - \mathbf{N}\mathbf{t}; a] . \tag{1.22}$$

The Continuous Space Fourier Transform (CSFT) of $h(\mathbf{x};a)$ can be expressed as

$$\begin{aligned} H(\mathbf{u};a) &= \sum_{\mathbf{m}\in Z^2} h[\mathbf{m};a] \int_{-\infty}^{\infty} p_{\text{dot}}(\mathbf{x}-\mathbf{m}R)e^{-j2\pi\mathbf{u}^T\mathbf{x}}\, d\mathbf{x} \\ &= P_{\text{dot}}(\mathbf{u}) \sum_{\mathbf{m}\in Z^2} h[\mathbf{m};a]e^{-j2\pi\mathbf{u}^T\mathbf{m}R} \\ &= P_{\text{dot}}(\mathbf{u}) \sum_{\mathbf{t}\in Z^2}\sum_{\mathbf{m}\in Z^2} c[\mathbf{m}-\mathbf{N}\mathbf{t};a]e^{-j2\pi\mathbf{u}^T\mathbf{m}R} \\ &= P_{\text{dot}}(\mathbf{u})\breve{C}(\mathbf{u}R;a) \sum_{\mathbf{t}\in Z^2} e^{-j2\pi\mathbf{u}^T\mathbf{N}\mathbf{t}R}, \end{aligned} \tag{1.23}$$

where $P_{\text{dot}}(\mathbf{u})$ is the CSFT of $p_{\text{dot}}(\mathbf{x})$ defined as

$$\begin{aligned} P_{\text{dot}}(\mathbf{u}) &= \int_{-\infty}^{\infty} p_{\text{dot}}(\mathbf{x})e^{-j2\pi\mathbf{u}^T\mathbf{x}}\, d\mathbf{x} \\ &= R^2\text{sinc}(R\mathbf{u}) \\ &= R^2\text{sinc}(Ru)\text{sinc}(Rv)\,, \end{aligned} \tag{1.24}$$

and $\breve{C}(\mathbf{u};a)$ is the Discrete Space Fourier Transform (DSFT) of $c[\mathbf{m};a]$

$$\breve{C}(\mathbf{u};a) = \sum_{\mathbf{m}\in Z^2} c[\mathbf{m};a]e^{-j2\pi\mathbf{u}^T\mathbf{m}}\,. \tag{1.25}$$

Furthermore, in Eq. (1.23), $\sum_{\mathbf{t}\in Z^2} e^{-j2\pi\mathbf{u}^T\mathbf{N}\mathbf{t}R}$ is a 2-D comb function, and its Fourier series representation [12] of this 2-D comb function can be expressed as

$$\sum_{\mathbf{t}\in Z^2} e^{-j2\pi\mathbf{u}^T\mathbf{N}\mathbf{t}R} = \frac{1}{|\mathbf{N}|\,R} \sum_{\mathbf{t}\in Z^2} \delta(\mathbf{u}-\frac{1}{R}\mathbf{N}^{-T}\mathbf{t})\,, \tag{1.26}$$

where $\mathbf{N}^{-T}$ denotes the inverse and transpose of $\mathbf{N}$, and $|\mathbf{N}| \equiv |\det(\mathbf{N})|$. Applying Eq. (1.26) to Eq. (1.23), the $H(\mathbf{u};a)$ can be expressed as

$$\begin{aligned} H(\mathbf{u};a) &= \frac{1}{|\mathbf{N}|R}P_{\text{dot}}(\mathbf{u})\breve{C}(\mathbf{u}R;a) \\ &\quad \times \sum_{\mathbf{t}\in Z^2} \delta(\mathbf{u}-\frac{1}{R}\mathbf{N}^{-T}\mathbf{t})\,, \end{aligned} \tag{1.27}$$

Eq. (1.27) shows that altering the screen matrix $\mathbf{N}$ will change the location of the spectral energy in the frequency domain. In order to simply identify the points in

the frequency domain where the spectral energy of $H(\mathbf{u};a)$ is located, we refer to $\mathbf{F} = [\mathbf{f}_1|\mathbf{f}_2]$ as the *frequency matrix* defined by

$$\mathbf{F} = \rho\,\mathbf{N}^{-T}\,, \tag{1.28}$$

where ρ is the printer resolution in units of dot-per-inch (dpi). Note that the frequency matrix $\mathbf{F} = [\mathbf{f}_1|\mathbf{f}_2]$ actually defines the reciprocal lattice of the screen matrix $\mathbf{N}$.

To derive the relationship between this halftone image and periodic laser scanner jitter, we view the halftone image $h(\mathbf{x};a)$ as the continuous-tone image $f(x,y)$ in Eq. (1.1) that is subject to jitter. Then, the Fourier spectrum $F(u,v)$ for the continuous-tone image in Eq. (1.16) becomes the Fourier spectrum $H(\mathbf{u};a)$ for the halftone image given by Eq. (1.27). So substituting Eq. (1.27) into Eq. (1.16), we obtain

$$\widetilde{H}(\mathbf{u};a) = \sum_{k\in Z} J_k\big(-2\pi[0,A]\mathbf{u}\big)H\left(\mathbf{u} - [k/X,0]^T;a\right)\,, \tag{1.29}$$

where $\widetilde{H}(\mathbf{u};a)$ denotes the Fourier transform of the continuous-space halftone image with laser scanner jitter. Substituting Eq. (1.27) into Eq. (1.29), and we obtained the complete expression of the Fourier transform of the continuous-space halftone image with laser scanner jitter

$$\begin{aligned}\widetilde{H}(\mathbf{u};a) &= \frac{1}{|\mathbf{N}|R}\sum_{k\in Z} J_k\big(-2\pi[0,A]\mathbf{u}\big)P_{\text{dot}}\big(\mathbf{u}-[k/X,0]^T\big)\breve{C}\left((\mathbf{u}-[k/X,0]^T)R;a\right)\\ &\quad\times\sum_{\mathbf{t}\in Z^2}\delta\big((\mathbf{u}-[k/X,0]^T)-\frac{1}{R}\mathbf{N}^{-T}\mathbf{t}\big)\,.\end{aligned} \tag{1.30}$$

1.5 Evaluation of the Mathematical Model for Laser Scanner Jitter

To evaluate our mathematical model, we compute the Fourier spectrum of a halftone image with scanner jitter Eq. (1.30). We then compare the result with the Fourier spectrum of a scanned test target of a 25% tint-fill ($a = \frac{1}{4}$) constant-tone image halftone printed at 600 dpi with two different colorants, black and magenta, using a dry toner laser EP printer. The printed test target is then scanned with an

EPSON Expression 10000XL at 2400 dpi. The corresponding periodicity matrices of these two colors are the default design for our target printer. The screen tile vectors for magenta are $\mathbf{n}_1 = [3, -1]^{\mathrm{T}}$ and $\mathbf{n}_2 = [1, 3]^{\mathrm{T}}$. For black, they are $\mathbf{n}_1 = [2, -2]^{\mathrm{T}}$ and $\mathbf{n}_2 = [2, 2]^{\mathrm{T}}$. The screen frequency for magenta is 190 lpi. For black, it is 212 lpi. The screen angle for magenta is 18 degrees. For black, it is 45 degrees. The size of the scanned image target is 1000×1000.

Figure 1.4 shows the scanned images of test targets that are printed with a printer with normal-case and worst-case laser scanners. In our experiment, we swapped the laser scanner assembly in the same printer to eliminate other sources of variability that might be observed from printer to printer. The left column images of Fig. 1.4 are printed with the normal-case laser scanner. The right column images of Fig. 1.4 are printed with the worst-case laser scanner. We can see a significant visual difference between the two images in the first row of Fig. 1.4. However, we do not see a visible difference between the magenta test targets because of the screen angle of the magenta.

To compare the Fourier transform of the scanned images with the analytical results obtained by evaluating Eq. (1.30), we apply the following processes to the scanned images in Fig. 1.4(b) and 1.4(d). First, we transform the scanner RGB to linear RGB by computing the gray balancing curves for the R, G and B channels. To obtain the gray balancing curves, we first scan the 24 neutral gray scale patches on the Kodak Q60 target, which is shown in Fig. 1.5, with an EPSON Expression 10000XL scanner at 2400 dpi. The R, G, and B values for each patch are computed as the average of all the pixel values within each patch. Then, the CIE Y value of each gray scale patch is measure by the X-rite DTP70 Spectrophotometer as shown in Fig. 1.6. Finally, the gray balancing curves can be approximated by a power law equation as follows

$$R_l \;=\; a(R/255)^b + c\,, \tag{1.31}$$

where $R_l = Y/100$, and R_l is the linearized R output value for a patch. Similarly, we can also find the parameters, a, b, and c for the G and B channels. The values of

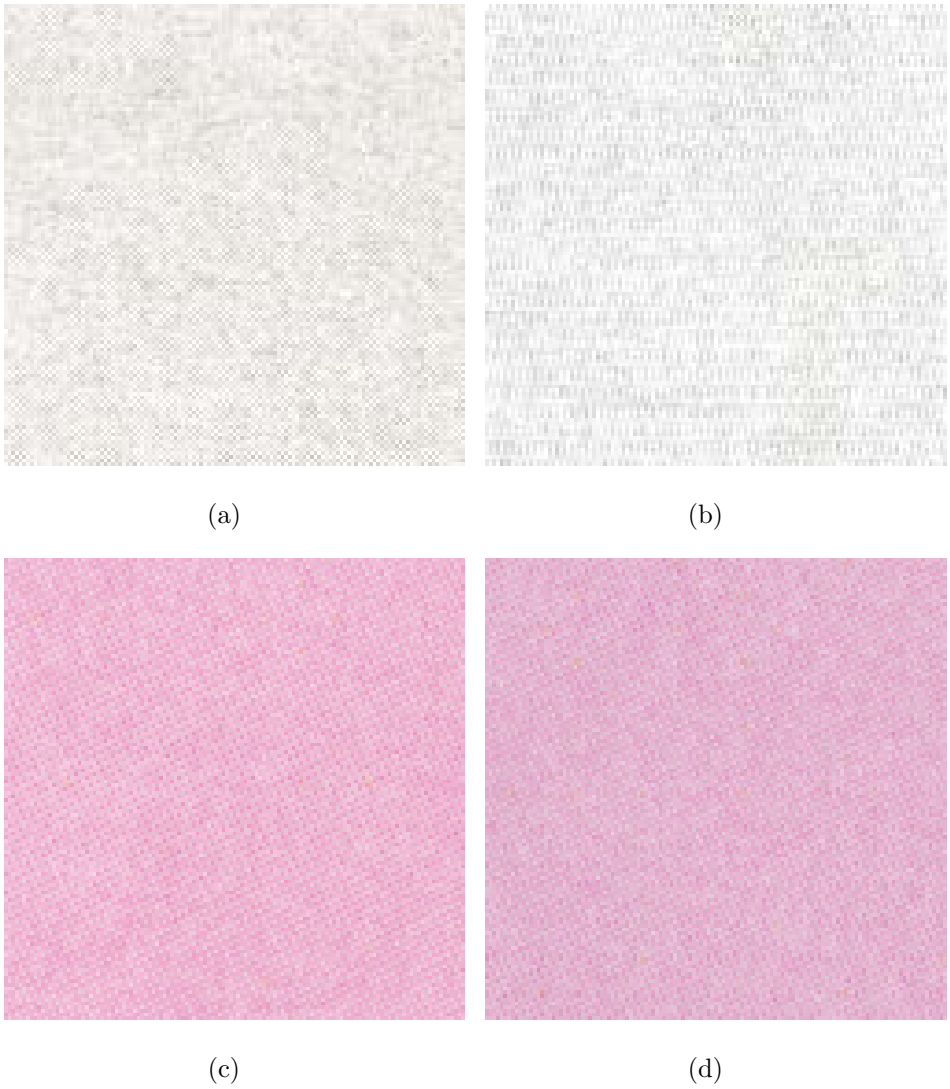

(a) (b)

(c) (d)

Fig. 1.4. Comparison of the scanned test targets with and without laser scanner jitter in black and magenta. (a) The black color test target without laser scanner jitter, and the dot coverage is 25%. (b) The scanned test target with laser scanner jitter. (c) The magenta color test target without laser scanner jitter, and the dot coverage is 25%. (d) The scanned test target with laser scanner jitter.

Table 1.1
The parameters for the power law equation for each channel

	R	G	B
a	0.004652	0.008277	0.002842
b	1.791	1.68	1.886
c	0.5154	0.3634	0.5

parameters, a, b, and c for the R, G and B channels can be found in Table 1.1. The gray balancing curves for R, G and B channel are shown in Fig. 1.7 (a)–(c).

Fig. 1.5. Kodak Q60 target we used to obtain the gray balancing curves for the R, G and G channels, and the transformation matrix from linear RGB to CIE XYZ.

Next, we find the transformation matrix for transforming the linear RGB values to CIE XYZ values. We use the process mentioned above to obtain the linear RGB values for the 228 color patches on the Kodak Q60 target. Then, the transformation matrix, M, is given by

$$\begin{aligned} M &= (A^T A)^{-1} A^T X \\ &= \begin{bmatrix} 0.5327 & 0.2889 & 0.0460 \\ 0.2673 & 0.5902 & 0.1194 \\ 0.0869 & 0.0376 & 0.5664 \end{bmatrix}, \end{aligned} \tag{1.32}$$

Fig. 1.6. X-rite DTP70 Spectrophotometer is used to measure the CIE Y value of each gray scale patch on the Kodak Q60 target.

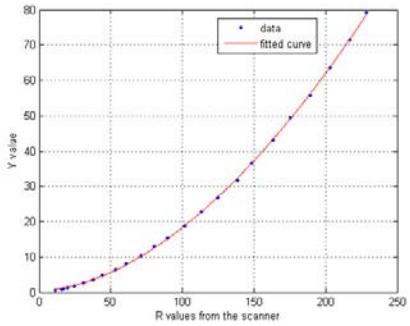

(a)

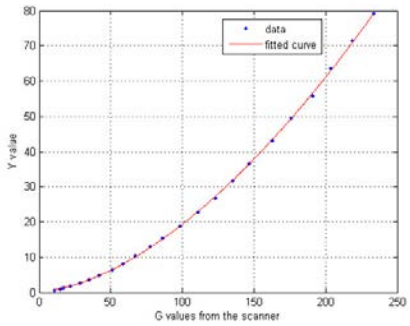

(b)

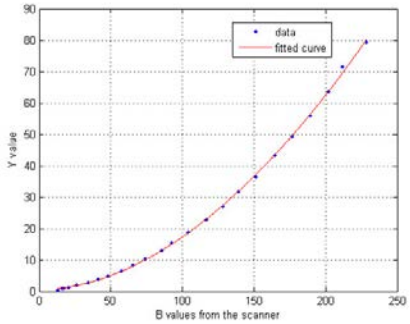

(c)

Fig. 1.7. The Gray balancing curves for R, G and B channel are approximated by a power law equation that uses the average of all the pixel values in each channel within each gray patch on the Kodak Q60 target, and the measured CIE Y value of each gray patch. (a) The gray balancing curve for R channel. (b) The gray balancing curve for G channel. (c) The gray balancing curve for B channel.

where matrix A (228×3) contains the 228 linear RGBs, and matrix X (228×3) contains the corresponding CIE XYZ values. Eq. (1.32) also shows the experimental result of the transformation matrix M. Based on the above processing, Fig. 1.4(b) and 1.4(d) are transformed to CIE XYZ. Finally, the CIE Y values are scaled to range from 0 (black) to 255 (white). We call the scanned Y image processed as described above the luminance image. The luminance images in black and magenta are shown in Fig. 1.8(b) and Fig. 1.8(e).

Before computing the 2D Discrete Fourier Transform (DFT) of the luminance image, we first perform the contrast stretching technique to enhance the luminance image for both Fig. 1.8(b) and (d). For black luminance image as shown in Fig. 1.8(b), we map the absorptance 100 in the black luminance image to absorptance 0, and map the absorptance 255 in the black luminance image to absorptance 255. The values between the absorptance 100 and absorptance 255 are scaled linearly in the range [0, 255]. The black enhanced luminance image is shown in the Fig. 1.8(c). On the other hand, we perform a different image enhancement to the magenta luminance image because it has very few absorptance 255. Therefore, we perform the following processes to the magenta luminance image. we map the minimum value in the black luminance image to absorptance 0, and map the maximum value in the black luminance image to absorptance 255. The values between minimum value and maximum value are scaled linearly in the range [0, 255]. The magenta enhanced luminance image is shown in the Fig. 1.8(f).

Subsequently, we compute the 2D Discrete Fourier Transform (DFT) of the enhanced luminance image. However, there are vertical and horizontal line smears, and noise in the frequency spectrum of the enhanced luminance image. These artifacts are not accounted for by our analytical result obtained by evaluating Eq. (1.30). The vertical and horizontal line smears may be due to that fact that the size of the enhanced luminance image is a non-integer multiple of periods of the halftone pattern. To eliminate the smears, a raised-cosine window function is applied to the enhanced luminance image and it is shown in Fig. 1.9. This window function drops from 1 to

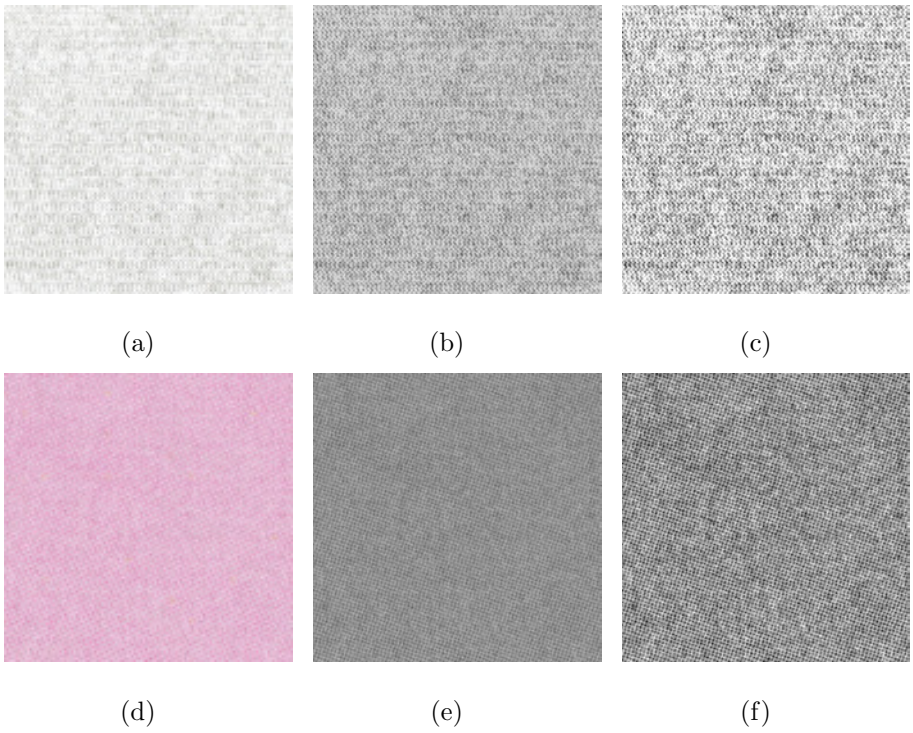

Fig. 1.8. Illustration of the results that the scanned test targets in black and magenta are transformed to CIE Y images, and CIE Y images are enhanced by the contrast stretching technique. (a) The black color test target wit laser scanner jitter, and the dot coverage is 25% as same as in Fig. 1.4(*b*). (b) The black color test target is transformed to CIE Y image that is called luminance image in this article. (c) The black enhanced luminance image. (d) The magenta color test target with laser scanner jitter, and the dot coverage is 25% as same as in Fig. 1.4(*d*). (e) The magenta color test target is transformed to CIE Y image. (f) The magenta enhanced luminance image.

0 within a zone inside each boundary of the image that comprises 5% of the total width or height of the image. In our experiment, we only apply this window function to the black color enhanced luminance image because the DFT of the magenta color enhanced luminance image does not show obvious vertical and horizontal line smears. To better show the spectrum, especially the low intensity features, Chang and Allebach [13] had the spectrum logarithmically compressed according to

$$i_{OUT} = \Big(255/\big(log(K+1)\big)\Big) log\Big(K\big(i_{IN}/max(i_{IN})\big)+1\Big). \tag{1.33}$$

where i_{OUT} is the logarithmically compressed spectrum and i_{IN} is the input spectrum. The parameter K for the DFT of the enhanced luminance images are chosen empirically by 1000. The parameter K for the analytical spectra are chosen emprically by 5×10^4. The final Fourier spectra of the printed and scanned halftone patches are shown in Fig. 1.10(a) and (d).

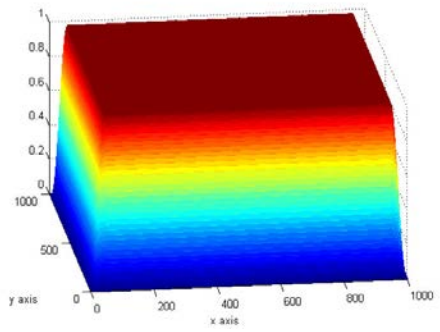

Fig. 1.9. A raised-cosine window function is applied to the luminance image. This window function drops from 1 to 0 within a zone inside each boundary of the image that comprises 5% of the total width or height of the image.

Figure 1.10 compares the analytical results obtained by evaluating Eq. (1.30) to those obtained by computing the DFT of the windowed enhanced luminance image of the black and the enhanced luminance image of the magenta. The first column images of Fig. 1.10 are the Fourier spectra of the windowed enhanced luminance image (black) and the enhanced luminance image (magenta). The second column images of Fig. 1.10

are based on Eq. (1.29) with the default periodicity matrices. For the computation, we set the values for the parameters in Eq. (1.30) as follows: $A = 1/1200$ inches, $a = 0.25$ absorptance units, $X = 1/60$ inches, and $R = 1/600$ inches. According to Eq. (1.30), we will have frequency components where the impulses are located; and an impulse corresponds to a pixel in the plot. To enhance its visibility, we replace each such impulse by a 9×9 square with constant amplitude. The Fourier spectrum of the continuous-space halftone image with laser scanner jitter exhibits replications of the spectrum of the original continuous-space halftone image. Each replication is separated by 60 cpi (cycles per inch) in the frequency domain with different weights. This is because the period X of the laser scanner jitter is $\frac{10}{600}$ inches. By comparison, the spectrum of the scanned image also shows replications that are separated by 60 cpi.

We can see that the analytical Fourier spectrum of magenta can predict the spectrum of the enhanced luminance image effectively. However, there is some mismatch in black. There are three possible reasons for this issue. First, the instability of the EP process may not reproduce the given test target perfectly. Furthermore, the screen frequency of black is higher than the screen frequency of magenta. Thus, the printed image of magenta would have better print quality. Second, we assume the displacement function to be a sinusoid function. However, the actual displacement is not a perfect sine wave function. Finally, the Fourier spectrum of the windowed luminance image shows that the spectral peaks roll off more as we move away from the origin than is the case with the analytical spectrum computed using Eq. (1.30). This could be due to the fact that our analytical model assumes that each printer addressable pixel is the function $\text{rect}(\frac{\mathbf{x}}{R})$. However, the effective spot shape may be larger than it is in our model due to dot gain effects. The above factors may be responsible for the mismatch in the Fig. 1.10(a) and Fig. 1.10(b).

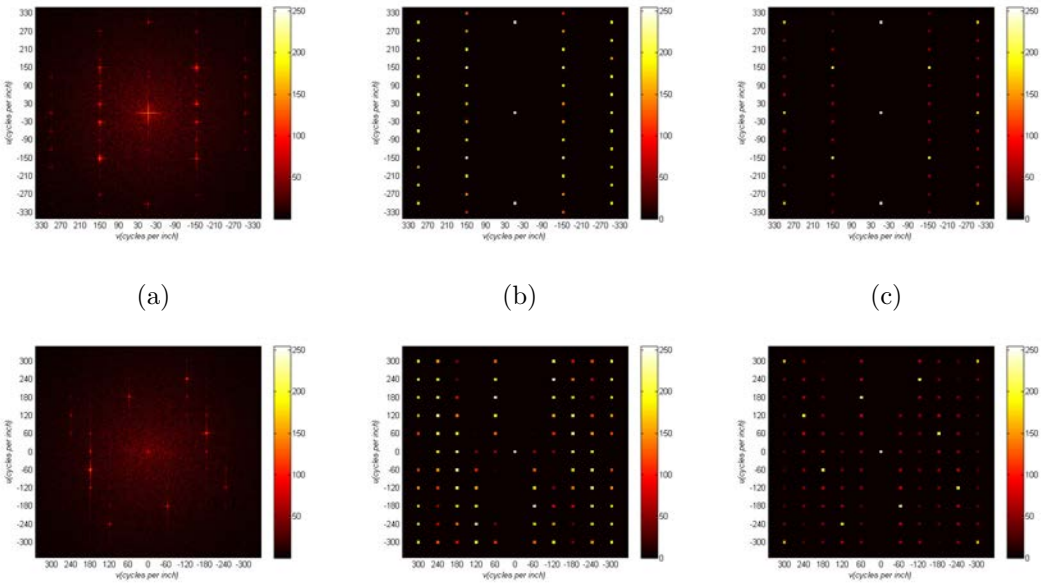

(a) (b) (c)

(d) (e) (f)

Fig. 1.10. Comparison of the Fourier spectrum of the scanned test target and the analytical Fourier spectrum both with laser scanner jitter. (a) The Discrete Fourier Transform of the black color windowed enhanced luminance image obtained by the color space transformation of the black color scanned test target in Fig. 1.4(b) followed by image enhancement, windowing and, finally, logarithmically compressed according to Eq. (1.33). (b) The result of using Eq. (1.29) to compute the Fourier spectrum of the continuous-space halftone image with laser scanner jitter using the periodicity matrix for black. (c) The analytical Fourier spectrum of black, which is based on Eq. (1.10) and Eq. (1.8). The Fourier coefficient $C_k(v)$ defined in Eq. (1.8) is numerically evaluated based on the estimated displacement function that is describe in Section 1.6 instead of assuming a sinusoidal displacement. (d) The Discrete Fourier Transform of the magenta color enhanced luminance image obtained by the color space transformation of the magenta color scanned test target in Fig. 1.4(d) followed by image enhancement and logarithmically compressed according to Eq. (1.33). (e) The result of using Eq. (1.29) to compute the Fourier spectrum of the continuous-space halftone image with laser scanner jitter using the periodicity matrix for magenta. (f) The analytical Fourier spectrum of magenta obtained by using the Fourier coefficient numerically evaluated based on the estimated displacement function instead of assuming a sinusoidal displacement.

1.6 Estimation of the Displacement Function

In the previous section, we show that there are mismatches between the Fourier spectrum of the scanned test target and the analytical Fourier spectrum both with laser scanner jitter. One of the reasons is that we assume the displacement function to be sinusoid function and periodic. Thus, we can derive a closed form for Fourier series coefficients, which is the k-th order Bessel function. Instead of making that assumption, we estimate the actual displacement by creating another test target and keep the assumption that the displacement function is periodic.

The test target is shown in Fig. 1.11(a), and it uses to measure the displacement function of laser scanner jitter. The fiducial marks on the top and bottom of the target are used to measure the skew. Fig. 1.11(b) is the zoomed-in image of the red box indicated in Fig. 1.11(a). Each group of line segments has 11 line segments, and each line segment, 4 pixels wide, within a eleven-line-segment group separates 7 pixels. Each line segment denotes a certain facet of the polygon mirror as shown in the Fig. 1.11(b), and the first and last line segment denote the same facet. The first line segment of every eleven-line-segment group is always the first facet.

To measure the displacement function, we first printed at 600 dpi with two different colorants, black and magenta, using a dry toner laser EP printer. The printed test target is then scanned with an EPSON Expression 10000XL at 800 dpi, and the scanned test target and zoomed-in scanned test target are shown in Fig. 1.12(a) and (b). To analyze the scanned image, We binarize the zoomed-in image by Otsu's algorithm [14], and the binarized image is shown in Fig. 1.12(c). Next we applied the connected component analysis [15], and then compute the centroid of each connected component. Fig. 1.12(d) shows the locations of centroid of each line segment in red cross. We use the centroid of the first line segment in each eleven-line-segment group as the reference. Before calculating the estimated displacement function, we apply the rotation matrix to the centroid coordinates to correct the skew. The rotation matrix is obtained by finding the centroids of fiducial marks, and the centroid coordinates

is used to retrieve the skew angle. The rotation matrix for black is shown in Eq. (1.34) with $\theta = 0.1709$ and rotation matrix for magenta is shown Eq. (1.35) with $\theta = 0.0749$. Since the first and last line segment denote the same facet, we average the y coordinate of the centroid of the first and last line segment, and use it as a reference to calculate the relative difference from the rest of 9 lines segments. Next, we collect relative differences of 100 eleven-line-segment groups, and average them. Then, we use these 10 relative differences data to fit a curve, the estimated displacement function $d_{estimate}(x)$ by using cubic spline interpolation. We do the above processes to the scanned test target in black and magenta colorants. We show the estimated displacement functions for black and magenta colorants in Fig. 1.13, and the estimated displacement is in unit of pixel. As stated in the beginning of this section, we assume the displacement function is periodic, and the period is 10, the number of facets of the polygon mirror in our target printer.

$$\begin{aligned} R_{black}(\theta) &= \begin{bmatrix} \cos(\theta) & -\sin(\theta) \\ \sin(\theta) & \cos(\theta) \end{bmatrix} \\ &= \begin{bmatrix} 1.000 & -0.003 \\ 0.003 & 1.000 \end{bmatrix} \end{aligned} \tag{1.34}$$

$$R_{magenta}(\theta) = \begin{bmatrix} 1.0000 & -0.0013 \\ 0.0013 & 1.0000 \end{bmatrix} \tag{1.35}$$

As we have the estimated displacement function for black and magenta test targets, we can numerically evaluate the Fourier coefficient $C_k(v)$ defined in Eq. (1.8), and we can have the spectrum of a halftone image with laser scanner jitter $G(u, v)$ according to Eq. (1.10). The resulting spectra of a halftone image with laser scanner jitter are shown in Fig. 1.10(c) and Fig. 1.10(f). The resulting spectra are also logarithmically compressed according to Eq. (1.33), and the parameter K is chosen empirically to be 5×10^4. We can see that the analytical Fourier spectra give a better prediction to spectrum of the enhanced luminance image than the experimental

results in Fig. 1.10(b) and Fig. 1.10(e). But, some mismatches still exists. The spectral peaks roll off more as we move away from the origin than is the case with the analytical spectrum since dot gain effects may be responsible for this issue.

1.7 Conclusion

In this chapter, we present a new method for characterizing and analyzing the Fourier spectrum of periodic laser scanner jitter. Unlike prior studies, we incorporate the periodic characteristics of laser scanner jitter into the mathematical model and extend the model to the special case where the jitter has a sinusoidal displacement. This leads to a simple closed-form expression in terms of Bessel functions of the first kind. We further investigate the Fourier domain relationship between a continuous-space halftone image and laser scanner jitter. Our preliminary experimental results show that the mathematical model based on the sinusoidal displacement can effectively characterize the phenomenon of laser scanner jitter, but there is some mismatches. To improve experimental results, we create another test target to directly estimate the displacement function instead of assuming a sinusoidal displacement. This gives a better prediction of the phenomenon of laser scanner jitter.

(a)

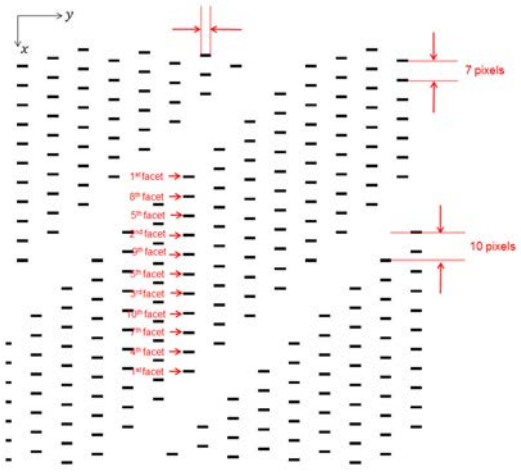

(b)

Fig. 1.11. Illustration of the test target that uses to measure the displacement function of laser scanner jitter. (a) The test target designed for estimating the displacement function of laser scanner jitter. The fiducial marks on the top and bottom of the target are used to measure the skew. (b) The zoomed-in image of the red box indicated in (a). Each column of line segments has 11 line segments, and each line segment, 4 pixels wide, within an eleven-line-segment group separates 7 pixels wide. Each line segment denotes a certain facet of the polygon mirror as shown in the figure, and the first and last line segment denote the same facet. The first line segment of every eleven-line-segment group is always the first facet.

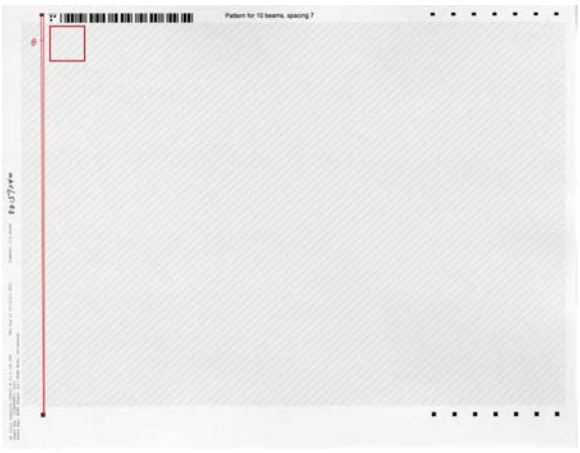

(a)

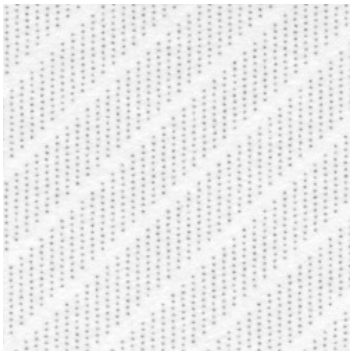

(b)

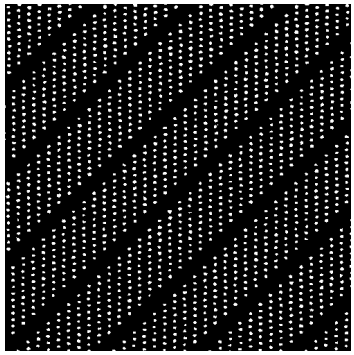

(c)

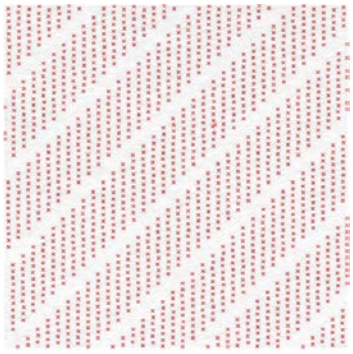

(d)

Fig. 1.12. Illustration of the process to get the centroid of each line segment in the scanned test target. (a) The scanned test target with skew. The fiducial marks are used to correct the skew. (b) The zoomed-in scanned test target. (c) The binarized scanned test target, which is binarized from the zoomed-in scanned test target by the Otsu's algorithm. (d) The binarized scanned test target is applied with the connected component analysis, and the connected component map is used to calculate the centroid location of each connected component. The centroid locations are marked by red crosses.

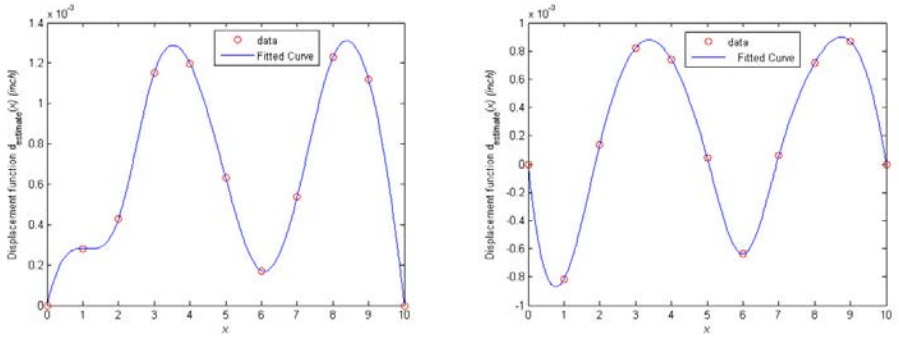

(a) (b)

Fig. 1.13. Illustration of the estimated displacement function $d_{estimate}(x)$. (a) The estimated displacement function $d_{estimate}(x)$ for black color. Red circles are the relative differences obtained by using the test target in Fig. 1.11. Then, the data are fitted by the cubic spline interpolation. According to our assumption, the estimated displacement function $d_{estimate}(x)$ is periodic, and the period is 10, the number of facets of the polygon mirror in our target printer. The estimated displacement function $d_{estimate}(x)$ is used to numerically evaluated the Fourier coefficient defined in Eq. (1.8). Then, we can obtain the better prediction of the spectrum of a halftone image with laser scanner jitter as shown in Fig. 1.10. (b) The estimated displacement function $d_{estimate}(x)$ for magenta color.

2. PAGE CONTENT ANALYSIS FOR OPTIMAL RENDERING

2.1 Introduction

A typical document page is composed of miscellaneous image objects that have different characteristics. Figure 2.1(a) shows a common example of such a page. This page contains text, photos, pictures, gradient regions, graphics, and background. In this paper, we divide these different parts of the page into high frequency or low frequency areas according to their spatial frequency content. We refer to high frequency areas as *detail*, and low frequency areas to *smooth*. As indicated in Fig. 2.1(a), photos and pictures belong to the detail area since the color changes frequently. On the other hand, gradient regions and the background are part of the smooth area because of the slower color change. We call pictures or photos *raster*, and gradient or graphics regions *vector* in this study.

To reproduce this page content with a laser electrophotographic (EP) printer, it is common practice to choose one of the various halftoning techniques and to apply it to all areas of the page regardless of the image characteristics. With such miscellaneous image objects on a single page, one single halftoning approach may not produce the best print quality with a laser EP printer. This is because laser EP printers are innately unstable due to the fluctuations in the angular velocity of the photoconductor (OPC) drums, and irregular development and transfer processes. Therefore, the halftone patterns may be susceptible to print artifacts such as fine pitch banding, streaks, and mottle. [16–18] In particular, print artifacts are more visible in the smooth areas of the printed document if we apply a high frequency screen to them. On the other hand, in detail areas the detail information will mask

the appearance of halftone artifacts that can occur with a high frequency screen; and the high frequency screen will better reproduce the detail information.

To overcome this issue, several different halftoning approaches have been suggested in the literature. [19–22] Basically, different halftone screens are used on different parts of the page. Park [23] et al refer to this approach as *object-oriented halftoning*. While previous works [19–22] demonstrated that the object-oriented halftoning can improve the overall print quality, these methods may produce boundary artifacts due to the mingling of different halftone textures. Park et al proposed a *seamless halftoning algorithm* to remove such boundary artifacts. [23]

Based on Park et al [23], in this study we apply a high lpi (lines-per-inch) screen to detail objects, and a low lpi screen to smooth objects. Figure 2.1 shows an example illustrating a typical page content and its corresponding object map. In Table 2.1, we also summarize the different object types, their color codes in the object map images, and the halftone screen corresponding to each. We apply a high lpi screen to the raster and background and text regions. On the other hand, we apply a low lpi screen to the vector region. For the purpose of applying different halftone screens to different regions of the page, we need an object map, an initial version of which can be extracted from the page description language (PDL) used to represent the page. Example languages include PCL, Postscript, and PDF.

The PDL communicates the description of each page generated by a composition system to a rendering system. The PDL specifies how each object on the page should appear when rendered on the final output medium such as a display or paper. [24–26] The PDL describes the appearance of the page composed of different objects such as texts, graphics, and images in terms of abstract graphical elements instead of device pixels. [26] These abstract graphical elements are converted by the raster image processor (RIP) into a display list, a series of graphics commands. The commands are then rasterized into an array of pixels that represent the output page image. The rasterization also extracts the object type information of each object, and this information forms the initial object map. The output image and the object type in-

formation are fed to the imaging pipeline of an output device, such as a display driver, printer driver, or embedded printer formatter or controller for further processing.

However, the information of object type obtained from the PDL may be incorrect due to the fact that some objects are originally defined as pictures or photos in the PDL by the application that generated the document, even though they contain no frequent color variation. Such areas may be interpreted as raster by the RIP. Figure 2.2 shows an example illustrate the misclassification in the RIPping process. In Fig. 2.2(a), the black box indicates a smooth region in a page document, and the corresponding region in the initial object map is classified as raster, whereas it should be vector. If we apply a high lpi halftone screen to this region, it is more susceptible to print artifacts. To reduce the appearance of these artifacts, we want to modify these regions to vector to apply a low lpi halftone screen, and thereby improve the overall print quality.

To correct the misclassification in the object map, a reclassification step is needed. Different document image analysis and segmentation algorithms have been suggested in the literature. Shafait et al [29] reported several page segmentation algorithms and presented an approach to evaluate their performance. These algorithms segment a page into blocks, and classify these blocks with predefined labels. [30] Instead of segmenting the page into blocks, Shadkami and Bonnier [31] introduced a watershed-based approach to segment a document into regions and classify them with a size filter into text, background, and image. On the other hand, Moll et al [32] classified each pixel as a predefined class using a k-nearest neighbors based classifier. Rather than classifying blocks or pixels in the given image, Cheng and Bouman [33] proposed a multiscale Bayesian segmentation and used a trainable model for different segmentation applications. The aforementioned algorithms proposed solutions to segment the page into different objects and classified them according to certain rules. In addition, there are several works aimed to extract photos, pictures and detail areas directly from the given page document. Won [34] adapted the block segmentation approach based on a maximum a posteriori (MAP) framework and pixel-based refine-

ment around the block boundary to extract images in a document. Chiu et al [36] applied an optical character recognition (OCR) system to mask text regions and the normalized cut algorithm [38] to cluster non-text pixels into pictures. More recently, Erkilinc et al [35] proposed an algorithm to classify a scanned document into text, photo and strong lines by five different processes. First, they applied several image preprocessing techniques to the scanned images. The two to fourth processes are that text regions are extracted by applying wavelet transform and run-length coding, photo regions are segmented by applying Markov random field based block-wise segmentation [34], and strong lines regions are detected by performing edge detection algorithms and Hough transform. Finally, K-means algorithm is used to combine the extraction of the text, photo and strong line maps to generate a page layout.

Unlike the previous works, their reclassification and segmentation approaches are based on the given input image. However, we have the initial object map extracted from the RIP in this study even though there may be misclassifications in some areas. Based on experimental observation, these misclassifications mostly appear in raster regions. Smooth areas are classified as raster rather than vector. Rather than using relatively complex approaches such as those described in the references cited above to fully segment the page image from scratch, and then classify each region with predefined labels, we only focus on the raster regions that are defined in the object map and correct them with simpler approaches.

Chen et al [37] proposed an algorithm that combines three features extracted from the input image and the segmentation algorithm to generate a map that indicates the photos and images in the input image. In the segmentation part, Chen et al applied the connected component analysis (CCA) twice, one finds the regions that should be classified as raster based on a criterion and another one modifies the misclassification around the text characters. The target of this algorithm is to be implemented in the imaging pipeline of the laserjet printer. Applying two CCA is not feasible in the hardware implementation. A more efficient algorithm should be explored.

In this chapter, we propose a more efficient segmentation-based object map correction algorithm (SBOMCA) to modify the initial object map generated by the RIP. The algorithm focuses on correcting the misclassification in raster areas since some raster areas should be vector. We combine feature extraction, segmentation and mathematical morphology algorithms to generate a map that indicates the true raster areas in the input image. Then, the corrected object map can mark each object in the continuous-tone raster image with the correct object type. In addition, we introduce a new imaging pipeline, which incorporates the SBOMCA and the idea of object-oriented halftoning. With this new imaging pipeline, we can achieve our ultimate goal – the improvement of overall print quality.

The rest of the chapter is organized as follows. In the next section, we briefly review the new imaging pipeline and seamless halftoning algorithm. Next, we present a detailed description of the segmentation-based object map correction algorithm (SBOMCA) in the Section 2.3. Then, experimental results are provided. Finally, we conclude in the last section.

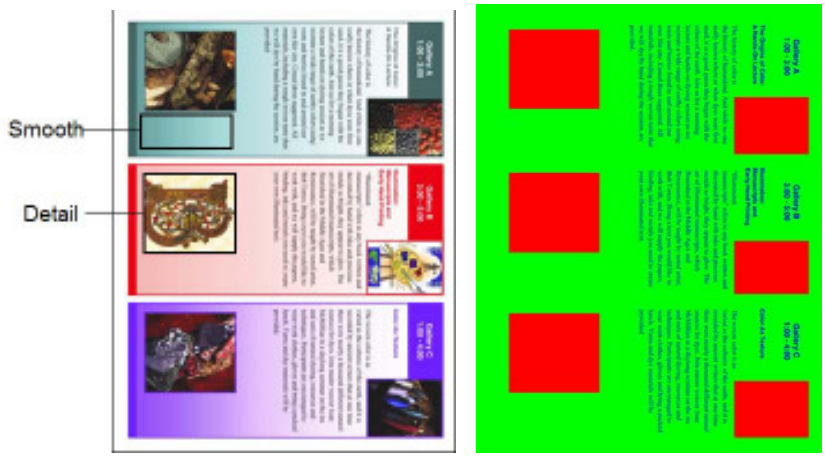

(a) (b)

Fig. 2.1. Illustration of the object type definition (a) Example page content classification: smooth and detail regions. (b) The corresponding object map showing the complete page content classification color-coded according to Table 2.1.

Table 2.1
Color code for the object map

	Red	Green	Blue
Object Type	Raster	Vector and Background	Text
Halftone Screen	High	Low	High

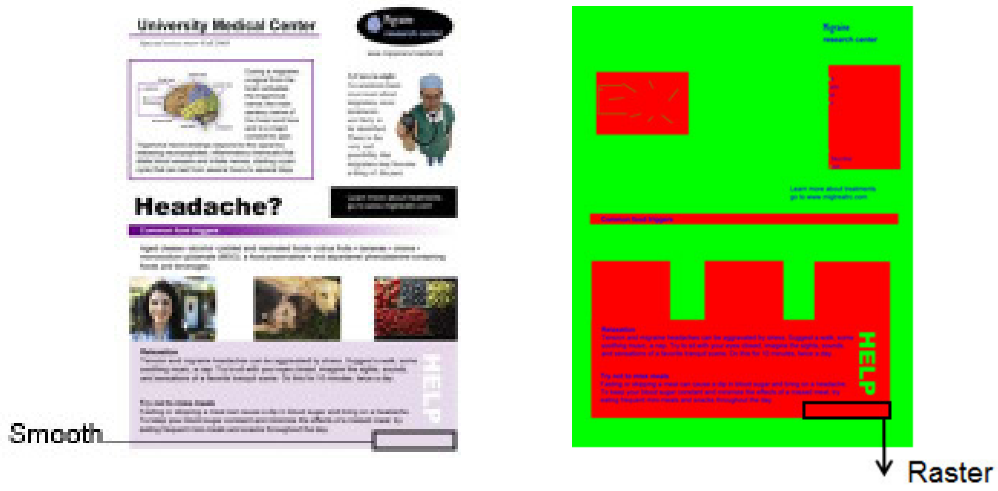

(a) (b)

Fig. 2.2. Illustration of the misclassification in the object map (a) A typical page document. (b) The corresponding initial object map with misclassification.

2.2 Preliminaries

2.2.1 The New Imaging Pipeline

Figure 2.3 shows the new imaging pipeline for laser EP printers. The RIP interprets a description of the page expressed in the form of a PDL to create a display list, which is a series of commands that define a rasterized image. This image is

then rendered by executing the display list. The output of this interpretation is a continuous-tone RGB color space raster image. In addition, the RIP extracts information that identifies the object type associated with each object in the rasterized image. We call it the initial object map. It describes each object on the page as raster, vector, text, or background. However, the object type information may be incorrect. The object map correction algorithm is proposed to modify the initial object map. Afterward, the continuous-tone RGB color space image is transformed by the color channel conversion block into a continuous-tone CMYK color space image. Then, it is halftoned by using the concept of object-oriented halftoning that is based on the corrected object map, and halftone blending [23]. Finally, the halftoned CMYK image is sent to the marking engine to generate a hardcopy document. [27, 39, 40]

The conventional imaging pipeline is more susceptible to print artifacts since the rendered image is halftoned with only one halftone method on the entire page regardless of its image characteristics. To address this issue, the new imaging pipeline applies low frequency screens to smooth areas to reduce the appearance of print artifacts; and it applies high frequency screens to detail areas to preserve the detail rendition. Consequently, the new imaging pipeline can improve the overall print quality.

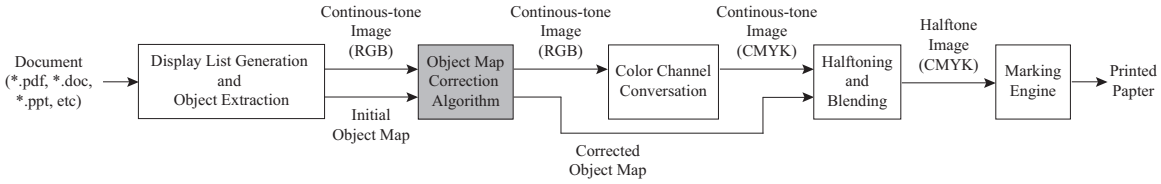

Fig. 2.3. The new imaging pipeline for laser electrophotographic (EP) printers.

2.2.2 Seamless Halftoning

Object-oriented halftoning applies a low lpi frequency screen to smooth areas and high lpi frequency screen to detail areas. Although this process improves the overall

quality, it introduces artifacts along the boundary between objects halftoned with two different frequency screens due to the mingling of different halftone textures. [23]. Figure. 2.4 illustrates these boundary artifacts. To reduce these artifacts, Park et al [23] proposed a seamless halftoning approach.

Seamless halftoning creates a transition region along the boundary between objects halftoned with different screens. This transition region has different halftone textures that are generated by blending the two halftone textures from the detail and smooth screens. The transition region starts at the edge of the region that will be halftoned exclusively with the smooth screen and ends at the edge of the region that will be halftoned exclusively with the detail screen. The concept of the transition region is shown in Fig. 2.5. As we move from the start of the transition region to the end of the transition region, the strength of the smooth screen decreases. Conversely, the strength of the detail screen increases, as the strength of the smooth screen diminishes. The strength ratio of the two screens is determined by the parameter d, which is defined as the distance between the starting point of the transition region and the current pixel (x, y). At the center of the transition region, the ratio is unity. At the end of the transition region, where $d = d_{max}$, the strength of smooth screen is effectively zero.

Based on the distance parameter d, Park et al [23] describe the blending process by the following equation

$$g(x,y) \;=\; \max\{h^{(S)}(x,y), h^{(D)}(x,y)\}\,, \tag{2.1}$$

where $g(x, y)$ is the pixel value after blending process, $h^{(S)}(x, y)$ is the smooth halftone texture and $h^{(D)}(x, y)$ is the detail halftone texture. To design these halftone screens, Park et al [23], and Lee and Allebach [28] give detailed descriptions for the design of periodic, clustered-dot halftone screens for application to laser EP printers with the mechanism of pulse width modulation (PWM) that allows each pixel of the halftone image to be defined as a multi-bit quantity that specifies pulse-width and possibly a justification mode.

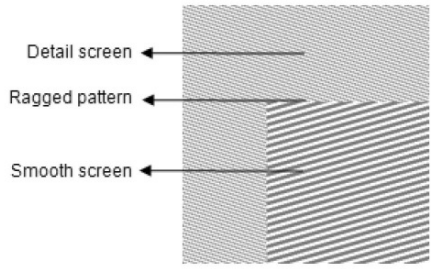

Fig. 2.4. Boundary artifact caused by object-oriented halftoning. [23]

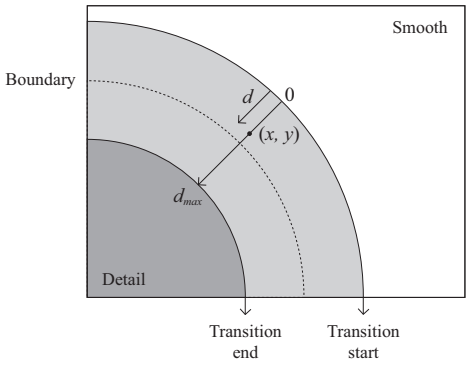

Fig. 2.5. Transition region for blending halftone texture. [23]

2.3 Segmentation–Based Object Map Correction Algorithm

The segmentation-based object map correction algorithm (SBOMCA) uses four different features that form three maps, the connected components analysis algorithm and morphological erosion to modify the initial object map. The block diagram is shown in Fig. 2.6. There are four steps in the SBOMCA. First, a raster decision map (RDM) is computed based on three maps that are formed by extracting four different features that extracted from the continuous-tone RGB color space image and initial object map. These four features are second order derivative, saliency, neutralness of the pixel in the continuous-tone RGB image and text. The RDM reflects potentially the regions of the truly raster. Second, we apply connected component analysis (CCA) to label the thresholded edge map into different connected components. Afterwards, some connected components are merged by comparing the size of each connected component with a fixed threshold. However, there may still be some misclassification around the text characters after this process. Third, we remove these misclassifications by morphological erosion where the structure element is a 5×5 square window. At this point, we have a reference map that marks the potential raster regions of the continuous-tone RGB color space image. Fourth, we use this map to correct the initial object map. The corrected object map is the final output of our algorithm.

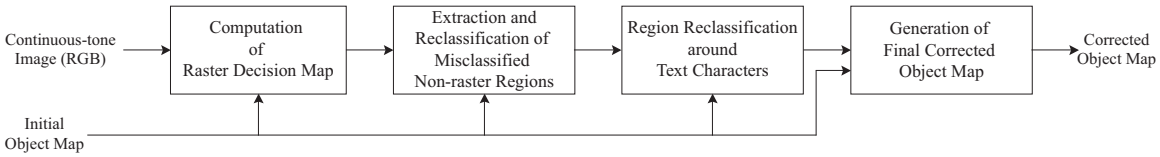

Fig. 2.6. Block diagram of segmentation-based object map correction algorithm (SBOMCA).

2.3.1 Computation of Raster Decision Map

In this section, three different maps, visual importance map, neutralness map and text map are discussed. The visual importance map is formed by using the two features, second order derivative and saliency. Then, neutralness map is generated by calculating the neutralness of the pixel in the continuous-tone RGB image. Finally, the text map is obtained by extracting the text information form the initial object map. The detail discussions for each map are given in the following. Then, a raster decision map (RDM) is defined based on these three maps. Fig. 2.9 illustrates the result obtained from these features for an example continuous-tone RGB image $f[m, n; i], i = R, G, B$ (Fig. 2.9a) and initial object map $o_{initial}[m, n]$ (Fig. 2.9b). The color code for the object map is given in Table 2.1.

Visual Importance Map

In this section, we discuss the visual importance map that is formed by the second order derivative and saliency. We then show how we calculate second order derivative and saliency in the following.

In the continuous-tone RGB page image, smooth areas tend to have lower color variation, and detail areas have higher color variation. The local activity in the image provides a means to quantify this difference. The local activity in an image can be estimated by edge detection algorithms. In this study, a number of edge operators were considered such as the Sobel operator [15], Canny edge detector [42], Laplacian of Gaussian [43], and the first/second order derivative. Since the Sobel operator, Canny edge detector and Laplacian of Gaussian all require relatively greater computational effort, we use the second order derivative as the edge detection method to extract the edge information in this step.

We compute the second order derivative of the continuous-tone image in each of the three channels, respectively. Moreover, to further increase the computational efficiency, we only compute the second derivative at pixels that are classified as raster

in the initial object map. In the following mathematical expression, we denote the initial object map as $o_{initial}[m, n]$. Instead of only computing the horizontal or vertical second order derivative, the second order derivative of the continuous-tone RGB color space image in each of three channels is defined as the maximum of the absolute horizontal and absolute vertical second order derivatives. The horizontal second order derivative can written as

$$f''_h[m, n; i] = f[m, n + 1; i] - 2f[m, n; i] + f[m, n - 1; i], \quad (2.2)$$

where $f[m, n; i]$ is the pixel value of the i^{th} channel of the continuous-tone RGB color space image and $f''_h[m, n; i]$ is the horizontal second order derivative of the i^{th} channel. On the other hand, the vertical second order derivative can represented as

$$f''_v[m, n; i] = f[m + 1, n; i] - 2f[m, n; i] + f[m - 1, n; i], \quad (2.3)$$

where $f''_v[m, n; i]$ is the vertical second order derivative of the i^{th} channel of the continuous-tone RGB color space image. Finally, the second order derivative of the continuous-tone RGB color space image in each of three channel is defined by

$$f''[m, n; i] = \max\left(|f''_h[m, n; i]|, |f''_v[m, n; i]|\right). \quad (2.4)$$

The idea of saliency is a feature to represent objects or regions that are visually most important in a given document. The way we compute the saliency value map $S[m, n]$ for a given image follows Achanta et al [44]. This method is computationally efficient and effective in detecting the salient regions. As defined by Achanta et al [44], the algorithm contains two steps. First, the given image is converted to an L*a*b* color space image. Then, the transformed image is blurred with a Gaussian filter. Finally, the saliency value at each pixel is computed as the squared Euclidean distance between the L*a*b* value at that pixel in the blurred image, and the average L*a*b* value of the entire blurred image. In our implementation, we reduce the computational effort by directly computing the saliency value of each pixel of the L*a*b* color space image without blurring by a Gaussian filter. In addition, we only compute the average

L*a*b* value of a 5×5 window centered at the current pixel in the L*a*b* color space image, instead of computing the average over the entire image. Thus, we have

$$\begin{aligned} S[m,n] &= \left(L[m,n] - \sum_{k=-2}^{k=2} \sum_{l=-2}^{l=2} L[m+k, n+l] \right)^2 + \\ & \left(a[m,n] - \sum_{k=-2}^{k=2} \sum_{l=-2}^{l=2} a[m+k, n+l] \right)^2 + \\ & \left(b[m,n] - \sum_{k=-2}^{k=2} \sum_{l=-2}^{l=2} b[m+k, n+l] \right)^2 . \end{aligned} \tag{2.5}$$

An alternative for L*a*b* color space is to compute NIQ [45] color space to reduce the computation effort of transforming RGB to L*a*b*. The transformation can be expressed as

$$\begin{bmatrix} N \\ I \\ Q \end{bmatrix} = \begin{bmatrix} 1/3 & 1/3 & 1/3 \\ 1/2 & -1/2 & 0 \\ 1/4 & 1/4 & -1/2 \end{bmatrix} \begin{bmatrix} R \\ G \\ B \end{bmatrix} \tag{2.6}$$

However, the range of the NIQ is different from the Lab. The range of L, a and b are $0 \leq L \leq 100$, $-128 \leq a \leq 128$ and $-128 \leq b \leq 128$. On the other hand, the range of N, I and Q are $0 \leq N \leq 255$, $-128 \leq I \leq 128$ and $-128 \leq Q \leq 128$. Therefore, we rescale the value of N from 0 to 100 and rewrite Eq. 2.6 as follow

$$\begin{bmatrix} N \\ I \\ Q \end{bmatrix} = \begin{bmatrix} 100/255 & 0 & 0 \\ 0 & 1 & 0 \\ 0 & 0 & 1 \end{bmatrix} \begin{bmatrix} 1/3 & 1/3 & 1/3 \\ 1/2 & -1/2 & 0 \\ 1/4 & 1/4 & -1/2 \end{bmatrix} \begin{bmatrix} R \\ G \\ B \end{bmatrix} \tag{2.7}$$

Therefore, we can use the values of NIQ to approximate the values of Lab, and rewrite the Eq. 2.5 by

$$\begin{aligned} S[m,n] &= \left(N[m,n] - \sum_{k=-2}^{k=2} \sum_{l=-2}^{l=2} N[m+k, n+l] \right)^2 + \\ & \left(I[m,n] - \sum_{k=-2}^{k=2} \sum_{l=-2}^{l=2} I[m+k, n+l] \right)^2 + \\ & \left(Q[m,n] - \sum_{k=-2}^{k=2} \sum_{l=-2}^{l=2} Q[m+k, n+l] \right)^2 . \end{aligned} \tag{2.8}$$

Based on Eq. 2.4 and Eq. 2.8, we generate the visual importance $v[m,n]$ map as follow

$$\begin{aligned} v[m,n] &= \mathcal{I}\Big(\max_{\substack{(k,l)\in[-2,2]\times[-2,2] \\ i=R,G,B}} f''[m+k,n+l;i] > T_{activity} \Big) \cap \\ & \quad \mathcal{I}\big(S[m,n] > T_{saliency}\big)\,, \end{aligned} \tag{2.9}$$

where $\mathcal{I}(\cdot)$ is the indicator function. The fixed thresholds $T_{activity}$ and $T_{saliency}$ are chosen empirically to yield the best image quality. Here $T_{activity}$ is chosen to be 4, and $T_{saliency}$ is chosen to be 5.

Neutralness Map

In the new imaging pipeline as shown in Fig. 2.3, the color channel conversion block transforms the RGB color space image into CMYK color space image. To better reproduce the print quality, different regions in the continuous-tone RGB rasterized page image are applied with different color maps for transforming RGB color space into CMYK color space. We summarize the color maps for different region in Table 2.2. The reason for rendering raster areas with process neutral is because K-only process may have contour or gloss changes in the transitions from gray black to color regions. Process grays are smooth and blend well with surrounding colors, so transitions in gradients from highlights to shadows is smooth with uniform gloss. On the other hand, text and graphic regions should apply K-only process because process neutral may introduce color misregistration and halo artifacts [40,41]. Therefore, K-only process keeps text lines sharp and reduces the impact of color plane misregistration.

However, different color appearance is perceived when we apply different color maps to different regions, especially two adjacent regions, with the same color. In Fig. 2.7, we show an example to illustrate the color difference between two color maps, process neutral and K-only in rendering the printed page. In Fig. 2.7(a), it is rendered by using the process neutral color map. On the other hand, Fig. 2.7(b) is

Table 2.2
Color map for different object types

Object Type	Raster	Text, Vector and Background
Color Table	Process-Neutral	K-only

rendered by K-only process. We can see a huge color difference in the upper region of the page, which is a region that should be classified as raster. If we render that raster region with two different color maps because of our object map correction algorithm, color difference can be detect easily, and it causes the artifact. To avoid this issue, we need a mechanism to prevent.

The color difference mainly appears around the neutral axis (with equal RGB value). To avoid this issue, the object type of a particular pixel in the initial object map should not be changed when R, G and B values are similar. To determine their similarity, we apply the following decision rule. If the maximum absolute difference between each of two color values is smaller than a certain threshold $T_{Neutral}$, the pixel value of the neutralness map $\eta[m,n]$ is set to be 1. If the maximum absolute difference between each of two color values is greater than a certain threshold $T_{Neutral}$, the pixel value of the neutralness map $\eta[m,n]$ is set to be 0 Then, we obtained the neutralness map $\eta[m,n]$ as follow

$$\begin{aligned}\eta[m,n] &= \mathcal{I}\Big(\max\big\{|f[m,n;R]-f[m,n;G]|,|f[m,n;G]-f[m,n;B]|,\\ &\qquad |f[m,n;R]-f[m,n;B]|\big\} < T_{Neutral}\Big),\end{aligned} \tag{2.10}$$

where $T_{Neutral}$ is chosen empirically to be 10.

Text Map

Initial object map is one of the input to our object map correction algorithm. As described in the PRELIMINARIES section, the initial object map is formed by

(a) (b)

Fig. 2.7. Illustration of the color difference between applying different color maps to render the printed page (a) The image is rendered by the process neutral color map. (b) The image is rendered by the K-only color map.

Table 2.3
Color code for the raster decision map

	Black	White
Object Type	Non-Raster	Potential Raster

extracting object information from the rasterization process. In this map, it includes the information of the text regions. Thus, we formed the text map as follow

$$t[m,n] \;=\; \mathcal{I}\big(o_{initial}[m,n] = \text{“}text\text{”}\big) \tag{2.11}$$

Raster Decision Map

We use the three maps mentioned in the previous section to compute a raster decision map. The raster decision map is defined as

$$o_{RDM}[m,n] \;=\; v[m,n] \cup \eta[m,n] \cup t[m,n]\,, \tag{2.12}$$

where $o_{RDM}[m,n]$ is the raster decision map, $v[m,n]$ is the visual importance map, $\eta[m,n]$ is the neutralness map and $t[m,n]$ is the text map. $\cup$ is the “OR” operation. If the pixel value at a particular pixel in the raster decision map is 1, we consider that pixel to be *potential raster*. If the pixel value at a particular pixel in the raster decision map is 0, we consider that pixel to be *non-raster*. The color code for the raster decision map is provided by Table 2.3. Figure 2.9(c) shows the raster decision map obtained for the continuous-tone RGB image in Fig. 2.9(a).

2.3.2 Extraction and Reclassification of Misclassfied Non-raster Regions

As the red box indicated in Fig. 2.9(c) and the red pixels in the zoom-in image, Fig. 2.9(g), these red pixels should be classified as *potential raster* rather than *non-raster*. Segmentation-based method needs to applied to the Fig. 2.9(c) to find these regions.

The objective of this step is to modify *non-raster* regions that should belong to *potential raster* regions. To extract these regions, we apply connected component analysis [15] (CCA) in this step. We use a 4-connected components, so the neighborhood of a point $[m, n]$ is defined as

$$\partial[m,n] \;=\; \big\{[m-1,n],[m+1,n],[m,n-1],[m,n+1]\big\}\,. \tag{2.13}$$

At first, a labeled connected component image is initialized. Given a pixel P_1, a class label is assigned to the connected component of P_1 that is a path of M pixels P_1, P_2, ..., P_M in a binary image such that for $1 \leq i \leq M$, P_{i-1} and P_i are connected neighbors. The connected neighbors of P are defined as

$$c(P) \;=\; \{Q \in \partial P|\ |x_P - x_Q| < T_{CCA}\}\,, \tag{2.14}$$

where P and Q are two points in the binary image, x_P and x_Q are the pixel value of P and Q, and T_{CCA} is a fixed threshold. In this paper, we define T_{CCA} is equal to 1 because it is sufficient to differentiate objects in a binary image. The corresponding pixels of this connected component in the labeled connected component image are labeled. Then, a new class label is assigned to another connected set by starting at an unlabeled pixel. After iterating through the whole image, the CCA labels each pixel with a index associated with its connected component.

To modify *non-raster* regions that should belong to *potential raster* regions, we first apply CCA to the raster decision map $o_{RDM}[m, n]$. Since our objective is to modify *non-raster* regions, we only run the CCA on those pixels are labeled as *non-raster* in the raster decision map. The CCA labels each connected component of *non-raster* regions with a different index. Meanwhile, we store the size of these connected components when we extract them. A simple decision rule is defined to determine the object type of each connected component. If the size of a particular connected component is smaller than a certain threshold T_2, we label this connected component to be *potential raster*. Otherwise, we do not make any change to this connected component. If the size of a connected component is larger than the predefined threshold T_{merge},

this object is highly likely to be the background or a graphic in the input image; and it should be classified as *non-raster*. Lastly, we merge connected components that are smaller than the threshold T_{merge} to be *potential raster*. The threshold T_{merge} is 6% of area of the entire image, and is chosen empirically. Figure 2.9(d) shows the resulting image. We call it the raster decision map[1] $o_{RDM^1}[m, n]$.

2.3.3 Region Reclassification around Text Characters

There are two issues with the raster decision map[1] $o_{RDM^1}[m, n]$. As can be seen in the zoomed images of Fig. 2.9(h) and Fig. 2.9(i), there are misclassifications around the text character. First, pixels in the closed-bowl of the text character are classified as *potential raster*; however, they should be classified as *non-raster*. Secondly, the outside boundary of the text character is enlarged because of the thresholding.

In this study, we only reclassify the outside boundary of the text character without modifying the misclassification in the closed-bowl of the text character. If the closed-bowl regions are reclassified into *non-raster*, these regions will be applied low frequency screen when we halftone the page image. It is easy to see the halftone texture when background regions are applied high frequency screen. We use two examples in Fig. 2.8 to illustrate this phenomena. In Fig. 2.8(a), the closed-bowl region is halftoned with low frequency screen and background is halftoned with high frequency screen. Figure. 2.8(c) is the zoom-in image of the red box in the Fig. 2.8(a), and Fig. 2.8(d) is the object map of the Fig. 2.8(c). On the other hand, the Fig. 2.8(b), the closed-bowl region is halftoned with high frequency screen and background is halftoned with low frequency screen. Figure. 2.8(e) is the zoom-in image of the red box in the Fig. 2.8(b), and Fig. 2.8(f) is the object map of the Fig. 2.8(e). In the first example, the halftone texture in Fig. 2.8(c) is easy to be perceived. Therefore, we should not reclassify the closed-bowl region to be *non-raster*, and keep them as *potential raster*. In the second example, we show the other situation that the adjacent

regions are applied with different halftone screen. The print quality is good enough under such setting.

Since the goal of this step is to modify pixels classified as *potential raster* on the outside boundary of the text characters, we apply the morphological operator, erosion [46], to reclassify those pixels. Erosion operator is the morphological transformation that combines the binary image and the structuring element using the vector subtraction [46]. In the following, the binary image is denoted as A and structuring element is denoted as B. With set A and B in Z^2, the erosion [46] of A by B is defined as

$$A \ominus B \quad = \quad \{z \in Z^2 | z + b \in A, \forall b \in B\} . \tag{2.15}$$

The binary image A is the merged thresholded edge map $o_{RDM^1}[m, n]$ and the structuring element B is a 5×5 square structuring element. The resulting image is shown in Fig. 2.9(e) and Fig. 2.9(j). This is used as the reference to correct the initial object map $o_{initial}[m, n]$. We name it the raster decision map[2] $o_{RDM^2}[m, n]$.

2.3.4 Generation of Final Corrected Object Map

The last step of the object map correction algorithm is to modify the initial object map, which is generated by the raster image processor (RIP). Based on the concept of object-oriented halftoning, we want to apply halftone screens with different frequencies to different parts of the document page to improve the overall print quality. A correct object map is needed to achieve this goal. However, there may be misclassification in raster regions in the initial object map.

The issue with the initial object map is that smooth areas in the input document page are classified as raster when they should be classified as vector. The objective is to reclassify those pixels that truly belong to vector, but which are classified as raster in the initial object map. For each pixel in the image, we first check whether it is raster or not in the initial object map $o_{initial}[m, n]$. If yes, we check the corresponding pixel in the raster decision map[2] $o_{RDM^2}[m, n]$ that has been generated as discussed

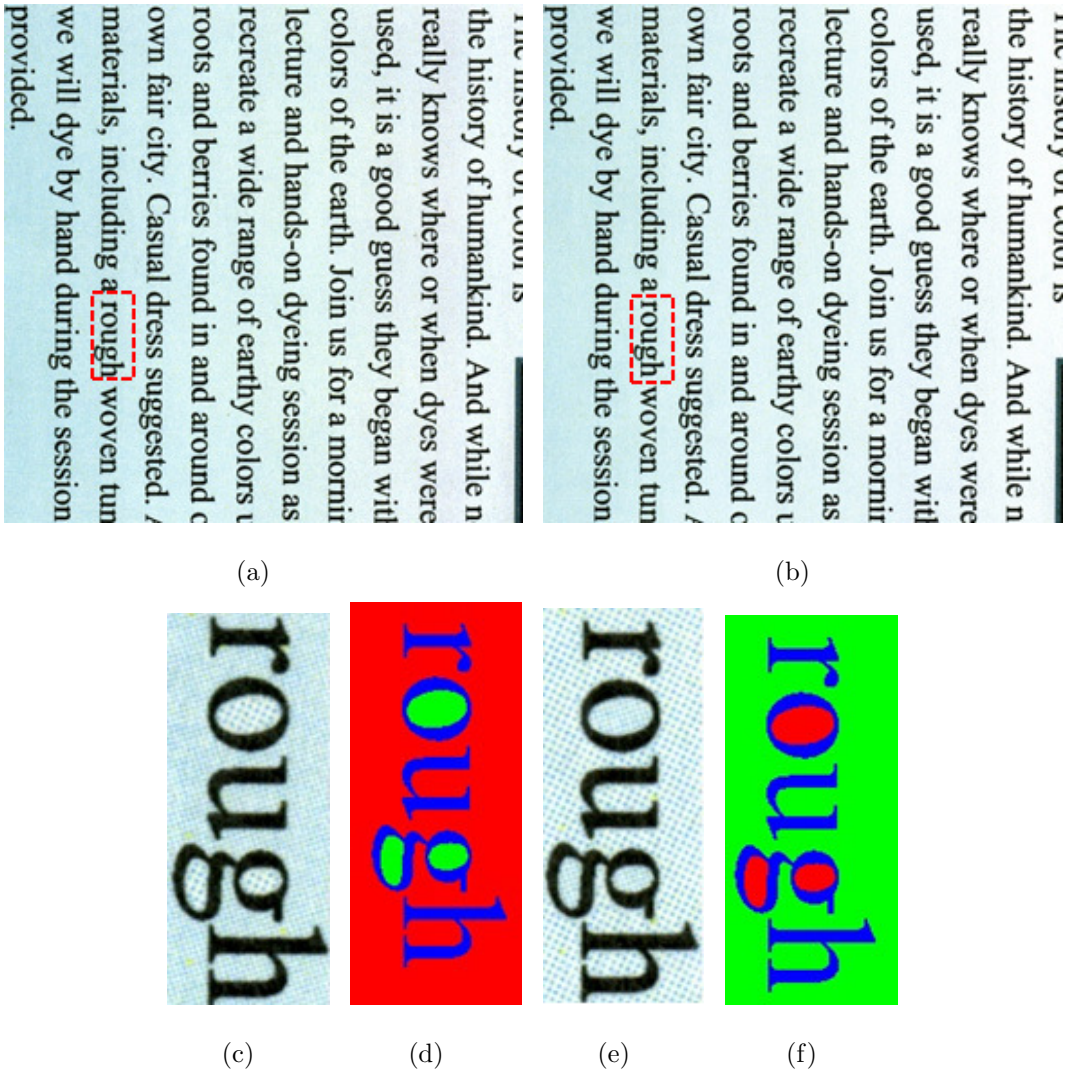

Fig. 2.8. Illustration of the print quality of different halftone screen that affects the visual appearance in the closed-bowl of the text character (a) A print page that the closed-bowl regions are halftoned with high frequency screen and the background regions are halftoned with low frequency screen. (b) A print page that the closed-bowl regions are halftoned with low frequency screen and the background regions are halftoned with high frequency screen. (c) The zoom-in character in (a). (d) The corresponding object map of (c). (e) The zoom-in character in (b). (f) The corresponding object map of (e).

earlier in this section. If the corresponding pixel is *potential raster*, we do not make any change. Otherwise, we change the pixel type to be *vector*. The corrected object map is shown in Fig. 2.9(f). We denote it as $o_{corrected}[m, n]$. With the corrected object map, we can apply object-oriented halftoning, and improve the overall print quality.

2.4 Experimental Results

The target printer in this study is the HP Color LaserJet CM4540 MFP printer at 600 dpi. To print the CMYK halftoned image, which is halftoned by the object-oriented halftoning with blending algorithm and adaptive halftoning algorithm (AHT) [19], we use the backdoor printing path. It directly stores the halftoned image in the buffer which is in the memory of the printer, and it is then transmitted to the formatter. It sends the video signal to control the laser driver board for reproduction. As we print the input document, it is scanned with a EPSON Expression 10000XL at 1200dpi.

The new imaging pipeline was applied to a large number of PDF files. Here, we provide some experimental results to show the benefits of our algorithm. The test PDF files are obtained from the Purdue University e-Archives and Hewlett-Packard Company. The files are interpreted by the raster image processor (RIP) producing two images: the initial object map and the continuous-tone RGB color space image. These two images are the inputs to the segmentation-based object map correction algorithm (SBOMCA). We have shown the step-by-step results in Fig. 2.9, as we discussed the segmentation-based object map algorithm. Currently, we have tested the SBOMCA on 74 different PDF files. Here we present three different samples to illustrate the benefits of our algorithm. The examples are shown in Fig. 2.10. Figures 2.10(a), 2.10(d), and 2.10(g) are continuous-tone RGB color space images. Figures 2.10(b), 2.10(e), and 2.10(h) are initial object maps generated by the RIP. Figures 2.10(c), 2.10(f), and 2.10(i) are the corrected object maps. The corrected

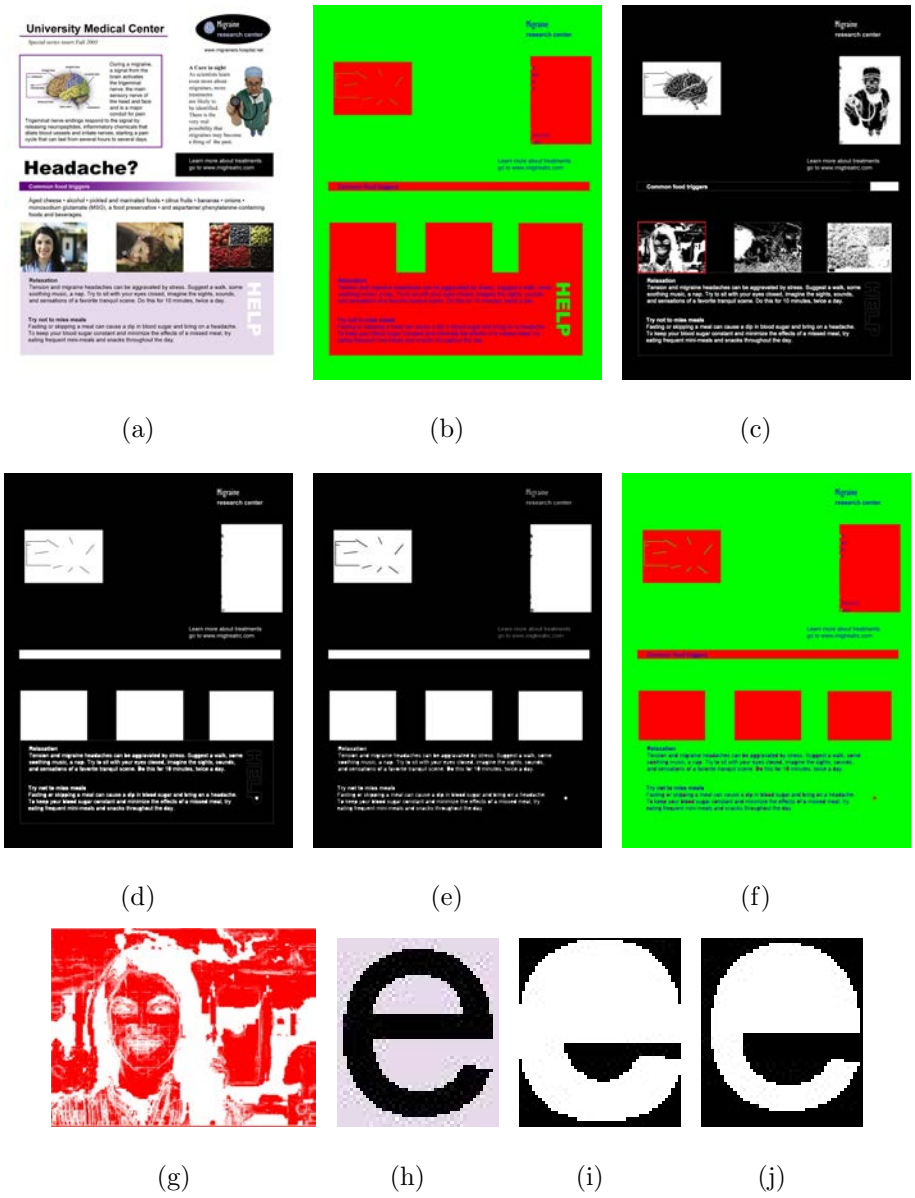

Fig. 2.9. Illustration of the segmentation-based object map correction algorithm (a) Continuous-tone RGB color space image. (b) Initial object map. (c) Raster Decision map. (d) Raster Decision map[1]. (e) Raster Decision map[2]. (f) Corrected object map. (g) Red pixels in the zoom-in image of the raster Decision map indicate that the regions should be classified as *potential-raster*. (h)The zoomed-in image of the text character in the RGB color space image. (i) The zoomed-in image of the text character in the raster Decision map[1]. (j) The zoom-in image of reclassifying around the text characters.

object maps show that smooth areas in the initial object maps have been reclassified effectively by our algorithm.

Lastly, we compare the print quality between using the new imaging pipeline and conventional imaging pipeline. The new imaging pipeline applies the object-oriented halftoning based on the corrected object map on the given page. We use the screen design based on Park et al. [23]. The detail screen set is using cyan 190 lpi, magenta 190 lpi, yellow 200 lpi, and black 212 lpi. The corresponding vectors are cyan: $\overrightarrow{d_1} = (3, -1)$, $\overrightarrow{d_2} = (1, 3)$, magenta: $\overrightarrow{d_1} = (1, -3)$, $\overrightarrow{d_2} = (3, 1)$, yellow: $\overrightarrow{d_1} = (3, 0)$, $\overrightarrow{d_2} = (0, 3)$, and black: $\overrightarrow{d_1} = (2, 2)$, $\overrightarrow{d_2} = (-2, 2)$. The smooth screen set is using cyan 135 lpi, magenta 135 lpi, yellow 212 lpi, and black 150 lpi whose vectors are cyan: $\overrightarrow{d_1} = (4, 2)$, $\overrightarrow{d_2} = (-2, 4)$, magenta: $\overrightarrow{d_1} = (4, -2)$, $\overrightarrow{d_2} = (2, 4)$, yellow: $\overrightarrow{d_1} = (2, 2)$, $\overrightarrow{d_2} = (-2, 2)$, and black: $\overrightarrow{d_1} = (4, 0)$, $\overrightarrow{d_2} = (0, 4)$. On the other hand, the conventional imaging pipeline applies high frequency screens on the whole given page. The high frequency screen set is same as the new imaging pipeline. The following examples show the benefit of using the new imaging pipeline. In Fig. 2.11, there are mottles in two images, which prints with the conventional imaging pipeline, on left hand side. By using the new imaging pipeline, mottles are reduced due to applying low lpi screen on the smooth area. In Fig. 2.12(a), there are streaks indicated in black ellipses. These streaks are reduced in Fig. 2.12(b).

2.5 Conclusion

In this paper, we proposed a systematic method to modify the initial object map for object-oriented halftoning. We first described the miscellaneous image objects that have different characteristics in a typical page content, and the idea of object-oriented halftoning. We then discussed the new imaging pipeline for laser EP printers and briefly reviewed the seamless halftoning, which reduces the undesired jagged patterns along the boundary of two different halftone screens. To apply object-oriented halftoning, we retrieve the object type information from the page description language

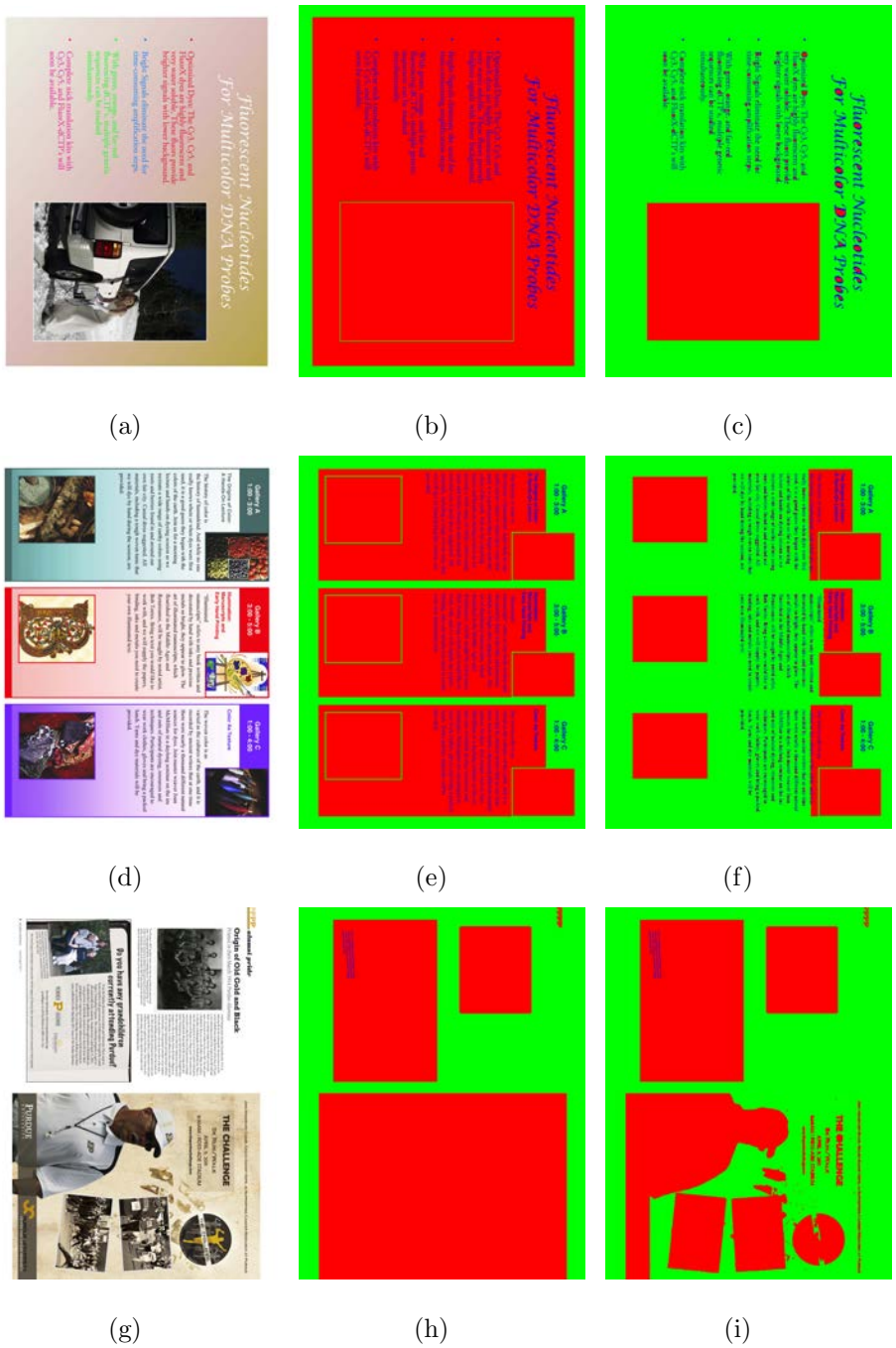

(a) (b) (c)

(d) (e) (f)

(g) (h) (i)

Fig. 2.10. Examples comparing the initial object map and corrected object map (a) Continuous-tone RGB color space image. (b) Initial object map. (c) Corrected object map. (d) Continuous-tone RGB color space image. (e) Initial object map. (f) Corrected object map. (g) Continuous-tone RGB color space image. (h) Initial object map. (i) Corrected object map.

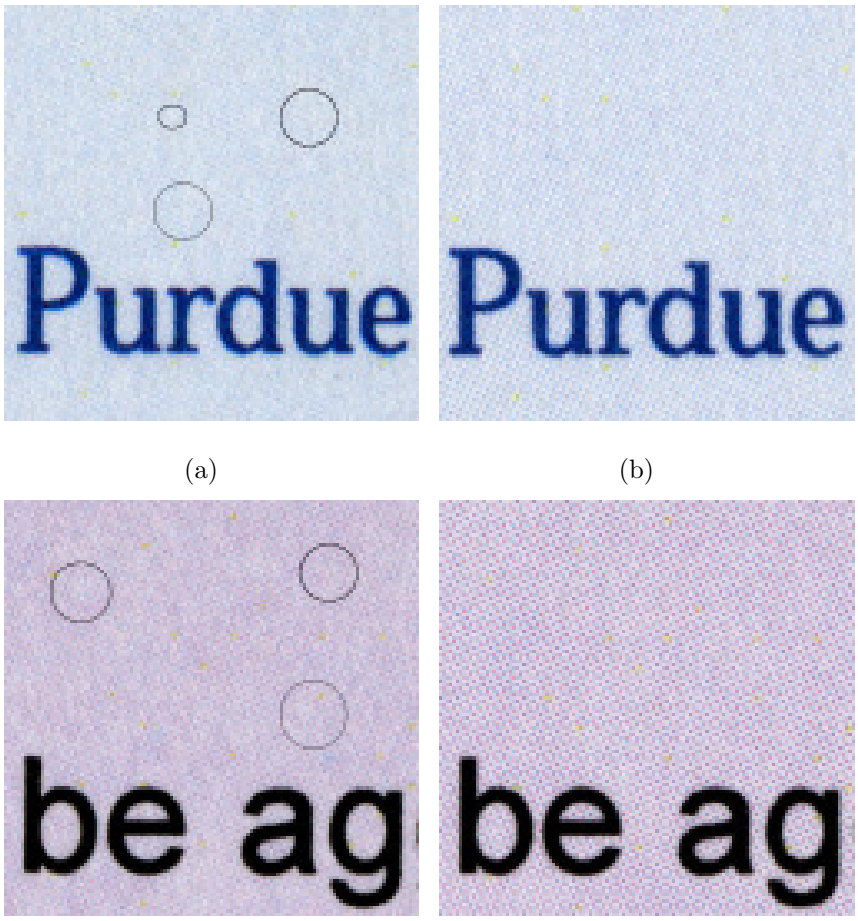

Fig. 2.11. Image quality between the conventional and new imaging pipeline (a) High frequency screen only: mottles are observed. (b) Object-oriented halftoning: mottles reduction. (c) High frequency screen only: mottles are observed. (d) Object-oriented halftoning: mottles reduction.

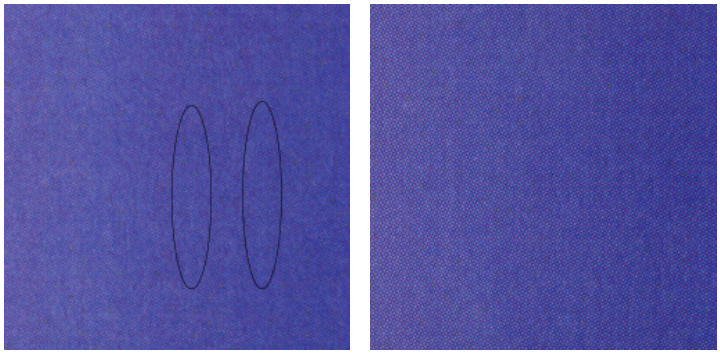

(a) (b)

Fig. 2.12. Print samples with streaks (a) High frequency screen only: streaks are observed. (b) Object-oriented halftoning: streaks reduction.

(PDL) to create an initial object map. However, the object type information in the initial object map may be incorrect. Specifically, smooth areas that should be vector are classified as raster. Therefore, we introduce a more efficient segmentation-based object map correction algorithm (SBOMCA) to correct the initial object map than in Chen [37]. The algorithm combines four features extracted from the continuous-tone RGB color space image and the initial object map, segmentation algorithm that uses connected component analysis and morphological erosion. Finally, we test the algorithm on a variety of contents in PDF files. Preliminary experimental results confirm the ability of our algorithm to yield a properly corrected object map.

3. UNDERSTANDING IMAGE GRAININESS

3.1 Introduction

With the emergence of the high-end digital printing technologies such as HP Indigo Technology that offers a different printing solution from laser electrophotographic (EP) printers, HP Indigo Technology aims to achieve the print quality as commercial offset presses. The imaging system of HP Indigo Technology are shown in Fig. 3.1 [47]. Instead of using toner in the commercial Laser EP printers, HP Indigo Technology uses the liquid electrophotography based on ElectroInk® [47]. The imaging processes are the following. The photo imaging plate (PIP) is electronically charged. The laser beam unit emits laser light that exposes on the PIP, and a latent image is created [47]. Various colored ink development stations have the ink developed individually onto the latent image. Afterward, the electronic field is used to transfer the ink to the hot blanket from the PIP. The liquid carrier in ElectroInk® is evaporated by the heat that creates a thin ink film [47]. Finally, the thin ink film on the hot blanket is transferred to the substrate by pressure and tackiness [47]. These steps complete the imaging process.

In addition to the different printing process from the laser EP printers, a different type of screen, which is one of various halftoning techniques used in HP Indigo Techn-logy. Halftoning is the process of rendering continuous-tone images with the limited number of tone levels. Mostly, the number of toner is two, which indicates a dot on the paper is either printed or not printed. Halftoning utilizes the low-pass nature of the human visual system, which can blur the halftone pattern, so that the halftone image is perceived as a continuous-tone image when we view from a distance.

The halftoning algorithms can be categorized into three different approaches: point operation (screening) [28, 48], neighborhood processes (error diffusion) [49] and

iterative processes (for example, DBS [50]). Screening is one of the most widely used in laser EP printers. Because of the innately unstable printing processes, screening is popular because it, which generates periodic, clustered-dot halftone textures provides a better rendering on laser EP printers. Moreover, screening provides a better control of moire by the superposition of different colorant planes [53]. In commercial offset printing, the imaging plates are all written using a high-resolution, laser-marking system. The screens for different colorants C, M, Y and K can all be obtained by a single screen that is rotated to the ideal angles of 0, 30, 45, and 60 degrees [53]. The screen frequency of the screen, which the commercial offset printer uses can be specified in a certain range.

However, the digital imaging system can not provide a high-resolution addressability that is same as commercial offset presses. This makes the screen angles and frequencies are limited. To reproduce dot cluster with screen under this circumstance when expressed in units of printer-addressable pixels, the elements of the periodicity matrix must be integer-valued [53]. This type of screen is called regular screens. They tile the plane into identical microcells that align with the printer-addressable lattice [53]. However, the regular screens have limited ability to approximate the screens sets used in commercial offset presses. To better approximate the screen sets of the commercial offset presses, irregular screens are used, which are used in HP Indigo Technology. In contrast to the elements of periodicity matrix of the regular screen have integer numbers, the elements of irregular screen's periodicity matrix are rational numbers when expressed in units of printer-addressable pixels. Recently, Tang et al [53] provides a procedure to design the irregular screen.

With such a high-end digital imaging system, graininess is still an important issue that HP Indigo Technology can not have the same smoothness as the commercial offset presses. Graininess describes the subjective perception of noise in a given image [51]. ISO 13660 standard defines graininess as the non-periodic high frequency noise, in contrast to mottle, which is defined as non-periodic low frequency noise [52]. In addition, the standard defines that graininess has aperiodic fluctuations of

density at a spatial frequency greater than 10 cycle-per-inch (cpi). Different graininess metrics have been proposed [51, 54, 55] to describe graininess of halftone images. However, the analysis of how halftone textures introduce image graininess has not to our knowledge been discussed in the literature. Therefore, we provide two different approaches analyzing the halftone textures in the frequency and the spatial domain to understand image graininess. In addition to analyze halftone textures, we conduct experiments to examine HP Indigo Technology by printing the same halftone pattern on different substrates, glossy and polyester media to see how the combinations of halftone textures and substrates affect the graininess measurement.

In this chapter, we report on a study to understand the relationship between image graininess and halftone technology and marking technology. We provide three different approaches to understand image graininess. The rest of this paper is organized as follows. In the next section, we give a brief introduction to screening and printer model. Then, we perform a Fourier-based analysis of regular and irregular periodic, clustered-dot halftone textures in the Section 3.3. Subsequently, a spatial-statistics approach is described in Section 3.4. In Section 3.5, experiments on graininess measurement on different substrates are illustrated. Finally, we conclude in the Section 3.6.

3.2 Preliminaries

In this section, we briefly introduce printer model and screening.

3.2.1 Pinter Model

Let $(\mathbf{x}) = (x, y)^T$ and $\mathbf{m} = [m, n]^T$ indicate the continuous and discrete coordinates, respectively, where the units of $(\mathbf{x})$ and $[\mathbf{m}]$ are inches and printer-addressable pixels, respectively. We use $f[\mathbf{m}]$ to denote the continuous-tone image and $g[\mathbf{m}]$ to represent the halftoned version of $f[\mathbf{m}]$. The image $f[\mathbf{m}]$ takes the discrete values from $\{0, \frac{1}{L-1}, \frac{2}{L-1}, \ldots, 1\}$, where L is the total number of gray levels. On the other

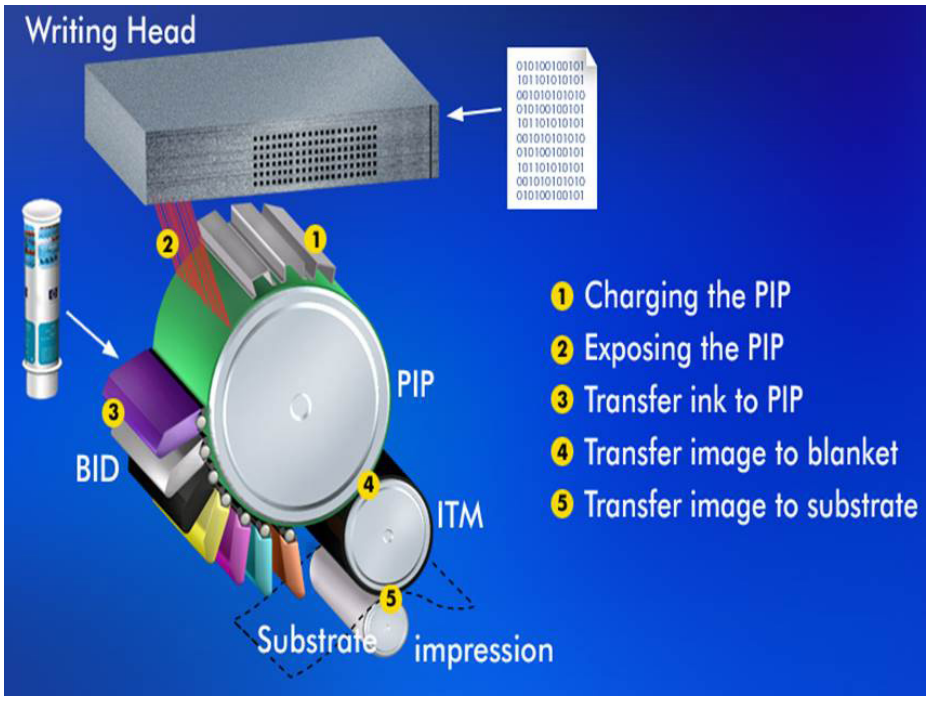

Fig. 3.1. Printing engine of a HP Indigo digital press. [47]

hand, $g[\mathbf{m}]$ takes the values from either 0 (white) or 1(black). We specify a ideal printer dot profile to be a square dot, and it is defined as

$$\begin{aligned} p_{\text{dot}}(\mathbf{x}) &= \text{rect}\,(\mathbf{x}/R) \\ &= \text{rect}(x/R)\text{rect}(y/R)\,. \end{aligned} \tag{3.1}$$

The rendered image $f(\mathbf{x})$ of $f[\mathbf{m}]$ can be expressed as

$$f(\mathbf{x}) = \sum_{\mathbf{m}\in Z^2} f[\mathbf{m}]\; p_{\text{dot}}(\mathbf{x} - \mathbf{m}R)\,, \tag{3.2}$$

where the parameter R is the horizontal and vertical distance between printer-addressable pixels in units of inches. Similarly, we have

$$g(\mathbf{x}) = \sum_{\mathbf{m}\in Z^2} g[\mathbf{m}]\; p_{\text{dot}}(\mathbf{x} - \mathbf{m}R)\,. \tag{3.3}$$

3.2.2 Screening

Screening is a point operation. The screening process generates the halftone image by thresholding the discrete-space continuous-tone image $g[\mathbf{m}]$ with a threshold array $t[\mathbf{m}]$ pixel by pixel. The discrete-space halftone image is defined as follow

$$g[\mathbf{m}] = \begin{cases} 1, & \text{if } f[\mathbf{m}] \geq t[\mathbf{m}] \\ 0, & \text{else} \end{cases}, \tag{3.4}$$

where $t[\mathbf{m}]$ is the threshold array and its periodicity is based on the periodicity matrix N, i.e., $t[\mathbf{m} + \mathbf{Nq}] = t[\mathbf{m}], \forall \mathbf{q} \in Z^2$.

3.3 Fourier-based Analysis of Regular and Irregular Periodic, Clustered-dot Halftone Textures

In this section, we develop a Fourier-based approach to analyze the regular and irregular periodic, clustered-dot halftone textures, and define a metric to measure the nonuniformity of the given halftone pattern. First, we introduce two terminology, analog rendering and digital rendering. Analog rendering is a continuous-space

halftone image without sampling by the printer lattice. On the other hand, the digital rendering is obtained by sampling the analog rendering. Then, each sampled impulse is convolved by the printer dot profile, which is a 2-D rect function in our analysis as we discussed in Section 3.2. The tile vectors of the regular halftone textures is follow: $\mathbf{n_1} = [3; 3]$ and $\mathbf{n_2} = [-3; 3]$. On the other hand, The tile vectors of the irregular halftone textures is follow: $\mathbf{n_1} = [2; 11/3]$ and $\mathbf{n_2} = [-11/3; 2]$. The absorptance is 0.25 for both regular and irregular halftone images. Figure. 3.2 is an example to illustrate the difference of the analog rendering and digital rendering between regular and irregular halftone textures in spatial domain. Figure 3.2 (a) and (c) are the analog rendering of the regular and irregular halftone textures. We can see that the images are basically the same with slightly differences in angle and dot area because the tile vectors of the regular and irregular screen are different. Figure 3.2 (b) and (d) are the digital rendering of the regular and irregular halftone textures. We can see there is a huge difference between the two digital renderings due to the non-integer elements in the periodicity matrix of the irregular screen when expressed in units of printer-addressable pixels. In the following section, we analyze regular and irregular halftone textures in frequency domain.

3.3.1 Fourier Spectrum of a Digital-Rendered Continuous-space Halftone Image with Circular Dot Pattern

In this section, we analyze a continuous-space halftone image with the circular dot pattern, and derive the corresponding Fourier expression after a image being sampled by the printer lattice and rendered by a printer dot profile function. In the following, we use boldface lower case to represent vectors, and boldface upper case to denote matrices. In the following derivation, we use $(\mathbf{x}) = (x, y)^T$ to indicate continuous coordinates , where the units of $(\mathbf{x})$ is inches.

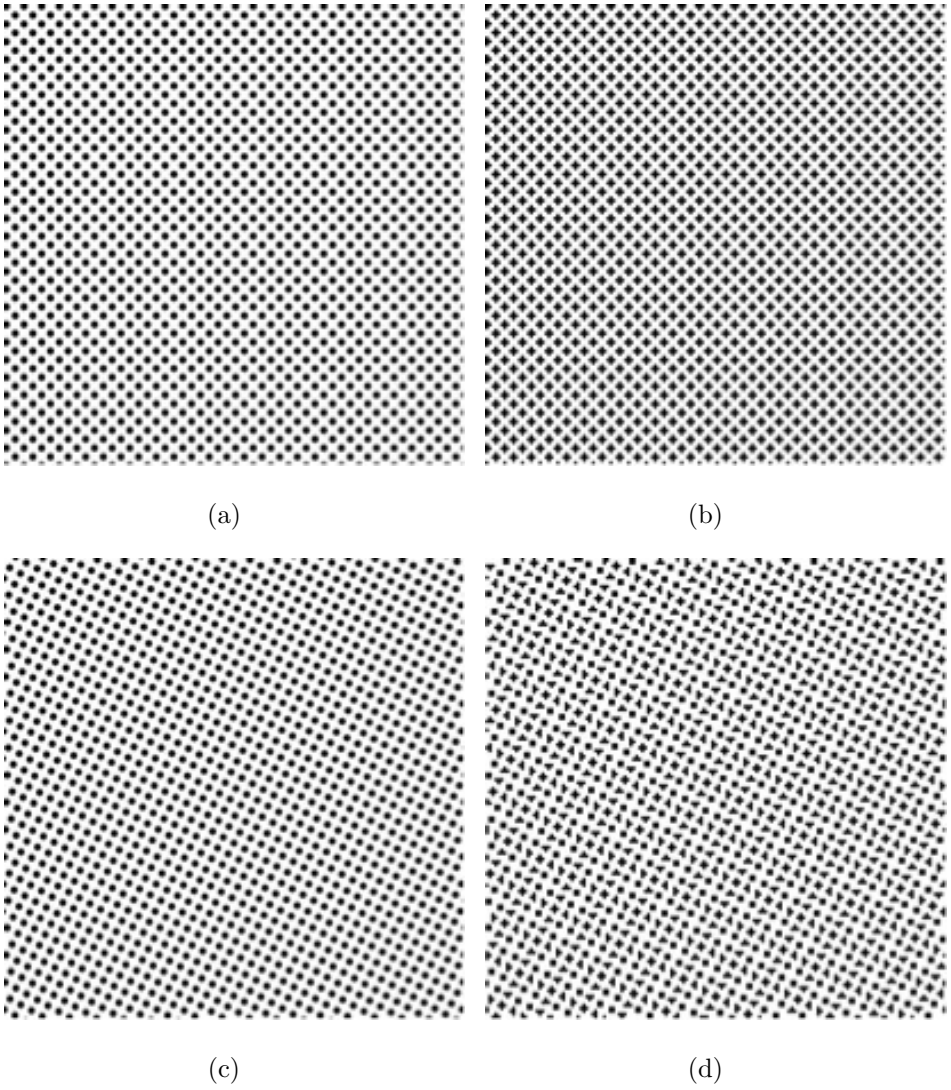

(a) (b)

(c) (d)

Fig. 3.2. Comparison of the difference the analog rendering and digital rendering between regular and irregular halftone textures in spatial domain. (a) The analog rendering of regular screen in spatial domain. (b) The digital rendering of regular screen in frequency domain. (c) The analog rendering of irregular screen in spatial domain. (d) The digital rendering of irregular screen in frequency domain.

We denote a continuous-space halftone image with circular dot pattern by $g(\mathbf{x})$, and it is defined as

$$g(\mathbf{x}) = \text{circ}(\mathbf{Mx}) * p(\mathbf{x}) \,, \tag{3.5}$$

where circle function $\text{circ}(\mathbf{x})$ is defined according to

$$\text{circ}(\mathbf{x}) = \begin{cases} 1, & \text{if } \sqrt{x^2+y^2} \leq \frac{1}{2} \\ 0, & \text{else} \end{cases} , \tag{3.6}$$

and the impulse function $p(\mathbf{x})$ is defined as

$$p(\mathbf{x}) \;\; = \;\; \sum_{\mathbf{k} \in Z^2} \delta(\mathbf{x} - R\mathbf{Nk}) \,, \tag{3.7}$$

where the matrix $\mathbf{N}$ is the periodicity matrix and the parameter R is the horizontal and vertical distance between printer-addressable pixels in units of inches. The matrix $\mathbf{M}$ is a diagonal matrix, and it is defined as

$$\mathbf{M} = \begin{bmatrix} \frac{1}{d} & 0 \\ 0 & \frac{1}{d} \end{bmatrix} , \tag{3.8}$$

where the parameter d is the diameter of the circle. Therefore, we can rewrite the continuous-space halftone image with circular dot pattern $g(\mathbf{x})$ as

$$\begin{aligned} g(\mathbf{x}) &= \text{circ}(\mathbf{Mx}) * p(\mathbf{x}) \\ &= \text{circ}(\mathbf{Mx}) * \sum_{\mathbf{k} \in Z^2} \delta(\mathbf{x} - R\mathbf{Nk}) \\ &= \sum_{\mathbf{k} \in Z^2} \text{circ}\big(\mathbf{M}(\mathbf{x} - R\mathbf{Nk})\big) \,. \end{aligned} \tag{3.9}$$

The image $g(\mathbf{x})$ is analog rendering, which we describe at the beginning of this section. Then, we compute the Continuous-Space Fourier transform (CSFT) of the continuous-

space halftone image with circular dot pattern $g(\mathbf{x})$, and CSFT of $g(\mathbf{x})$ is computed according to

$$\begin{aligned} G(\mathbf{u}) &= \int_{-\infty}^{\infty} g(\mathbf{x}) e^{-j2\pi \mathbf{u}^T \mathbf{x}}\, d\mathbf{x} \qquad (3.10) \\ &= \int_{-\infty}^{\infty} \sum_{\mathbf{k}\in Z^2} \mathrm{circ}\big(\mathbf{M}(\mathbf{x} - R\mathbf{N}\mathbf{k})\big) e^{-j2\pi \mathbf{u}^T \mathbf{x}}\, d\mathbf{x} \\ &= \sum_{\mathbf{k}\in Z^2} \int_{-\infty}^{\infty} \mathrm{circ}\big(\mathbf{M}(\mathbf{x} - R\mathbf{N}\mathbf{k})\big) e^{-j2\pi \mathbf{u}^T \mathbf{x}}\, d\mathbf{x} \\ &= \frac{1}{|\det(\mathbf{M})|} \sum_{\mathbf{k}\in Z^2} \mathrm{jinc}(\mathbf{M}^{-T}\mathbf{u}) e^{-j2\pi \mathbf{u}^T R\mathbf{N}\mathbf{k}} \\ &= \frac{1}{R^2 |\det(\mathbf{M})\det(\mathbf{N})|} \mathrm{jinc}(\mathbf{M}^{-T}\mathbf{u}) \sum_{\mathbf{k}\in Z^2} \delta(\mathbf{u} - \frac{1}{R}\mathbf{N}^{-T}\mathbf{k}), \qquad (3.11) \end{aligned}$$

where the CSFT of a circ function is a jinc function. The jinc function is defined as

$$\mathrm{jinc}(\mathbf{u}) = \frac{J_1(\pi\sqrt{u^2+v^2})}{2\sqrt{u^2+v^2}}, \qquad (3.12)$$

where J_1 is the Bessel function of the first kind with order 1.

Then, we sample the continuous-space halftone image with circular dot pattern $g(\mathbf{x})$ with the printer lattice, and convolve with the printer dot profile function. The rendered image of $g(\mathbf{x})$ is

$$g_p(\mathbf{x}) = \mathrm{comb}_{RR}[g(\mathbf{x})] * \mathrm{rect}(\frac{\mathbf{x}}{R}). \qquad (3.13)$$

The image $g_p(\mathbf{x})$ is the digital rendering, which we describe at the beginning of this section. The CSFT of $g_p(\mathbf{x})$ can be computed as follow

$$\begin{aligned} G_p(\mathbf{u}) &= \mathrm{rep}_{\frac{1}{R}\frac{1}{R}}[G(\mathbf{u})]\mathrm{sinc}(R\mathbf{u}) \\ &= \mathrm{sinc}(R\mathbf{u}) \sum_{\mathbf{m}\in Z^2} G(\mathbf{u} - \mathbf{V}\mathbf{m}) \\ &= \frac{\mathrm{sinc}(R\mathbf{u})}{R^2|\det(\mathbf{M})\det(\mathbf{N})|} \sum_{\mathbf{m}\in Z^2} \mathrm{jinc}\big(\mathbf{M}^{-T}(\mathbf{u} - \mathbf{V}\mathbf{m})\big) \\ &\quad \times \sum_{\mathbf{k}\in Z^2} \delta(\mathbf{u} - \mathbf{V}\mathbf{m} - \frac{1}{R}\mathbf{N}^{-T}\mathbf{k}), \qquad (3.14) \end{aligned}$$

where the matrix V is

$$\mathbf{V} = \begin{bmatrix} \frac{1}{R} & 0 \\ 0 & \frac{1}{R} \end{bmatrix} \qquad (3.15)$$

Now, we have the analytical expression of the CSFT of a analog rendering $G(\mathbf{u})$ and digital rendering $G_p(\mathbf{u})$. We plot the CSFT of the analog rendering and digital rendering of the regular and irregular screen in the following. The tile vectors of the regular screen are $\mathbf{n_1} = [3; 3]$ and $\mathbf{n_2} = [-3; 3]$. The screen angle and frequency of the regular screen are 45° and 191.4 line-per-inch (lpi), respectively. On the other hand, The tile vectors of the irregular halftone textures are $\mathbf{n_1} = [2; 11/3]$ and $\mathbf{n_2} = [-11/3; 2]$. The screen angle and frequency of the irregular screen are 61° and 194.4 lpi, respectively. The absorptance of the continuous-space halftone image is 0.25. To better show the spectrum, especially the low intensity features, Chang and Allebach [13] had the spectrum logarithmically compressed according to

$$i_{OUT} = \Big(255/\big(log(K+1)\big)\Big) log\Big(K\big(i_{IN}/max(i_{IN})\big) + 1\Big), \tag{3.16}$$

where i_{OUT} is the logarithmically compressed spectrum and i_{IN} is the input spectrum.

Figure 3.3 shows the CSFT of the analog rendering and digital rendering of the regular and irregular halftone textures. The parameter K in Eq. (3.16) is chosen empirically to be 100.

3.3.2 Fourier Spectrum of a Perceived Digital-Rendered Continuous-space Halftone Image with Circular Dot Pattern

In this section, we derive the CSFT of a perceived digital-rendered continuous-space halftone image with circular dot pattern. Let $h_{HVS}(\mathbf{x})$ be the point spread function of the human visual system (HVS). A perceived digital-rendered continuous-space halftone image with circular dot pattern $\widetilde{g_p}(\mathbf{x})$ is defined as

$$\widetilde{g_p}(\mathbf{x}) \;=\; g_p(\mathbf{x}) * h_{\mathrm{HVS}}(\mathbf{x})\,. \tag{3.17}$$

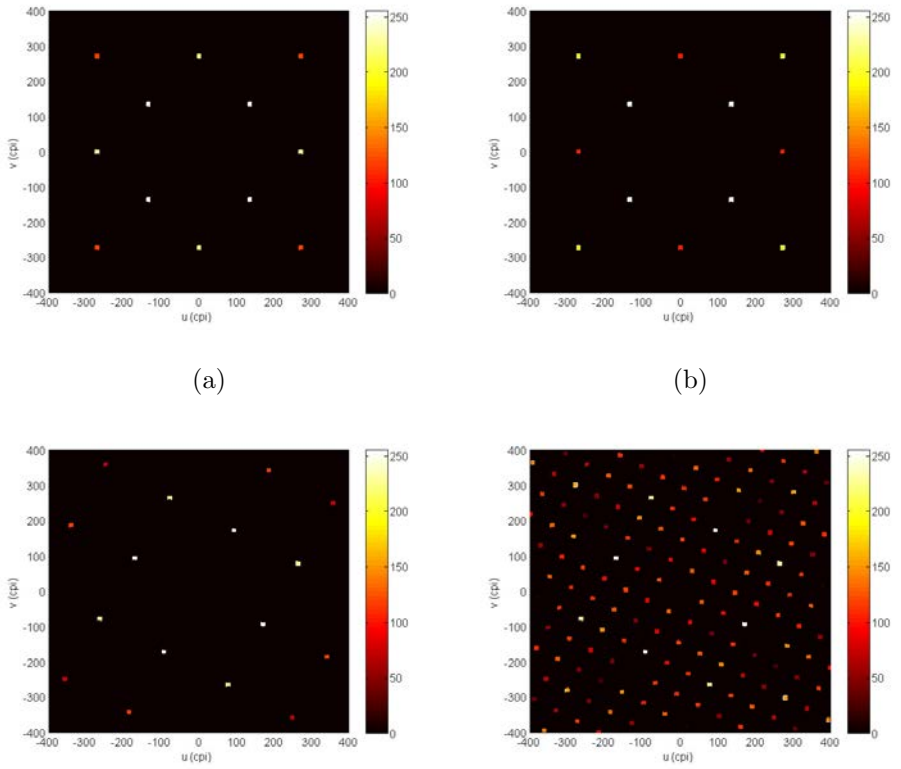

(a) (b)

(c) (d)

Fig. 3.3. Comparison of the difference between the analog rendering and digital rendering between regular and irregular halftone textures in frequency domain. (a) The analog rendering of regular screen in frequency domain. (b) The digital rendering of regular screen in frequency domain. (c) The analog rendering of irregular screen in frequency domain. (d) The digital rendering of irregular screen in frequency domain.

Then, we compute the CSFT of a perceived digital-rendered continuous-space halftone image with circular dot pattern $\widetilde{g_p}(\mathbf{x})$ as follow

$$\begin{aligned}\widetilde{G_p}(\mathbf{u}) &= G_p(\mathbf{u})H_{\mathrm{HVS}}(\mathbf{u}) \\ &= \frac{H_{\mathrm{HVS}}(\mathbf{u})\mathrm{sinc}(R\mathbf{u})}{R^2|\det(\mathbf{M})\det(\mathbf{N})|}\sum_{\mathbf{m}\in Z^2}\mathrm{jinc}\big(\mathbf{M}^{-T}(\mathbf{u}-\mathbf{V}\mathbf{m})\big) \\ &\quad\times\sum_{\mathbf{k}\in Z^2}\delta(\mathbf{u}-\mathbf{V}\mathbf{m}-\frac{1}{R}\mathbf{N}^{-T}\mathbf{k})\,, \end{aligned} \tag{3.18}$$

where the CSFT of the point spread function $h_{HVS}(\mathbf{x})$ is $H_{\mathrm{HVS}}(\mathbf{u})$. In our analysis, the HVS filter we use is N*äsä*nen model [56]. The viewing distance is 16 (in) at 812 dpi.

3.3.3 A Metric for Measuring the Nonuniformity

In the previous section, we have the analytical expression of the spectrum of a perceived digital-rendered continuous-space halftone image. We like to have a metric to measure the nonuniformity of a given halftone pattern. The metric we use to measure the nonuniformity of a give halftone pattern is square root of the average power of the signal.

Let a 2-D periodic signal $f(x,y)$ with period T_{p_x} in x direction and T_{p_y} in y direction can be represented using Fourier series by the following

$$f(x,y) = \sum_{k=-\infty}^{\infty}\sum_{l=-\infty}^{\infty}F_{k,l}e^{j2\pi(kF_{p_x}x+lF_{p_y}y)}\,, \tag{3.19}$$

where the Fourier coefficient $F_{k,l}$ is defined as

$$F_{k,l} = \frac{1}{T_{p_x}}\frac{1}{T_{p_y}}\int_{-T_{p_y}/2}^{T_{p_y}/2}\int_{-T_{p_x}/2}^{T_{p_x}/2}f(x,y)e^{-j2\pi(kF_{p_x}x+lF_{p_y}y)}\,dxdy\,. \tag{3.20}$$

The parameter $F_{p_x} = 1/T_{p_x}$ and $F_{p_y} = 1/T_{p_y}$. The average power of a periodic signal is the sum of the power spectrum density, and the power is defined according to

$$\begin{aligned} P &= \frac{1}{T_{p_x}}\frac{1}{T_{p_y}}\int_{-T_{p_y}/2}^{T_{p_y}/2}\int_{-T_{p_x}/2}^{T_{p_x}/2}|f(x,y)|^2 dxdy \\ &= \frac{1}{T_{p_x}}\frac{1}{T_{p_y}}\int_{-T_{p_y}/2}^{T_{p_y}/2}\int_{-T_{p_x}/2}^{T_{p_x}/2} f(x,y)\sum_{k=-\infty}^{\infty}\sum_{l=-\infty}^{\infty} F_{k,l}^{*} e^{j2\pi(kF_{p_x}x+lF_{p_y}y)} dxdy \\ &= \sum_{k=-\infty}^{\infty}\sum_{l=-\infty}^{\infty} F_{k,l}^{*}\left(\frac{1}{T_{p_x}}\frac{1}{T_{p_y}}\int_{-T_{p_y}/2}^{T_{p_y}/2}\int_{-T_{p_x}/2}^{T_{p_x}/2} f(x,y)e^{j2\pi(kF_{p_x}x+lF_{p_y}y)} dxdy\right) \\ &= \sum_{k=-\infty}^{\infty}\sum_{l=-\infty}^{\infty}|F_{k,l}|^2 . \end{aligned} \tag{3.21}$$

According to Eq. (3.21), we can get the average power of a periodic signal by finding the Fourier coefficients of the 2-D periodic signal. To find the Fourier coefficients of the 2-D periodic signal from the CSFT, we first write the Fourier transform of a 2-D periodic signal as

$$F(u,v) = \sum_{k=-\infty}^{\infty}\sum_{l=-\infty}^{\infty} F_{k,l}\delta(u-\frac{k}{T_{p_x}}, v-\frac{l}{T_{p_y}}) . \tag{3.22}$$

The following is the proof for Eq. (3.22).

$$\begin{aligned} \mathcal{F}^{-1}\{F(u,v)\} &= \int_{-\infty}^{\infty}\int_{-\infty}^{\infty}\left(\sum_{k=-\infty}^{\infty}\sum_{l=-\infty}^{\infty} F_{k,l}\delta(u-\frac{k}{T_{p_x}})\delta(v-\frac{l}{T_{p_y}})\right) e^{j2\pi(ux+vy)}\ dudv \\ &= \sum_{k=-\infty}^{\infty}\sum_{l=-\infty}^{\infty} F_{k,l}\int_{-\infty}^{\infty}\int_{-\infty}^{\infty}\delta(u-\frac{k}{T_{p_x}})\delta(v-\frac{l}{T_{p_y}})e^{j2\pi(ux+vy)}\ dudv \\ &= \sum_{k=-\infty}^{\infty}\sum_{l=-\infty}^{\infty} F_{k,l}e^{j2\pi\frac{k}{T_{p_x}}x}e^{j2\pi\frac{l}{T_{p_y}}y} \\ &= \sum_{k=-\infty}^{\infty}\sum_{l=-\infty}^{\infty} F_{k,l}e^{j2\pi(kF_{p_x}x+lF_{p_y}y)} \\ &= f(x,y) . \end{aligned} \tag{3.23}$$

We know that a perceived digital-rendered continuous-space halftone image with circular dot pattern is a 2-D periodic signal. Therefore, we can find the Fourier coefficient of the perceived digital-rendered continuous-space halftone image according to

Eq. (3.22). The Fourier coefficient $C_{\mathbf{k},\mathbf{m}}$ of the perceived digital-rendered continuous-space halftone image is defined as

$$C_{\mathbf{k},\mathbf{m}} = \frac{H_{\mathrm{HVS}}(\mathbf{V}\mathbf{m}+\frac{1}{R}\mathbf{N}^{-T}\mathbf{k})\mathrm{sinc}(\mathbf{m}+\mathbf{N}^{-T}\mathbf{k})\mathrm{jinc}\big(\frac{1}{R}\mathbf{M}^{-T}\mathbf{N}^{-T}\mathbf{k}\big)}{R^2|\det(\mathbf{M})\det(\mathbf{N})|}\,. \quad (3.24)$$

Now, we have the analytical expression of the the Fourier coefficient $C_{\mathbf{k},\mathbf{m}}$ of a perceived digital-rendered continuous-space halftone image. Average power is a metric of nonuniformity. Then, we categorize the average power of the perceived digital-rendered continuous-space halftone image into three contributions.

The first contribution of the nonuniformity is due to the analog rendering, which is not sampled by the printer lattice. Therefore, the spectrum for the first contribution is

$$\widetilde{G_p}^1(\mathbf{u}) = \frac{H_{\mathrm{HVS}}(\mathbf{u})\mathrm{sinc}(R\mathbf{u})}{R^2|\det(\mathbf{M})\det(\mathbf{N})|}\mathrm{jinc}\big(\mathbf{M}^{-T}(\mathbf{u})\big)\sum_{\mathbf{k}\in Z^2}\delta(\mathbf{u}-\frac{1}{R}\mathbf{N}^{-T}\mathbf{k})\,, \quad (3.25)$$

where $\mathbf{m}$ in Eq. (3.18) is equal to $\mathbf{0}$. The Fourier cofficient $C^1_{\mathbf{k},\mathbf{m}}$ that satisfies the condition of first contribution can be rewritten as

$$C^1_{\mathbf{k},\mathbf{m}} = \frac{H_{\mathrm{HVS}}(\frac{1}{R}\mathbf{N}^{-T}\mathbf{k})\mathrm{sinc}(\mathbf{N}^{-T}\mathbf{k})\mathrm{jinc}\big(\frac{1}{R}\mathbf{M}^{-T}\mathbf{N}^{-T}\mathbf{k}\big)}{R^2|\det(\mathbf{M})\det(\mathbf{N})|}\,. \quad (3.26)$$

The nonuniformity of first contribution is the square root of the sum of the Fourier coefficient $C^1_{\mathbf{k},\mathbf{m}}$ over $\mathbf{k}$, and $\mathbf{m}=\mathbf{0}$ and $\frac{1}{R}\mathbf{N}^{-T}\mathbf{k}\neq\mathbf{0}$, and we have

$$P^1_{nonuniformity} = \sqrt{\sum_{\substack{\mathbf{k}\in Z^2\\ \mathbf{k}\neq[0\ 0]^{\mathrm{T}}}}|C^1_{\mathbf{k},\mathbf{m}}|^2}\,. \quad (3.27)$$

The second contribution of the nonuniformity is introduced by the digital rendering, which is obtained by sampling the analog rendering, and then convolved with the printer model. As we know, if we sample the image in spatial domain, we get replication in frequency domain. The replicated frequency components may or may not fall on the same frequency locations as the analog rendering. In the second contribution of the nonuniformity, we find those frequency components that fall on the on

the same frequency locations as the analog rendering. The following is the condition to find the frequency components for the second contribution of the nonuniformity:

$$\begin{gathered}\text{For any } \mathbf{m} \in Z^2 \text{ and } \mathbf{m} \neq \mathbf{0},\ \exists\, \mathbf{k} \in Z^2 \text{ and } \mathbf{l} \in Z^2 \Rightarrow \\ \mathbf{V}\mathbf{m} + \frac{1}{R}\mathbf{N}^{-T}\mathbf{k} = \frac{1}{R}\mathbf{N}^{-T}\mathbf{l} \text{ and } \mathbf{V}\mathbf{m} + \frac{1}{R}\mathbf{N}^{-T}\mathbf{k} = \frac{1}{R}\mathbf{N}^{-T}\mathbf{l} \neq \mathbf{0}\,. \end{gathered} \tag{3.28}$$

Therefore, the spectrum for the second contribution is the Eq. (3.29), and the spectrum is satisfied the condition (3.28).

$$\begin{aligned}\widetilde{G_p}^2(\mathbf{u}) &= G_p(\mathbf{u})H_{\mathrm{HVS}}(\mathbf{u}) \\ &= \frac{H_{\mathrm{HVS}}(\mathbf{u})\mathrm{sinc}(R\mathbf{u})}{R^2|\det(\mathbf{M})\det(\mathbf{N})|}\sum_{\mathbf{m}\in Z^2}\mathrm{jinc}\big(\mathbf{M}^{-T}(\mathbf{u}-\mathbf{V}\mathbf{m})\big) \\ &\quad \times \sum_{\mathbf{k}\in Z^2}\delta(\mathbf{u}-\mathbf{V}\mathbf{m}-\frac{1}{R}\mathbf{N}^{-T}\mathbf{k})\,, \end{aligned} \tag{3.29}$$

The Fourier coefficient $C^2_{\mathbf{k},\mathbf{m}}$ that satisfies the condition of second contribution is

$$C^2_{\mathbf{k},\mathbf{m}} = \frac{H_{\mathrm{HVS}}(\mathbf{V}\mathbf{m}+\frac{1}{R}\mathbf{N}^{-T}\mathbf{k})\mathrm{sinc}(\mathbf{m}+\mathbf{N}^{-T}\mathbf{k})\mathrm{jinc}\big(\frac{1}{R}\mathbf{M}^{-T}\mathbf{N}^{-T}\mathbf{k}\big)}{R^2|\det(\mathbf{M})\det(\mathbf{N})|}\,, \tag{3.30}$$

where the parameter $\mathbf{k}$ and $\mathbf{m}$ should satisfy condition (3.28). The nonuniformity of second contribution is the square root of the sum of the Fourier coefficient $C^2_{\mathbf{k},\mathbf{m}}$, and we have

$$P^2_{nonuniformity} = \sqrt{\sum_{\mathbf{k}\in Z^2}\sum_{\substack{\mathbf{m}\in Z^2 \\ \mathbf{m}\neq[0\ 0]^{\mathrm{T}}}}|C^2_{\mathbf{k},\mathbf{m}}|^2}\,. \tag{3.31}$$

The third contribution of the nonuniformity is also introduced by the digital rendering. However, The replicated frequency components fall on the different frequency locations as the analog rendering. The following is the condition to find the frequency components for the third contribution of the nonuniformity:

$$\begin{gathered}\text{For any } \mathbf{m} \in Z^2 \text{ and } \mathbf{m} \neq \mathbf{0},\ \nexists\, \mathbf{k} \in Z^2 \text{ and } \mathbf{l} \in Z^2 \Rightarrow \\ \mathbf{V}\mathbf{m} + \frac{1}{R}\mathbf{N}^{-T}\mathbf{k} = \frac{1}{R}\mathbf{N}^{-T}\mathbf{l}\,. \end{gathered} \tag{3.32}$$

Therefore, the spectrum for the third contribution is the Eq. (3.33), and the spectrum is satisfied the condition (3.32).

$$\begin{aligned}\widetilde{G_p}^3(\mathbf{u}) &= G_p(\mathbf{u})H_{\mathrm{HVS}}(\mathbf{u}) \\ &= \frac{H_{\mathrm{HVS}}(\mathbf{u})\mathrm{sinc}(R\mathbf{u})}{R^2|\det(\mathbf{M})\det(\mathbf{N})|}\sum_{\mathbf{m}\in Z^2}\mathrm{jinc}\big(\mathbf{M}^{-T}(\mathbf{u}-\mathbf{V}\mathbf{m})\big) \\ &\quad\times\sum_{\mathbf{k}\in Z^2}\delta(\mathbf{u}-\mathbf{V}\mathbf{m}-\frac{1}{R}\mathbf{N}^{-T}\mathbf{k})\,, \end{aligned} \tag{3.33}$$

The Fourier coefficient $C^3_{\mathbf{k},\mathbf{m}}$ that satisfies the condition (3.32) is

$$C^3_{\mathbf{k},\mathbf{m}} = \frac{H_{\mathrm{HVS}}(\mathbf{V}\mathbf{m}+\frac{1}{R}\mathbf{N}^{-T}\mathbf{k})\mathrm{sinc}(\mathbf{m}+\mathbf{N}^{-T}\mathbf{k})\mathrm{jinc}\big(\frac{1}{R}\mathbf{M}^{-T}\mathbf{N}^{-T}\mathbf{k}\big)}{R^2|\det(\mathbf{M})\det(\mathbf{N})|}\,, \tag{3.34}$$

where the parameter $\mathbf{k}$ and $\mathbf{m}$ should satisfy Eq. (3.32). The nonuniformity of third contribution is the square root of the sum of the Fourier coefficient $C^3_{\mathbf{k},\mathbf{m}}$, and we have

$$P^3_{nonuniformity} = \sqrt{\sum_{\mathbf{k}\in Z^2}\sum_{\mathbf{m}\in Z^2}|C^3_{\mathbf{k},\mathbf{m}}|^2}\,. \tag{3.35}$$

Figure 3.4 shows the spectrums of three contributions of the nonuniformity for regular and irregular halftone textures. Figure 3.4 (a) and (b) is the first contribution of the nonuniformity of regular and irregular halftone textures. Then, Fig. 3.4 (c) and (d) show the the second contribution of the nonuniformity of regular and irregular halftone textures. According to the definition of second contribution of nonuniformity, frequency components fall on the same frequency locations as the the first contribution of the nonuniformity for both regular and irregular halftone textures. In Fig. 3.4 (f), it shows that there are new frequency components in the spectrum of the third contribution of the nonuniformity of irregular halftone textures. On the other hand, there is no new frequency components in the spectrum of the third contribution of the nonuniformity of regular halftone textures as shown in Fig. 3.4 (e).

As we know the spectra of three contributions of the nonuniformity, we can use Eq. (3.27), (3.31) and (3.35) to compute the nonuniformity in terms of root mean square that are introduced by first, second and third contribution of regular and irregular halftone textures. The results are shown in Table 3.1. From table 3.1, we can see

Table 3.1
The RMS value of three contributions for regular and irregular halftone textures

	First contribution	Second contribution	Third contribution
Regular	9.66×10^{-6}	2.41×10^{-6}	0
Irregular	8.16×10^{-6}	3.85×10^{-7}	9.97×10^{-4}

Table 3.2
Power budget of the RMS values for measuring the nonuniformity that applies the HVS filter

	First contribution	Second contribution	Third contribution
Regular	80.1%	19.9%	0%
Irregular	0.812%	0.038%	99.15%

that the nonuniformity of regular halftone textures comes from the first and second contribution. The variations come from those frequency components which are far from the spectrum origin as shown in Fig. 3.4 (a) and (c). As we see the spatial image from a distance, these frequency components may be invisible to the human viewer. On the other hand, the nonuniformity of irregular halftone textures mostly comes from the third contribution. The new frequency components are introduced because of the non-integer elements in their periodicity matrix and finite addressability of the marking engine. These new frequency components are low enough to be visible to the human viewer. In Table 3.2, THE table summarizes the power budgets that include the HVS filter when we calculate the RMS value. In our experiments, the HVS filter we use is N*äsä*nen model [56]. The viewing distance is 16 (in) at 812 dpi.

3.3.4 Visualization of Contributions of the Nonuniformity

In the previous section, we show the spectra of the three contributions of the nonuniformity and provide a metric to measure the nonuniformity. In this section,

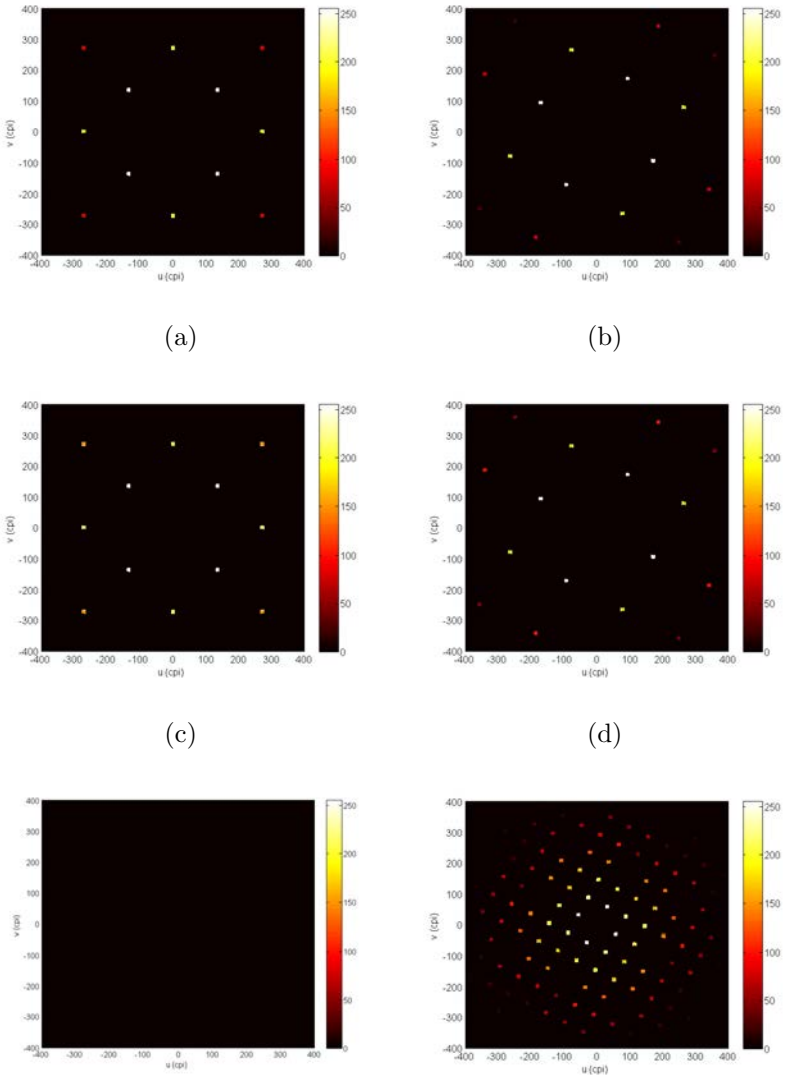

(a) (b)

(c) (d)

(e) (f)

Fig. 3.4. Comparison of the spectra of three contributions of the nonuniformity of regular and irregular halftone textures. The parameter K in Eq. (3.16) is chosen empirically to be 10^8. (a) First contribution of the nonuniformity of regular halftone textures. (b) First contribution of the nonuniformity of irregular halftone textures. (c) Second contribution of the nonuniformity of regular halftone textures. (d) Second contribution of the nonuniformity of irregular halftone textures. (e) Third contribution of the nonuniformity of regular halftone textures. (f) Third contribution of the nonuniformity of irregular halftone textures.

we visualize these three contributions of nonuniformity in spatial domain. We use two sets of regular and irregular screen pairs in the following experiments. For the first example, the tile vectors of regular screen are: $\mathbf{n_1} = [3; 3]$ and $\mathbf{n_2} = [-3; 3]$. The screen angle and frequency of the regular screen are 45° and 191.4 line-per-inch (lpi), respectively. The basic screen block (BSB) [28] of this regular screen 6×6. On the other hand, the tile vectors of the irregular screen are $\mathbf{n_1} = [2; 11/3]$ and $\mathbf{n_2} = [-11/3; 2]$. The screen angle and frequency of the irregular screen are 61° and 194.4 lpi, respectively. The BSB of this irregular screen 157×157. For the second example, the tile vectors of regular screen are: $\mathbf{n_1} = [4; 4]$ and $\mathbf{n_2} = [-4; 4]$. The screen angle and frequency of the regular screen are 45° and 143.5 (lpi), respectively. The BSB of this irregular screen 8×8. On the other hand, the tile vectors of the irregular screen are $\mathbf{n_1} = [4; 11/3]$ and $\mathbf{n_2} = [-11/3; 4]$. The screen angle and frequency of the irregular screen are 42.5° and 149.63 (lpi), respectively. The BSB of this irregular screen 265×265. Two examples of regular and irregular screen are considered to understand how the screen frequency affect the nonuniformity. The image size of the halftone textures is chosen to be a integer multiple of the BSB to prevent the windowing artifact, which is introduced in computing the Discrete Fourier Transform (DFT) of a 2-D image. The parameter K in Eq. (3.16) is chosen empirically to be 50 for Fig. 3.5, Fig. 3.6, Fig. 3.7, Fig. 3.8, Fig. 3.9, Fig. 3.10, Fig. 3.11, and Fig. 3.12.

In the experiment, we first create the analog rendering of a given halftone screen in spatial domain. Then, we sample the analog rendering, and digital rendering is obtained by convolving the sampled analog rendering with a printer dot profile function. Then, we compute the DFT of the analog and the digital rendering. We create the analog rendering in spatial domain by upsampling 24 times to mimic the circle function at an infinity resolution. On the other hand, we also upsample 24 times for the digital rendering by using nearest neighbor method.

As we know from the previous section, the first contribution of the nonuniformity is contributed by the analog rendering, and we compute Inverse Discrete Fourier Transform (IDFT) to get the spatial domain of the first contribution of the nonuniformity.

To get the spatial domain of second and third contribution of the nonuniformity, we first calculate the spectrum difference between the analog and digital rendering. According to the definition of the second contribution of the nonuniformity, the frequency components of the second contribution fall on the same frequency location as the first contribution. Thus, we find those frequency components that are same as the first contribution in the difference spectrum of the analog and digital rendering, and that forms the spectrum of the second contribution of the nonuniformity. Similarly, we can get the second contribution of the nonuniformity in the spatial domain by computing the IDFT. Finally, the spectrum of the third contribution of the nonuniformity is formed by finding those frequency components that do not fall on the same location as the first contribution of the nonuniformity. Afterward, IDFT is performed to get the third contribution of the nonuniformity in the spatial domain. Spatial domain images in Fig. 3.6, Fig. 3.8, Fig. 3.10 and Fig. 3.12 that are all multiplied by a constant to make the maximum value of each image to be absorptance 1 (black).

The results of the first example of regular halftone textures are shown in Fig. 3.5 and Fig. 3.6. Figure 3.5 (a) and (b) are the analog and digital rendering in the spatial domain. Figure 3.5 (c) and (d) are the corresponding DFT spectrum. Then, we analyze the DFT spectrum of the digital rendering, and it is categorized into two different contributions of nonuniformity. Images of first and second contribution of the nonuniformity in the spatial domain are shown Fig. 3.6 (a) and (b). Figure. 3.6 (c) and (d) are the corresponding DFT spectra. As we know from the analysis in the previous section, The nonuniformity of a given regular halftone texture is given by the first and second contribution. The image of the first contribution shown in Fig. 3.6 (a) is contributed by the analog rendering shown in Fig. 3.5 (a). On the other hand, the image of the second contribution shown in Fig. 3.6 (b) comes from the difference of the analog and digital rendering.

Next, we have results of the first example of irregular halftone textures are shown in Fig. 3.7 and Fig. 3.8. In the DFT spectra of analog rendering of the regular and irregular halftone textures, we can not see any difference except the screen frequency

and screen angle. However, the DFT spectra of digital rendering of the regular and irregular halftone textures are quite different due to the new frequency components introduced by sampling the analog rendering. Then, we analyze the DFT spectrum of the digital rendering, and we categorize it into three different contributions of the nonuniformity. Images of first, second, and third contribution of the nonuniformity in the spatial domain are shown in Fig. 3.8 (a), (b) and (c). The corresponding DFT spectra are shown in Fig. 3.8 (d), (e) and (f). In contrast to the regular case, there are new frequency components are shown in the spectrum, and new components form the third contribution of the nonuniformity. In Fig. 3.8 (f), there are roughly 60 cpi frequency components that can be observed, and we can see a 1/60 in approximately repeated pattern in Fig. 3.8 (c).

In the second example, we choose a lower screen frequency for regular and irregular screen. The results of the second example of regular halftone textures are shown in Fig. 3.9 and Fig. 3.10. In addition, the results of the first example of irregular halftone textures are shown in Fig. 3.11 and Fig. 3.12. The contributions of nonuniformity in the spatial or in the frequency domain show a similar pattern as in the first example. However, we can see in Fig. 3.12 that there are roughly 30 cpi frequency components that can be observed. Thus, the irregular halftone textures in the second example gives a more visible repeated pattern in the spatial domain than in the first example. We conclude that a given irregular halftone textures becomes noisier when the screen frequency is lower.

To visualize graininess from a given digital rendering that we have used in this section, we first apply the HVS filter to the digital halftone image, and the perceived image is processed based on the module shown in Fig. 3.13 to visualize graininess. The HVS filter we use is N*äsä*nen model [56]. The view distance is 16 (in) at 812 dpi. In Fig. 3.13, the perceived image $\widetilde{g_p}(x, y)$ is obtained by convolving the digital rendering $g_p(x, y)$ with the point spread function $h_{HVS}(x, y)$. According to the Fig. 3.13, we have

the relationship between the enhanced perceived image $\widetilde{g_p}'(x,y)$ and the perceived image $\widetilde{g_p}(x,y)$ as follows

$$\begin{aligned}\widetilde{g_p}'(x,y) &= S \times \left(\widetilde{g_p}(x,y) - E[\widetilde{g_p}(x,y)]\right) + E[\widetilde{g_p}(x,y)] \\ &= S \times \Delta\widetilde{g_p}(x,y) + E[\widetilde{g_p}(x,y)]\,, \end{aligned} \tag{3.36}$$

where the parameter S is chosen empirically be 5 to get a better comparison visually.

The digital rendering of two different pairs of regular and irregular halftone textures are considered. The results are shown in Fig. 3.14 and Fig. 3.15. Figure 3.14 are the digital rendering, perceived digital rendering and enhanced perceived digital rendering of the first example of the regular and irregular halftone textures. Figure 3.15 are the digital rendering, perceived digital rendering and enhanced perceived digital rendering of the second example of the regular and irregular halftone textures. In Fig. 3.14 (c) and (f), we can see graininess of both images. However, graininess of both images does not have a big difference visually. To quantify graininess, we calculate the variance of the perceived digital rendering for regular and irregular screen in Fig. 3.14 (b) and (e). The variance of both images are equal to 0.0019. This could be due to the fact that the screen frequency of the first pair of of regular and irregular halftone textures is high enough so that the variance of both images are the same when the digital rendering is applied with the HVS filter.

Next, we consider the second pair of of regular and irregular halftone textures that has lower screen frequency than the first pair. In Fig. 3.15 (c) and (f), we can see that the enhanced perceived digital rendering of irregular halftone textures has high graininess than the enhanced perceived digital rendering of regular halftone textures. Similarly, we calculate the variance of the perceived digital rendering for regular and irregular halftone textures in Fig. 3.15 (b) and (e). The variance of the perceived digital rendering for regular halftone textures is 0.0017. On the other hand, the variance of the perceived digital rendering for irregular screen is 0.0034. Based on these two examples, we find out that the screen frequency affects graininess of a

given digital rendering. The lower the screen frequency is, the more visible graininess is observed.

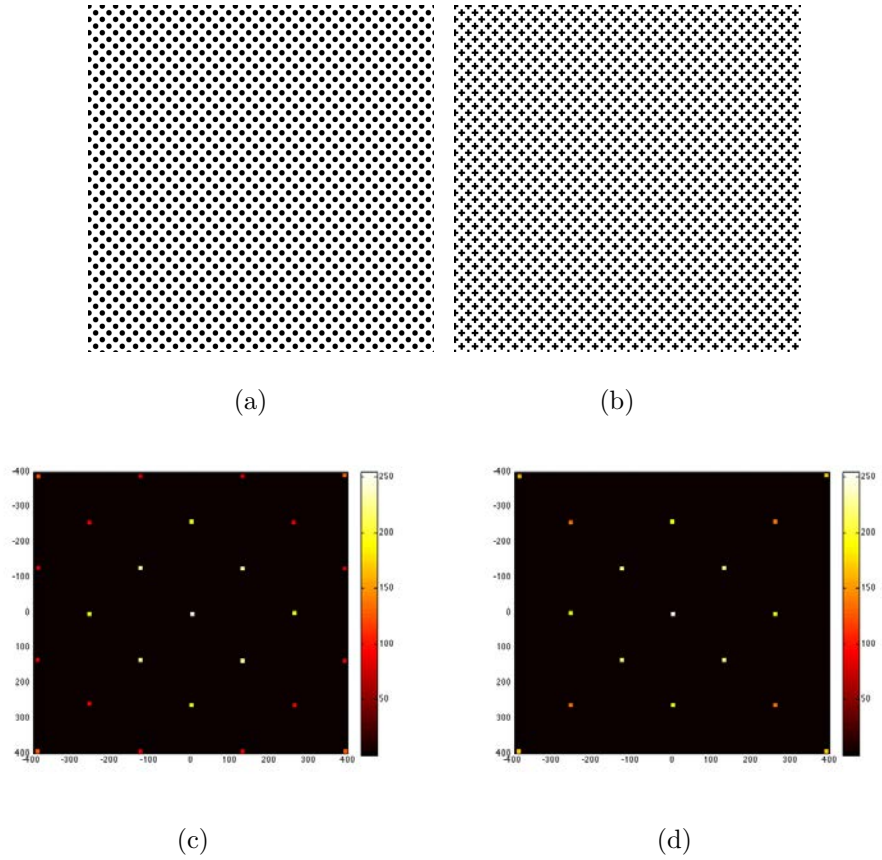

(a) (b)

(c) (d)

Fig. 3.5. The tile vectors of regular screen are: $\mathbf{n_1} = [3; 3]$ and $\mathbf{n_2} = [-3; 3]$. The screen angle and frequency of the regular screen are 45° and 191.4 (lpi), respectively. The parameter K in Eq. (3.16) is chosen empirically to be 50. (a) The analog rendering of regular hafltone textures. (b) The digital rendering of regular halftone textures. (c) The DFT spectrum of the analog rendering of regular halftone textures. (d) The DFT spectrum of the digital rendering of regular halftone textures.

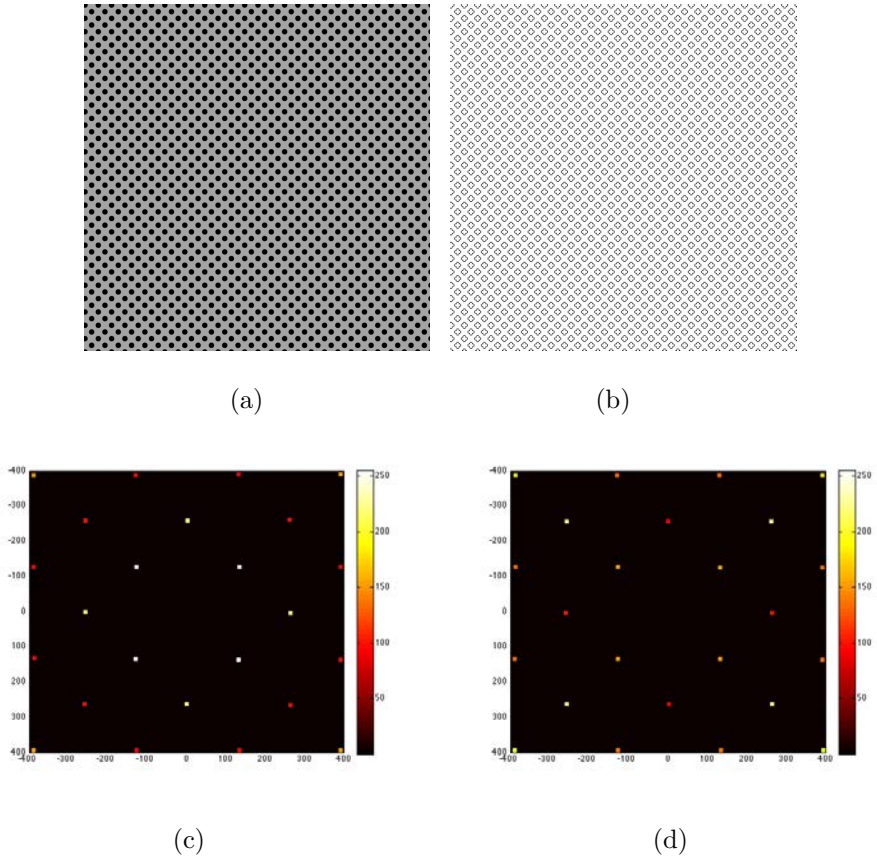

Fig. 3.6. Comparison of the DFT spectra of contributions of the nonuniformity of regular halftone textures. The parameter K in Eq. (3.16) is chosen empirically to be 50. The spatial domain images are obtained by calculating the IDFT of the DFT spectra. These images are all multiplied by a constant to make the maximum value of each image to be absorptance 1 (black). (a) The spatial image of the first contribution of the nonuniformity of regular halftone textures. (b) The spatial image of second contribution of the nonuniformity of regular halftone textures. (c) The DFT spectrum of the first contribution of the nonuniformity of regular halftone textures. (d) The DFT spectrum of second contribution of the nonuniformity of regular halftone textures.

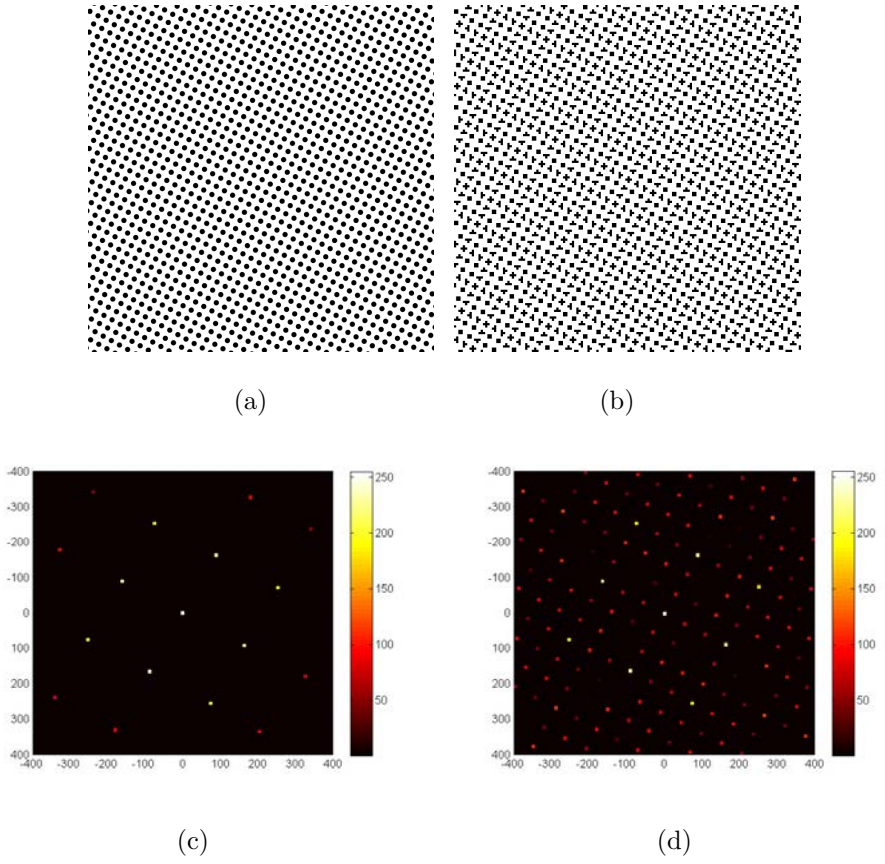

Fig. 3.7. The tile vectors of the irregular screen are $\mathbf{n_1} = [2; 11/3]$ and $\mathbf{n_2} = [-11/3; 2]$. The screen angle and frequency of the irregular screen are 61° and 194.4 (lpi), respectively. The parameter K in Eq. (3.16) is chosen empirically to be 50. (a) The analog rendering of irregular halftone textures. (b) The digital rendering of irregular halftone textures. (c) The DFT spectrum of the analog rendering of irregular halftone textures. (d) The DFT spectrum of the digital rendering of irregular halftone textures.

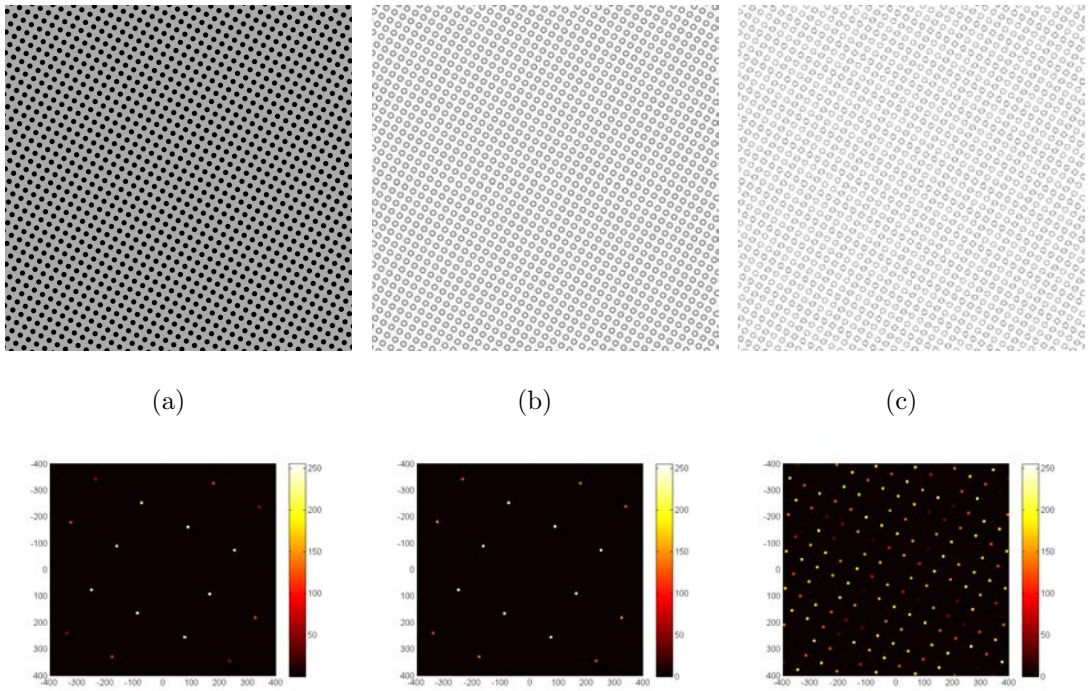

(a) (b) (c)

(d) (e) (f)

Fig. 3.8. Comparison of the DFT spectra of contributions of the nonuniformity of irregular halftone textures. The parameter K in Eq. (3.16) is chosen empirically to be 50. The spatial domain images are obtained by calculating the IDFT of the DFT spectra. These images are all multiplied by a constant to make the maximum value of each image to be absorptance 1 (black). (a) The spatial image of the first contribution of the nonuniformity of irregular halftone textures. (b) The spatial image of second contribution of the nonuniformity of irregular halftone textures. (c) The spatial image of third contribution of the nonuniformity of irregular halftone textures. (d) The DFT spectrum of the first contribution of the nonuniformity of irregular halftone textures. (e) The DFT spectrum of second contribution of the nonuniformity of irregular halftone textures. (f) The DFT spectrum of third contribution of the nonuniformity of irregular halftone textures.

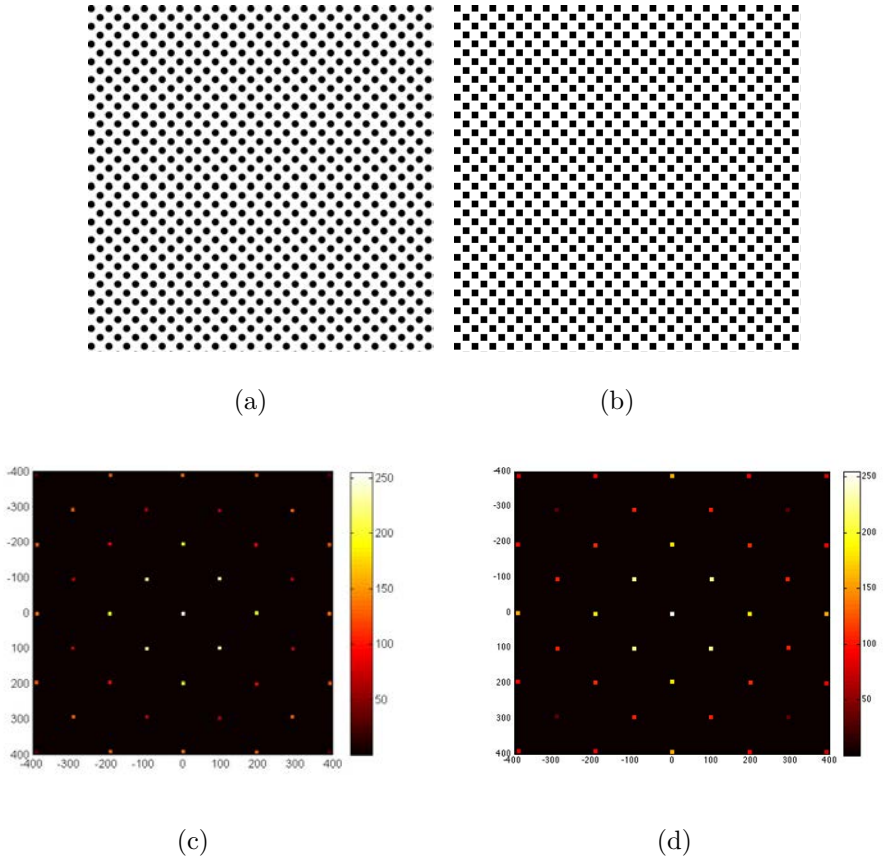

Fig. 3.9. The tile vectors of regular screen are: $\mathbf{n_1} = [4; 4]$ and $\mathbf{n_2} = [-4; 4]$. The screen angle and frequency of the regular screen are 45 ° and 143.5 (lpi), respectively. The parameter K in Eq. (3.16) is chosen empirically to be 50. (a) The analog rendering of regular halftone textures. (b) The digital rendering of regular halftone textures. (c) The DFT spectrum of the analog rendering of regular halftone textures. (d) The DFT spectrum of the digital rendering of regular halftone textures.

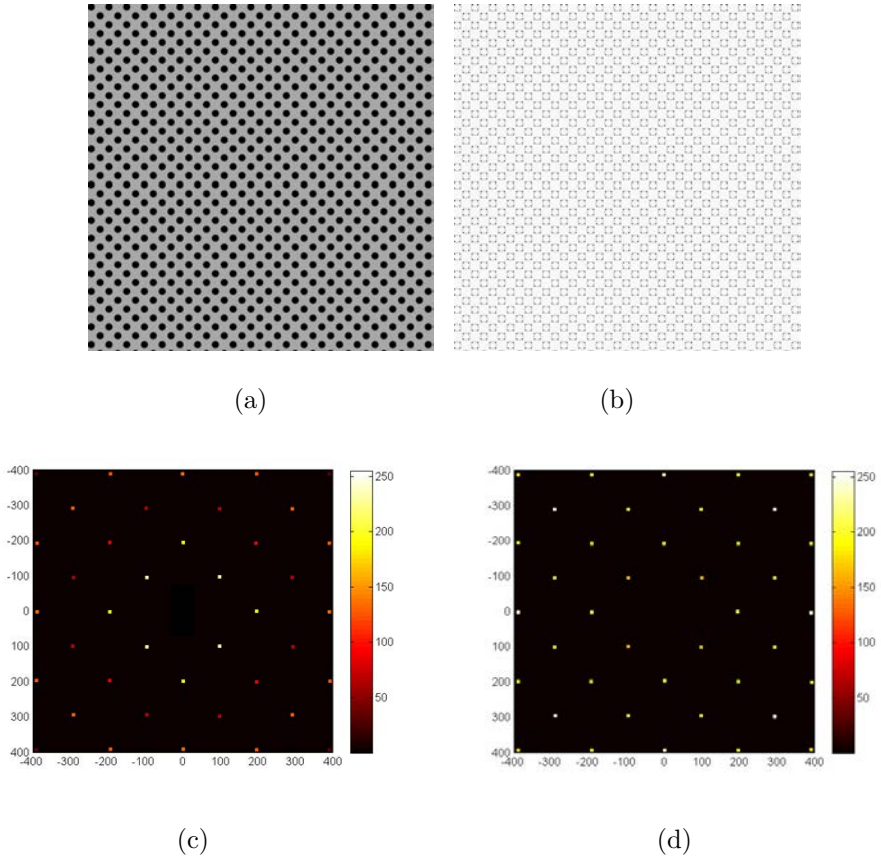

Fig. 3.10. Comparison of the DFT spectra of contributions of the nonuniformity of regular halftone textures. The parameter K in Eq. (3.16) is chosen empirically to be 50. The spatial domain images are obtained by calculating the IDFT of the DFT spectra. These images are all multiplied by a constant to make the maximum value of each image to be absorptance 1 (black). (a) The spatial image of the first contribution of the nonuniformity of regular halftone textures. (b) The spatial image of second contribution of the nonuniformity of regular halftone textures. (c) The DFT spectrum of the first contribution of the nonuniformity of regular halftone textures. (d) The DFT spectrum of second contribution of the nonuniformity of regular halftone textures.

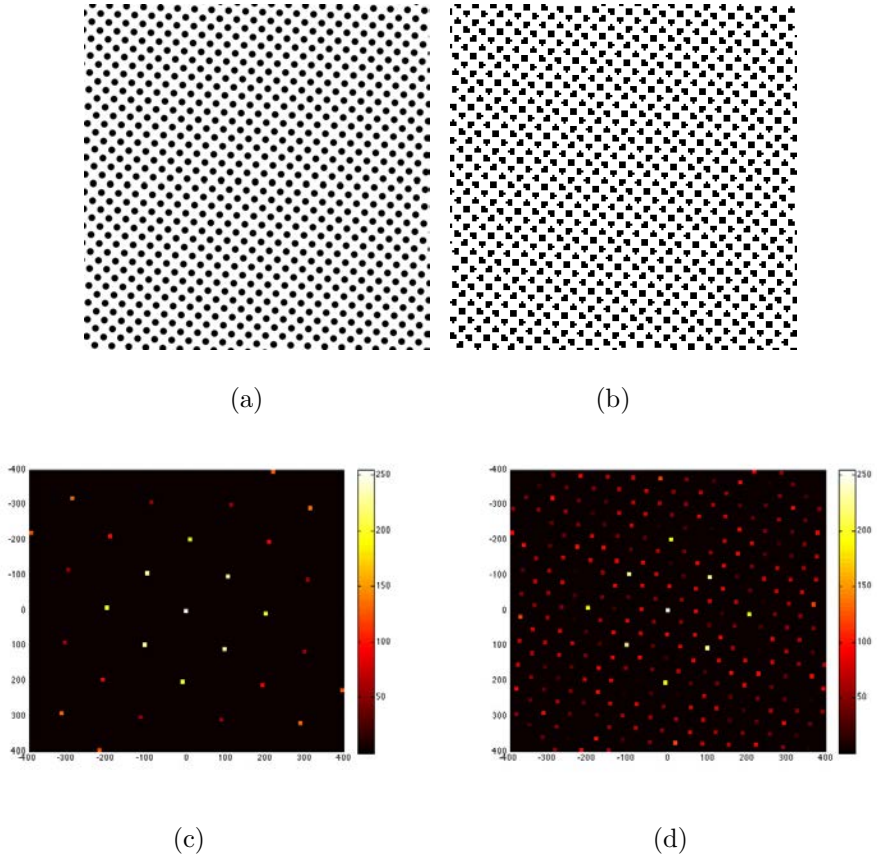

Fig. 3.11. The tile vectors of the irregular screen are $\mathbf{n_1} = [4; 11/3]$ and $\mathbf{n_2} = [-11/3; 4]$. The screen angle and frequency of the irregular screen are $42.5\,^\circ$ and 149.63 (lpi), respectively. The parameter K in Eq. (3.16) is chosen empirically to be 50. (a) The analog rendering of irregular halftone textures. (b) The digital rendering of irregular halftone textures. (c) The DFT spectrum of the analog rendering of irregular halftone textures. (d) The DFT spectrum of the digital rendering of irregular halftone textures.

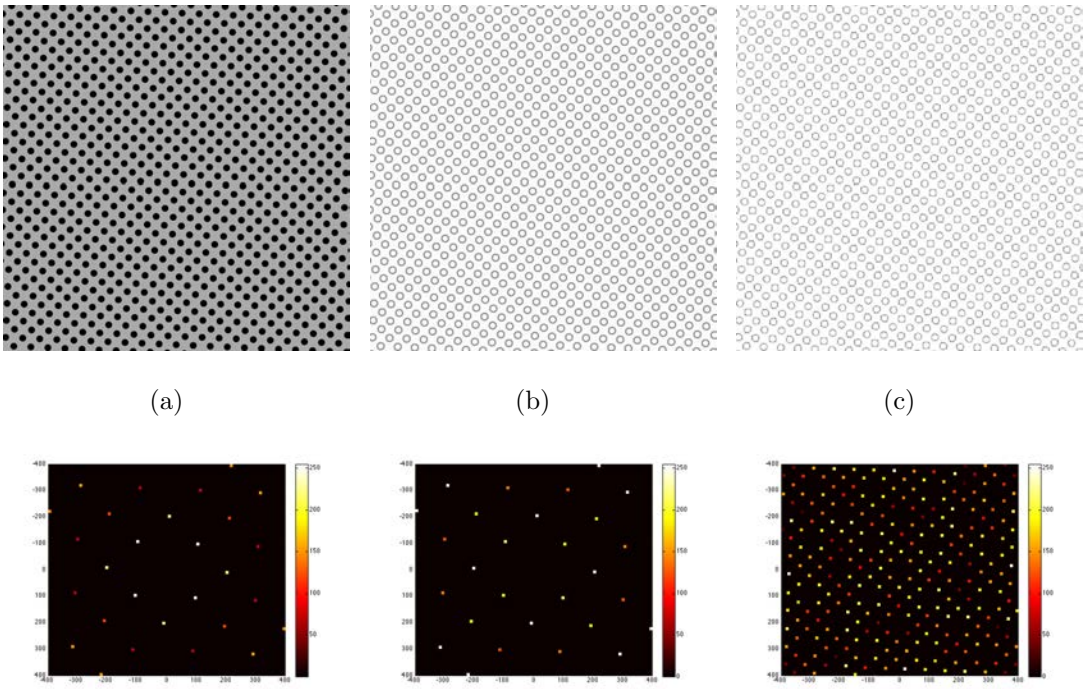

(a) (b) (c)

(d) (e) (f)

Fig. 3.12. Comparison of the DFT spectra of contributions of the nonuniformity of irregular halftone textures. The parameter K in Eq. (3.16) is chosen empirically to be 50. The spatial domain images are obtained by calculating the IDFT of the DFT spectra. These images are all multiplied by a constant to make the maximum value of each image to be absorptance 1 (black). (a) The spatial image of the first contribution of the nonuniformity of irregular halftone textures. (b) The spatial image of second contribution of the nonuniformity of irregular halftone textures. (c) The spatial image of third contribution of the nonuniformity of irregular halftone textures. (d) The DFT spectrum of the first contribution of the nonuniformity of irregular halftone textures. (e) The DFT spectrum of second contribution of the nonuniformity of irregular halftone textures. (f) The DFT spectrum of third contribution of the nonuniformity of irregular halftone textures.

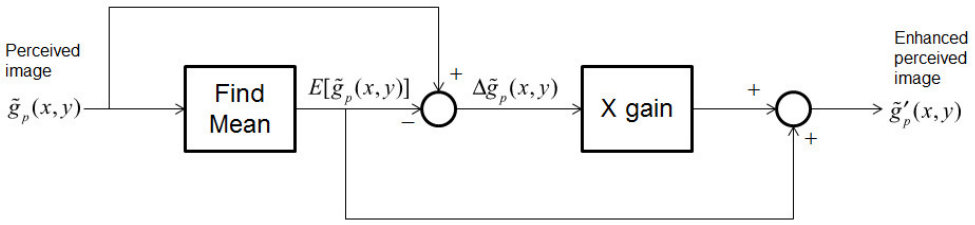

Fig. 3.13. A tool to visualize graininess of a given digital halftone image.

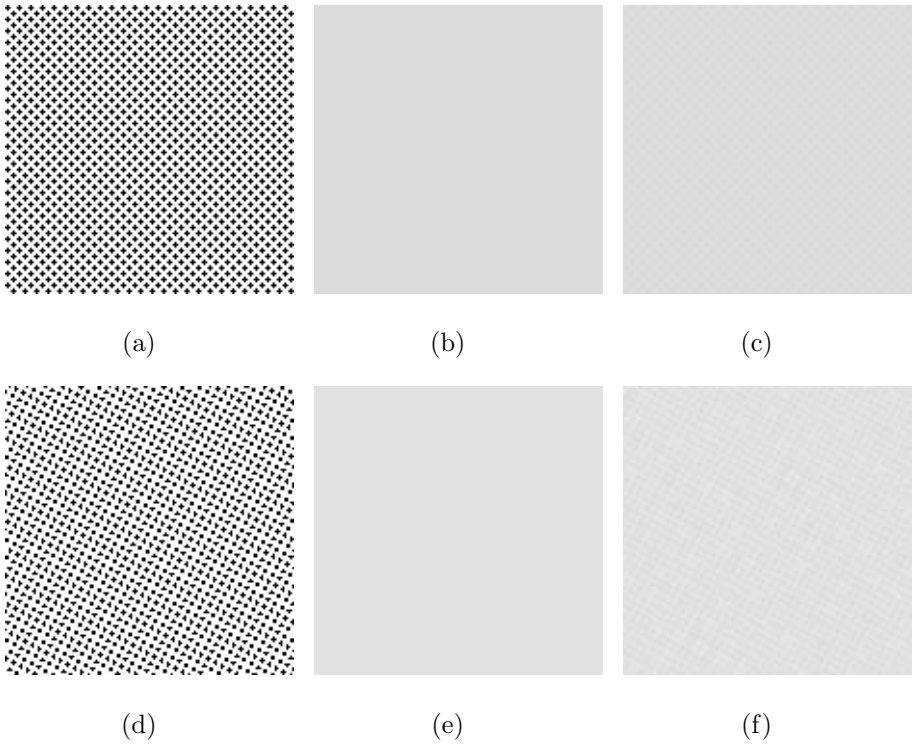

Fig. 3.14. This example shows that a higher screen frequency of the regular and irregular halftone textures. From the enhanced perceived image of the regular and irregular halftone textures, graininess of both images does not have a big difference visually. (a) Digital rendering of the regular halftone textures. (b) The perceived image of the regular halftone textures is obtained by convolving the digital rendering with the HVS filter. The variance of this image is equal to 0.0019. (c) The enhanced perceived image of the regular halftone textures is obtained according to Eq. (3.36) and Fig. 3.13. (d) Digital rendering of the irregular halftone textures. (e) The perceived image of the irregular halftone textures is obtained by convolving the digital rendering with the HVS filter. The variance of this image is equal to 0.0019 (f) The enhanced perceived image of the irregular halftone textures is obtained according to Eq. (3.36) and Fig. 3.13.

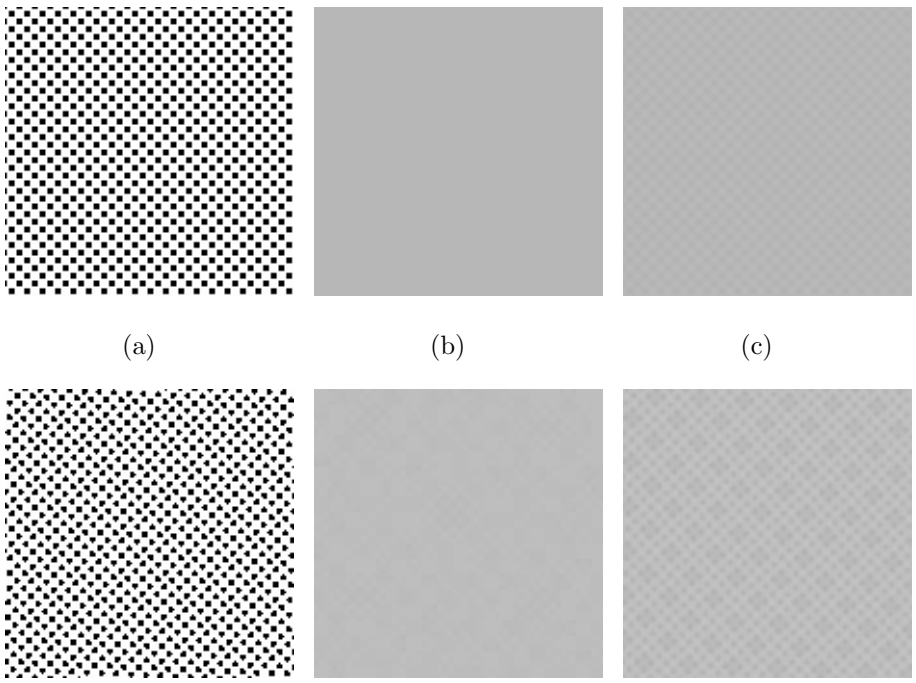

Fig. 3.15. Another example shows that a lower screen frequency of the regular and irregular halftone textures. From the enhanced perceived image of the regular and irregular halftone textures, graininess of irregular halftone textures are more visible than graininess of regular halftone textures. (a) Digital rendering of the regular halftone textures. (b) The perceived image of the regular halftone textures is obtained by convolving the digital rendering with the HVS filter. The variance of this image is equal to 0.0017 (c) The enhanced perceived image of the regular halftone textures is obtained according to Eq. (3.36) and Fig. 3.13. (d) Digital rendering of the irregular halftone textures. (e) The perceived image of the irregular halftone textures is obtained by convolving the digital rendering with the HVS filter. The variance of this image is equal to 0.0034 (f) The enhanced perceived image of the irregular halftone textures is obtained according to Eq. (3.36) and Fig. 3.13.

3.4 Spatial-statistics-based Analysis of Regular and Irregular Periodic, Clustered-dot Halftone Textures

In this section, we report on a study of a spatial-statistics-based analysis of regular and irregular periodic, clustered-dot halftone textures. In the spatial-statistics-based analysis, three different spatial statistics are considered. First, we find the disparity between the centroids of dot clusters in the captured printed and digital halftone textures, and lattice points generated by the periodicity matrix of regular or irregular halftone screens. Second, we find the area of each dot cluster in the captured printed and digital halftone textures. Finally, the compactness of each dot cluster in the captured printed and digital halftone textures is discussed.

In this section, we find the error between the centroids of dot clusters in the halftone textures, and lattice points generated by the periodicity matrix of regular or irregular halftone screens. We use a set of regular and irregular screen pairs in our experiment. For the first example, the tile vectors of regular screen are: $\mathbf{n_1} = [3; 3]$ and $\mathbf{n_2} = [-3; 3]$. The screen angle and frequency of the regular screen are 45° and 191.4 line-per-inch (lpi), respectively. The basic screen block (BSB) [28] of this regular screen 6×6. On the other hand, the tile vectors of the irregular screen are $\mathbf{n_1} = [2; 11/3]$ and $\mathbf{n_2} = [-11/3; 2]$. The screen angle and frequency of the irregular screen are 61° and 194.4 lpi, respectively. The BSB of this irregular screen 157×157.

3.4.1 Disparity between the Centroids of Dot Clusters and Lattice Points

These digital halftone textures are shown in Fig. 3.16. We also print these digital halftone textures by HP Indigo 5000 at 812.8 dpi, and capture these textures by QEA PIAS II at 7663 dpi. The image size is 768×1024. The captured printed halftone textures are shown in Fig. 3.17.

To find the error between centroids and lattice points, we first find the centroid of each dot cluster. For digital halftone textures, we can directly find centroids in Fig. 3.16 (a) and (b). For captured printed halftone textures, Otsu algorithm [60] is

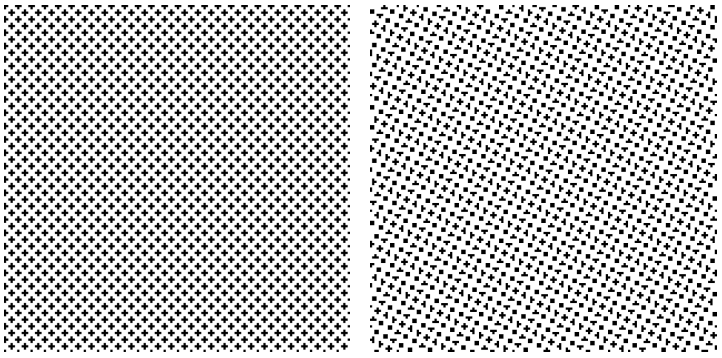

(a) (b)

Fig. 3.16. Regular and irregular halftone textures used to find error between centroids of dot clusters in the digital halftone textures, and lattice points generated by the periodicity matrix of regular or irregular halftone screens. (a) The first example of regular halftone textures with tile vectors $\mathbf{n_1} = [3; 3]$ and $\mathbf{n_2} = [-3; 3]$. (b) The first example of irregular halftone textures with tile vectors $\mathbf{n_1} = [2; 11/3]$ and $\mathbf{n_2} = [-11/3; 2]$.

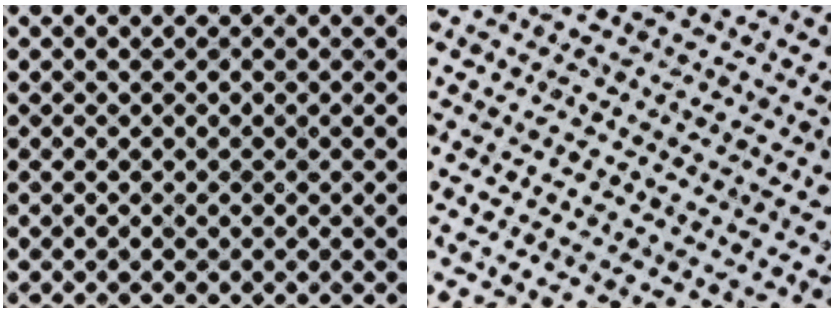

(a) (b)

Fig. 3.17. Captured printed regular and irregular halftone textures. The digital halftone textures are printed by HP Indigo 5000 at 812.8 dpi, and then captured by QEA PIAS II at 7663 dpi. The image size is 768×1024. (a) The captured printed regular halftone textures. (b) The captured printed irregular halftone textures.

used to generate the binary mask image. Then, the binary mask image and captured gray level image are used to calculate the centroids of dot clusters.

Next, we calculate lattice points according to the following

$$\begin{bmatrix} L_1 \\ L_2 \end{bmatrix} = \mathbf{N} \begin{bmatrix} t_1 \\ t_2 \end{bmatrix} + \begin{bmatrix} \varepsilon_1 \\ \varepsilon_2 \end{bmatrix}, \tag{3.37}$$

where $(L_1\,, L_2)^T$ is the coordinate of the lattice point, N is the periodicity matrix of halftone textures, $(t_1\,, t_2)^T$ is the integer scalars, and $(\varepsilon_1\,, \varepsilon_2)^T$ is the coordinate of the top left centroid.

The results are shown in Fig. 3.18 and Fig. 3.19. In Fig. 3.18 (a) and (b), we use red cross to mark centroids of dot clusters, and green cross to mark lattice points. In Fig. 3.18 (a), centroids and lattice points of regular digital halftone textures all fall on the same location. However, difference in the location of centroids and lattice points of irregular halftone textures shown in Fig. 3.18 (b) can be observed.

On the other hand, we use red cross to mark centroids of dot clusters, and green cross to mark lattice points in the binarized captured printed halftone textures. It is shown in Fig. 3.19. In Fig. 3.19 (a), the location of centroids of dot clusters are different from the location of lattice points when regular halftone textures are printed, which would not be the case for digital halftone textures. In Fig. 3.19 (b), it shows a significant difference between the location of centroids of dot clusters are different from the location of lattice points when irregular halftone textures are printed.

To quantify the difference between digital halftone textures and printed halftone textures, we find the disparity between centroids of dot clusters and lattice points by calculating the average of Euclidean distance between all centroids and lattice points. The results of digital halftone textures are shown in Table 3.3 in unit of printer pixels. The results of binarized captured printed halftone textures are shown in Table 3.4 in unit of printer pixels. A printer pixel is equal to 7663/812.8 camera pixels. As we can see from these two Tables, the disparity is larger when the digital halftone textures are printed. In addition, another statistic, percentage error of distance, is obtained

by as error divides by the square root of the area of the microcell. The area of the microcell is the determinant of the periodicity matrix.

In this section, we found out that the disparity of centroids of dot clusters and lattice points in the irregular halftone textures are more different than in regular halftone textures according Table 3.3. Moreover, the disparity of centroids of dot clusters and lattice points in the binarized captured printed irregular halftone textures is increased according to Table 3.4.

We also are interested in the disparity of centroids of dot clusters and lattice points in the real-world irregular halftone textures, which is shown in Fig. 3.21 (c) and Fig. 3.22 (c). However, the periodicity matrix of irregular halftone textures (HP Indigo) is unknown. A least square fit is conducted to find the corresponding periodicity matrix.

Given coordinates of centroids $\mathbf{X}_1, \mathbf{X}_2, \ldots, \mathbf{X}_N$, we want to minimize the following optimization problem

$$minimize\ E = \sum_{i=1}^{N} ||\mathbf{X}_i - \widetilde{\mathbf{X}}_i||^2 , \tag{3.38}$$

where $\widetilde{X}_i$ is the *i-th* lattice point, which is associated with X_i. The lattice point $\widetilde{X}_i$ is defined as

$$\widetilde{\mathbf{X}}_i = \mathbf{N}\mathbf{t}_i + \mathbf{e} , \tag{3.39}$$

where the parameter $\mathbf{N}$ is the periodicity matrix (which is unknown), $\mathbf{t_i}$ is a vector and $\mathbf{e}$ is the offset. To solve this optimization problem, we need to know the $\mathbf{t_i}$ that is associated with $\widetilde{X}_i$. To obtain $\mathbf{t_i}$, we first find an initial guess of the periodicity matrix $\mathbf{N}_{ini}$. We pick three centroids in Fig. 3.21 (c), and these three points can generate an initial guess of the periodicity matrix $\mathbf{N}_{ini}$. In the experiment, the initial periodicity matrix is

$$\mathbf{N}_{ini} = \begin{bmatrix} 3.53 & -2.2 \\ 2.2 & 3.53 \end{bmatrix} . \tag{3.40}$$

Table 3.3
Location disparity between centroids and lattice points of regular and irregular digital halftone textures in unit of printer pixels, and the percentage error of distance

	Regular	Irregular	Irregular (HP)
Error	0	0.0051	0.01
Percentage error of distance	0	0.12%	0.24%

As we know the coordinates of centroids and the periodicity matrix $\mathbf{N}_{ini}$, we can obtain $\mathbf{t}_i$ from Eq. 3.39.

Then, we can infer the unknown periodicity matrix $\mathbf{N}$. Given centroids $(x_1, y_1)^T$, $(x_2, y_2)^T$, $\ldots$, $(x_N, y_N)^T$ and, for very i, $(k_i, t_i)^T$ is known, we want to solve

$$min\ E = \sum_{i=1}^{N} (x_i - \widetilde{x_i})^2 + (y_i - \widetilde{y_i})^2 \,. \tag{3.41}$$

According to the lattice theory, we have

$$\begin{bmatrix} \widetilde{x_i} \\ \widetilde{y_i} \end{bmatrix} = \begin{bmatrix} a_{11} & a_{12} \\ a_{21} & a_{22} \end{bmatrix} \begin{bmatrix} k_i \\ t_i \end{bmatrix} + \begin{bmatrix} \varepsilon_1 \\ \varepsilon_2 \end{bmatrix} , \tag{3.42}$$

We take the partial derivative of Eq. 3.41 to 6 unknown parameters (i.e., a_{11}, a_{12}, a_{21}, a_{22}, ε_1 and ε_2) and are set to 0. By solving these 6 equations, we obtain the unknown periodicity $\mathbf{N}$ as

$$\mathbf{N} = \begin{bmatrix} 3.6 & -2.25 \\ 2.25 & 3.6 \end{bmatrix} . \tag{3.43}$$

According to Fig. 3.18, Fig. 3.19, Table 3.3 and Table 3.4, we can the disparity of the actual irregular halftone textures is larger than another halftone textures.

3.4.2 Area of the Regular and Irregular Dot Clusters

In this section, we find the area of each dot cluster in the digital halftone textures and binarized captured printed halftone textures. We use examples in Fig. 3.21, which

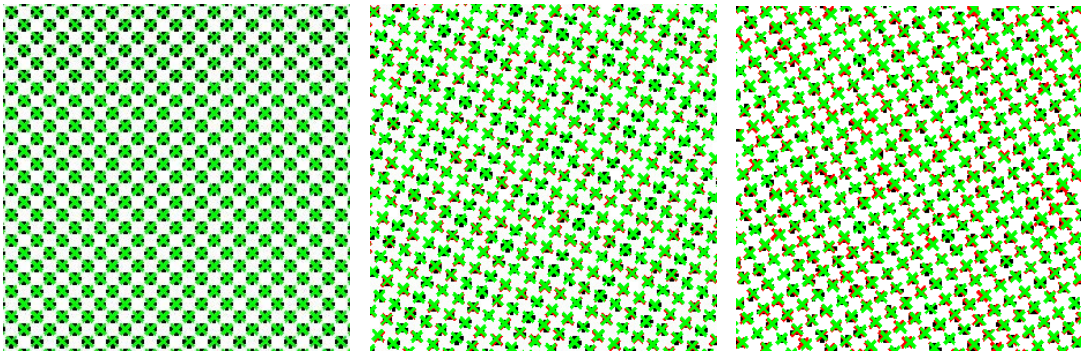

(a) (b) (c)

Fig. 3.18. In the figure, we mark the centroid of each dot cluster red cross, and mark the lattice point generated by the periodicity matrix of regular and irregular halftone textures green cross. (a) The location of all centroid of dot clusters and the location of lattice points fall on the same position. (b) A difference between the location of centroids and lattice points can be observed. (c) The difference between the location of centroids and lattice points in actual halftone textures is obvious.

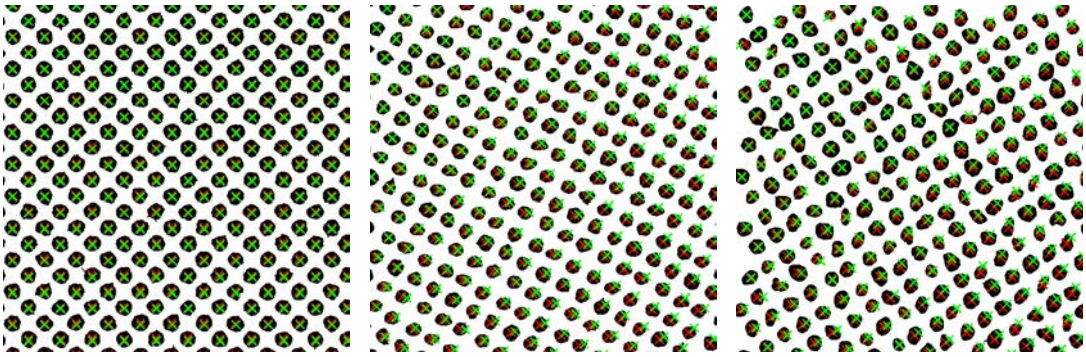

(a) (b) (c)

Fig. 3.19. In the figure, we mark the centroid of each dot cluster in the binarized captured printed halftone textures red cross, and mark the lattice points generated by the periodicity matrix of regular and irregular screens green cross. (a) The location of centroid of dot clusters and the location of lattice points have slightly difference. (b) A significant difference between the location of centroids and lattice points can be observed. (c) The difference between the location of centroids and lattice points in actual halftone textures is obvious.

are three different digital halftone textures, and Fig. 3.22, which are three different captured printed halftone textures. Figure 3.21 (c) and Fig. 3.22 (c) show a real digital irregular halftone textures and captured printed halftone textures. We can see the halftone textures shown in Fig. 3.21 (c) are more irregular than the irregular halftone textures shown in Fig. 3.21 (b). For captured printed halftone textures, we also have to binarize the captured image, and the binarized captured image can be used to find the area of each dot cluster. The connected component analysis [15] was applied to group pixels into connected sets. We use a 8-connected components in our experiment. To find the area of each dot cluster, number of pixels in each dot cluster is calculated. Figure 3.20 shows three examples to illustrate the way of counting area of a given dot cluster.

Histograms of digital dot-cluster area and binarized captured printed dot-cluster area are shown in Fig. 3.23 and Fig. 3.24. In addition to the mean and standard deviation of the histogram, we use normalized standard deviation (NSTD), which is defined as the ratio of standard deviation and the square root of the mean area. This statistic is independent of the area of dot cluster. In Fig. 3.23 (a), the histogram of the regular dot-cluster area has mean 5, standard deviation 0 and NSTD 0. In Fig. 3.23 (b), the histogram of the irregular dot-cluster area has mean 4.11, standard deviation 0.31 and NSTD 0.15. In Fig. 3.23 (c), the histogram of another irregular dot-cluster area has mean 3.93, standard deviation 0.72 and NSTD 0.37. We can

Table 3.4
Location disparity between centroids and lattice points of binarized captured printed regular and irregular halftone textures in unit of printer pixels, and the percentage error of distance

	Regular	Irregular	Irregular (HP)
Error	0.013	0.042	0.05
Percentage error of distance	0.03%	0.1%	0.12%

(a)

(b)

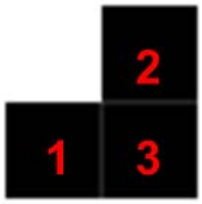

(c)

Fig. 3.20. Illustration of counting area of a dot cluster. (a) Area is equal to 5. (b) Area is equal to 3. (c) Area is equal to 3.

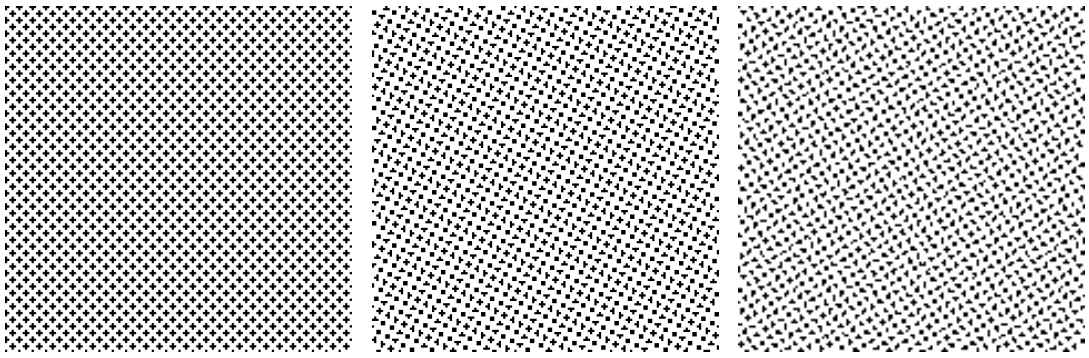

(a) (b) (c)

Fig. 3.21. Digital regular and irregular halftone textures used to find area of dot clusters. (a) The first example of regular halftone textures with tile vectors $\mathbf{n_1} = [3; 3]$ and $\mathbf{n_2} = [-3; 3]$. (b) The first example of irregular halftone textures with tile vectors $\mathbf{n_1} = [2; 11/3]$ and $\mathbf{n_2} = [-11/3; 2]$. (c) Irregular halftone textures provide by HP Indigo partners.

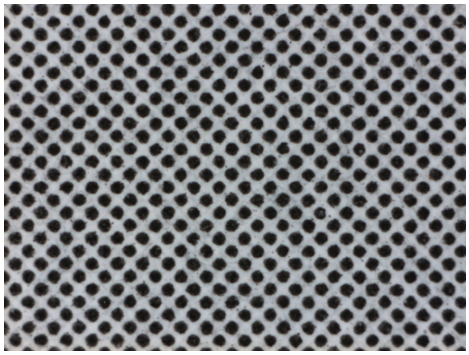

(a)

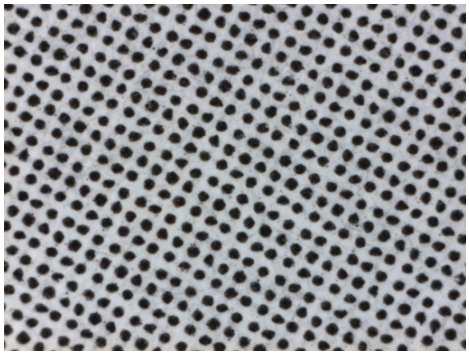

(b)

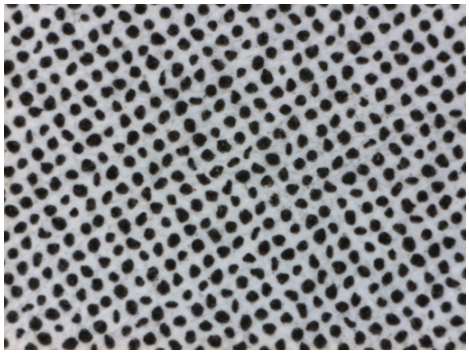

(c)

Fig. 3.22. Captured printed regular and irregular halftone textures. The digital halftone textures are printed by HP Indigo 5000 at 812.8 dpi, and then captured by QEA PIAS II at 7663 dpi. The image size is 768×1024. (a) The captured printed regular halftone textures. (b) The captured printed irregular halftone textures. ((b) The captured printed irregular halftone textures, which is provided by HP Indigo partners.)

observe that irregular halftone textures provided by HP Indigo partners have higher variance in the area of dot clusters according to the normalized standard deviation.

Figure. 3.24 (a) shows the histogram of the binarized captured printed regular dot-cluster area has mean 7.21, standard deviation 0.46 and NSTD 0.17. Figure. 3.24 (b) shows the histogram of the binarized captured printed irregular dot-cluster area has mean 5.49, standard deviation 0.64 and NSTD 0.27. Figure. 3.24 (c) shows the histogram of the binarized captured printed irregular dot-cluster area has mean 6.24, standard deviation 1.36 and NSTD 0.54. According to the results, we can observe that the NSTD of three histogram of binarized captured printed halftone textures are all increased due to the printing process.

3.4.3 Compactness of the Regular and Irregular Dot Clusters

In this section, we measure the compactness of the regular and irregular dot clusters. A compactness ratio is used to measure the compactness. The compactness measurement is considered is because a clustered-dot halftone algorithm wants to produce clustered-dot as compact as possible. Thus, we would like to compare the compactness of regular dot clusters and of irregular dot clusters. The compactness ratio is defined as $A/\pi R^2$, where A is the area of a dot cluster, and R is the radius of smallest circle which surround a dot cluster.

Histograms of digital dot-cluster compactness and binarized captured printed dot-cluster compactness are shown in Fig. 3.25 and Fig. 3.26. In Fig. 3.25 (a), the histogram of the regular dot-cluster compactness has mean 0.64 and standard deviation 0. In Fig. 3.25 (b), the histogram of the irregular dot-cluster compactness has mean 0.58 and standard deviation 0.06. In Fig. 3.25 (c), the histogram of the another irregular dot-cluster compactness has mean 0.5 and standard deviation 0.08. We can observe that irregular dot clusters provided by HP Indigo partners are less compact than the regular dot clusters and irregular dot clusters we generate.

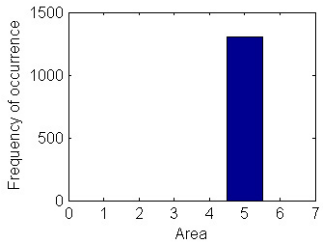

(a)

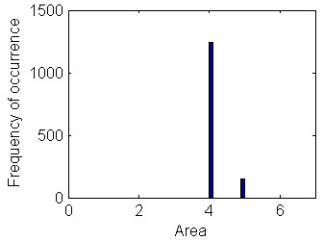

(b)

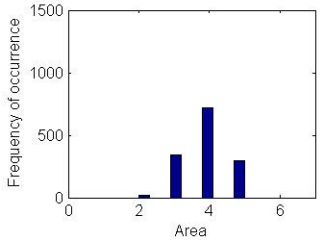

(c)

Fig. 3.23. Different histograms of the dot-cluster area in the regular and irregular digital halftone textures. In addition to the mean and standard deviation of the histogram, we use normalized standard deviation (NSTD), which is defined as the ratio of standard deviation and the square root of the mean area. (a) The histogram of the dot-cluster area in the regular halftone textures has mean 5, standard deviation 0 and NSTD 0. (b) The histogram of the area of dot clusters in the irregular halftone textures has mean 4.11, standard deviation 0.31 and NSTD 0.15. (c) The histogram of the dot-cluster area in the irregular halftone textures provided by HP Indigo partners has mean 3.93, standard deviation 0.72 and NSTD 0.37.

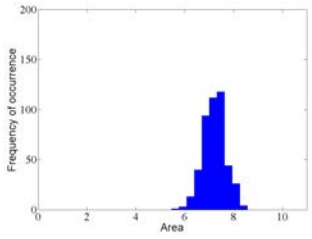

(a)

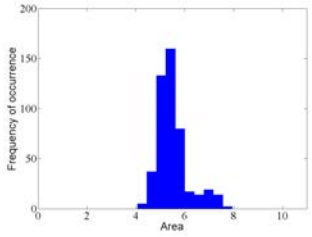

(b)

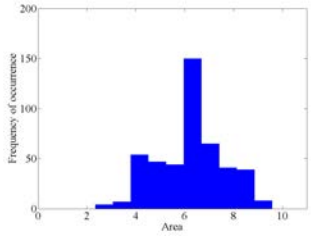

(c)

Fig. 3.24. Different histograms of the dot-cluster area in the regular and irregular binarized captured printed halftone textures. (a) The histogram of the dot-cluster area in the binarized captured printed regular halftone textures has mean 7.21, standard deviation 0.46 and NSTD 0.17. (b) The histogram of the binarized captured printed irregular dot-cluster area has mean 5.49, standard deviation 0.64 and NSTD 0.27. (c) The histogram of another binarized captured printed irregular dot cluster has mean 6.24, standard deviation 1.36 and NSTD 0.54.

Figure. 3.26 (a) shows the histogram of the binarized captured printed regular dot-cluster compactness has mean 0.8 and standard deviation 0.042. Figure. 3.26 (b) shows the histogram of the binarized captured printed irregular dot-cluster area has mean 0.76 and standard deviation 0.065. Figure. 3.26 (c) shows the histogram of another binarized captured printed irregular dot-cluster area has mean 0.72 and standard deviation 0.085. According to the results, we can observe that the compactness of binarized captured printed regular dot clusters is higher than the compactness of two binarized captured printed irregular dot clusters. However, we also observe that the printing processes increase the compactness of dot clusters.

3.5 Graininess Measurements on Different Substrates

In this section, we measure graininess on different substrates, and understand how the characteristics of the substrate affects graininess measurement. We consider two different substrates, glossy and polyester media. The polyester media we used is from TEKRA's Dura-Go® Polyester. In our experiment, 175 micron Clear Polyester is considered since it is the smoothest substrate provided by TEKRA. We choose the smoothest to eliminate graininess introduced by the substrate.

3.5.1 Experimental Setting and Captured Images

In the experiment, we print regular and irregular halftone pattern on glossy and polyester media. The tile vectors of the regular screen are: $\mathbf{n_1} = [3; 3]$ and $\mathbf{n_2} = [-3; 3]$. The screen angle and frequency of the regular screen are 45° and 191.4 line-per-inch (lpi), respectively. On the other hand, the irregular screen are provided by HP Indigo. The screen angle and frequency of the irregular screen are 31.88° and 192.06 (lpi), respectively. On the target, we print 10 different gray levels from 15 to 159 with increment 16 for both regular and irregular screen. The capture device is the Dyson Relay CMOS Imaging Device (Dr. CID) at 7946.85 dpi shown in Fig. 3.29.

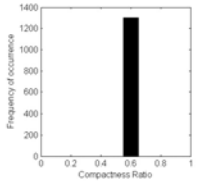

(a)

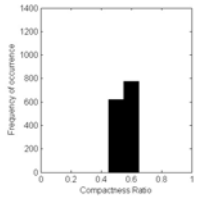

(b)

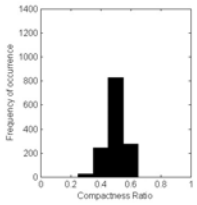

(c)

Fig. 3.25. Different histograms of compactness of regular and irregular dot clusters. (a) The histogram of the regular dot-cluster compactness has mean 0.64 and standard deviation 0. (b) The histogram of the irregular dot-cluster compactness has mean 0.58 and standard deviation 0.06. (c) The histogram of another irregular dot-cluster compactness has mean 0.5 and standard deviation 0.08.

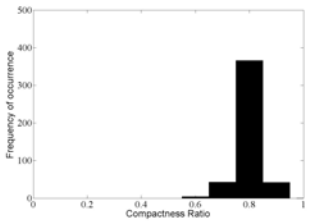

(a)

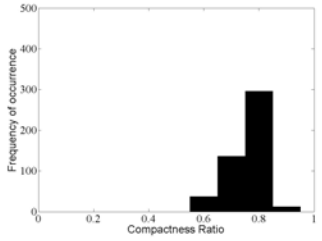

(b)

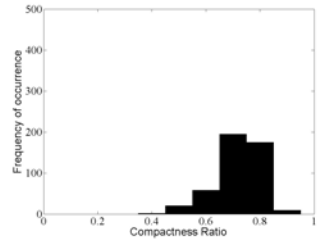

(c)

Fig. 3.26. Different histograms of compactness of binarized captured printed regular and irregular dot clusters. (a) The histogram of the binarized captured printed regular dot-cluster compactness has mean 0.8 and standard deviation 0.042. (b) The histogram of the binarized captured printed irregular dot-cluster compactness has mean 0.76 and standard deviation 0.065. (c) The histogram of another binarized captured printed irregular dot-cluster compactness has mean 0.72 and standard deviation 0.085.

To capture the halftone textures on the glossy media, we place the Dr. CID camera on top of the target, and the camera sensor captures images by recording the light, emitted by the internal white LED, reflects from the target surface. However, this scenario does not work on the polyester media. It is because the polyester media is transparent. To overcome this issue, we place the polyester media on top of a light box[1] shown in Fig. 3.30. Instead of capturing the light reflecting from the target surface, the camera sensor captures the light passing through the polyester media. The switch shown in Fig. 3.29 turns off when capturing the halftone textures on the polyester media, and turns on when capturing the halftone textures on the polyester media. In addition, there is a lighting effect when we capture the halftone textures on the glossy media using the internal white LED as shown in Fig. 3.27. To reduce the lighting effect, we only use the captured image in the red box as indicated in Fig. 3.27.

Figure. 3.28 shows a digital halftone image, a captured halftone image printed on glossy media and a captured halftone image printed on polyester media for both regular and irregular halftone textures at gray level 63. The size of these images are all 830×742. The captured images are all in camera RGB color space. Figure 3.28 (a) and (d) are the digital halftone image of regular and irregular pattern.Figure 3.28 (b) and (e) are the captured halftone patterns on the glossy media; and Figure 3.28 (c) and (f) are the captured halftone patterns on the polyester media. As we can see from the images capturing from the glossy media are quite different from the images capturing from the polyester media. This is because the light sources for these two kinds of images are different. To compensate the color difference issue and to compare graininess of two different images, calibration processes that transform the camera RGB to CIE XYZ are required.

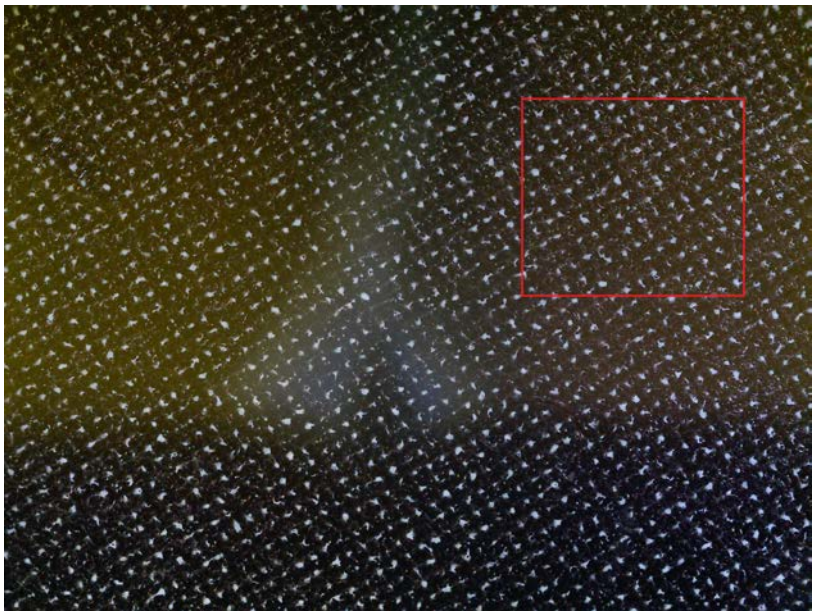

Fig. 3.27. The lighting effect appears when we use the internal white LED of the Dr. CID.

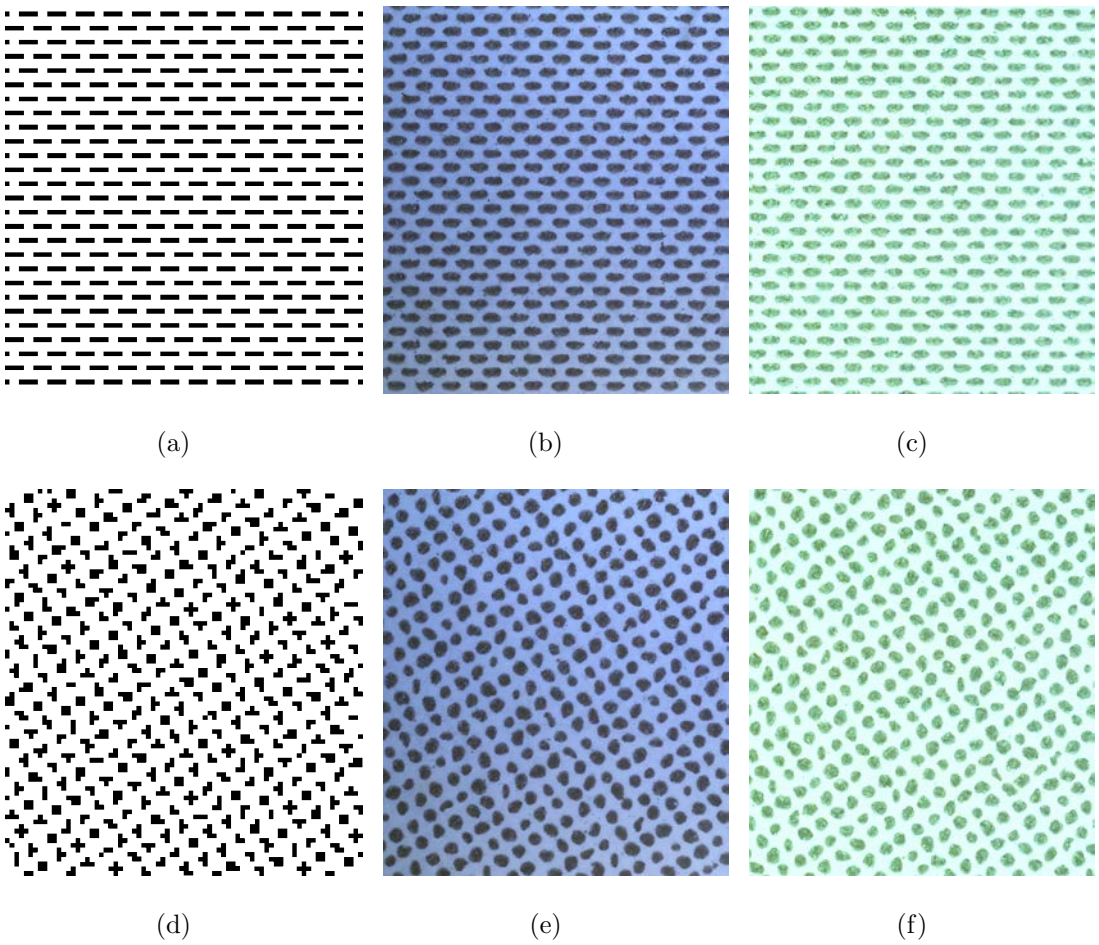

Fig. 3.28. (a) The digital halftone image of regular halftone pattern. (b) The captured regular halftone patterns on the glossy media. (c) The captured regular halftone patterns on the polyester media. (d) The digital halftone image of irregular halftone pattern. (e) The captured irregular halftone patterns on the glossy media. (f) The captured irregular halftone patterns on the polyester media.

3.5.2 Calibration for the Captured Halftone Textures on Glossy Media

To transform the camera RGB to CIE XYZ for the images capturing from the glossy media, we first have to transform the camera RGB to linear RGB by computing the gray balancing curves for the R, G and B channels. To obtain the gray balancing curves, we capture the 22 neutral gray scale patches on the Kodak IT8 4×5" target. However, there is lighting effect when we capture images using the internal white LED. To further reduce the lighting effect, a flat field method is considered. We first capture 20 white patches on the glossy media. Then, we average these white patches to get the averaged white patch. Each pixel of a neutral gray scale patch is divided by the corresponding pixel of the averaged white patch. Subsequently, the pixel of the resultant image is multiplied by 255 and each pixel value is rounded to integer value. Therefore, we have the flat-field-corrected gray patches. The R, G, and B values for each corrected gray patch are computed as the average of all the pixel values within each patch. The size of each gray patch is 400×400 for averaging. Then, the CIE Y value of each gray scale patch is measured by the X-Rite DTP70 Spectrophotometer under the default illuminant D65. Finally, the gray balancing curves can be approximated by a power law equation as follows

$$R_l \;=\; a(R/255)^b + c\,, \tag{3.44}$$

where $R_l = Y/100$, and R_l is the linearized R output value for a patch. Similarly, we can also find the parameters, a, b, and c for the G and B channels. The values of parameters, a, b, and c for the R, G and B channels for images on glossy media can be found in Table 3.5. The gray balancing curves for R, G and B channel for glossy media are shown in Fig. 3.32 (a)–(c).

Next, we find the transformation matrix M_{glossy} for transforming the linear RGB values to CIE XYZ values. We use the process mentioned above to obtain the linear

RGB values for the 228 color patches on the Kodak IT8 4 × 5" target. Then, the transformation matrix for glossy media, M_{glossy}, is given by

$$\begin{aligned} M_{glossy} &= (A^T A)^{-1} A^T X \\ &= \begin{bmatrix} 0.5512 & 0.3136 & 0.0649 \\ 0.6102 & 1.0208 & 0.2873 \\ 0.1294 & 0.0241 & 0.69 \end{bmatrix}, \end{aligned} \tag{3.45}$$

where matrix A (228 × 3) contains the 228 linear RGBs, and matrix X (228 × 3) contains the corresponding CIE XYZ values. Eq. (3.45) also shows the transformation matrix M_{glossy} for glossy media. Based on the above processing, we can transform the camera RGB to CIE XYZ. Finally, the CIE Y values are scaled to range from 0 (black) to 255 (white). Figure. 3.34 shows the calibration results for images capturing from the glossy media.

3.5.3 Calibration for the Captured Halftone Textures on Polyester Media

On the other hand, the calibration process for images capturing from the polyester media is different. Since the illuminant for capturing the halftone pattern on the polyester is from the light box, chromatic adaption transformation (CAT) is performed. Instead of using X-Rite DTP70 Spectrophotometer, we use Photo Research Spectroradiometer (SpectroScan 705)[2] as shown in Fig. 3.31. Chromatic adaption transformation (CAT) is used in imaging systems to map image appearance to colorimetry under different illumination sources [57]. The goal of a CAT algorithm is to have a linear transformation of a source color (X_S, Y_S, Z_S) to a destination color (X_D, Y_D, Z_D) by a transformation matrix $[M]$ that is dependent on the source reference white (X_{WS}, Y_{WS}, Z_{WS}) and the destination reference white (X_{WD}, Y_{WD}, Z_{WD}).

The relationship of a source color (X_S, Y_S, Z_S) and a destination color (X_D, Y_D, Z_D) is the following [57]

$$\begin{bmatrix} X_D \\ Y_D \\ Z_D \end{bmatrix} = [M] \begin{bmatrix} X_S \\ Y_S \\ Z_S \end{bmatrix} . \tag{3.46}$$

To perform the chromatic adaption transformation, we first have to linearly transform CIE XYZ into relative cone response domain (LMS) [57] by multiply a 3×3 matrix $[M_{CAT}]$. Then, Eq. (3.47) and Eq. (3.48) define the transformation from CIE XYZ to relative cone response domain for a source reference white and a destination reference white. Transformation matrix $[M]$ is defined according to Eq. (3.49)

$$\begin{bmatrix} L_S \\ M_S \\ S_S \end{bmatrix} = [M_{CAT}] \begin{bmatrix} X_{WS} \\ Y_{WS} \\ Z_{WS} \end{bmatrix} . \tag{3.47}$$

$$\begin{bmatrix} L_D \\ M_D \\ S_D \end{bmatrix} = [M_{CAT}] \begin{bmatrix} X_{WD} \\ Y_{WD} \\ Z_{WD} \end{bmatrix} . \tag{3.48}$$

$$[M] = [M_{CAT}]^{-1} \begin{bmatrix} L_D/L_S & 0 & 0 \\ 0 & M_D/M_S & 0 \\ 0 & 0 & S_D/S_S \end{bmatrix} [M_{CAT}] , \tag{3.49}$$

where the scaling is based on on the ratio of the cone response of the source and destination reference whites [57]. In our experiment, we choose the CAT based on CMCCAT 2000 [58], and the matrix $[M_{CAT}]$ is shown in Eq. (3.50).

The following is the calibration processes for images capturing from the polyester media. First, we measure the CIE XYZ value of the light emitted from the light box by

[1]Logan Electric, Texarkana, AR.
[2]Photo Research Inc., Chatsworth, CA.

using Photo Research Spectroradiometer (SpectroScan 705). Then, we transform the measured CIE Y of the light box white to transformed Y values that is measured under illuminant D65 that is the default illuminant of X-Rite DTP70 Spectrophotometer. As we have the transformation matrix $[M]$, we then find the gray balancing curves for R, G and B channel. To find the gray balancing curves, we place the Kodak IT8 4×5" transparency target on top of the light box, and measure the CIE XYZ values of the 22 gray level patches using Photo Research Spectroradiometer (SpectroScan 705). Afterward, we can apply CAT to the measured CIE Y of these gray patches to transformed CIE Y. On the other hand, we use Dr. CID to capture the 22 gray level patches on the target, which is on the light box, then we use these data to fit the gray balancing curve for each R, G and B channel based on the Eq. (3.44). The size of the patch using to average is 400×400. The values of parameters, a, b, and c for the R, G and B channels for images on polyester media can be found in Table 3.6. The gray balancing curves for R, G and B channel for polyester media are shown in Fig. 3.33 (a)–(c).

Next, we find the transformation matrix $M_{polyester}$ for transforming the linear RGB values to CIE XYZ values. We measure the CIE XYZ values of the 228 color patches on the Kodak IT8 4×5" transparency target by Photo Research Spectroradiometer (SpectroScan 705). Again, these measured CIE XYZ values are applied CAT to the transformed CIE XYZ. Then, Dr. CID is used to capture the 228 color patches on the Kodak IT8 4×5" transparency target. Based on Eq. (3.45), we can obtain the transformation matrix $M_{polyester}$ for polyester media, and $M_{polyester}$ is shown in Eq. (3.51). Figure. 3.35 shows the calibration results for images capturing from the polyester media.

$$[M_{CAT}] = \begin{bmatrix} 0.7982 & 0.3389 & -0.1371 \\ -0.5918 & 1.5515 & 0.0406 \\ 0.0008 & 0.0239 & 0.9753 \end{bmatrix}. \tag{3.50}$$

$$[M_{polyester}] = \begin{bmatrix} 0.3467 & 0.1901 & 0.076 \\ 0.6484 & 0.9644 & 0.4369 \\ 0.1021 & 0.0056 & 0.6899 \end{bmatrix} \tag{3.51}$$

Fig. 3.29. Dyson Relay CMOS Imaging Device (Dr. CID).

Fig. 3.30. Light box.

Fig. 3.31. Photo Research Spectroradiometer (SpectroScan 705).

Table 3.5
The parameters for the power law equation for each channel for images capturing from glossy media

	R	G	B
a	5.039×10^{-5}	4.137×10^{-4}	1.139×10^{-3}
b	2.566	2.18	1.982
c	-4.127	-2.372	2.223

Table 3.6
The parameters for the power law equation for each channel for images capturing from polyester media

	R	G	B
a	1.055×10^{-4}	5.3×10^{-6}	1.675×10^{-4}
b	2.489	2.915	2.349
c	-2.369	0.8057	-1.098

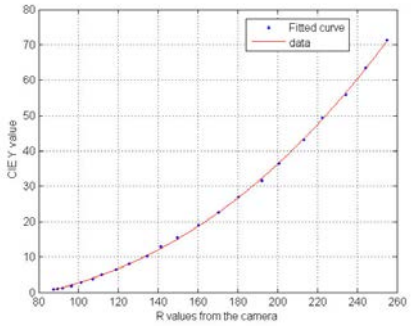

(a)

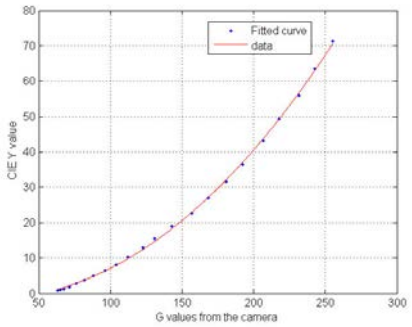

(b)

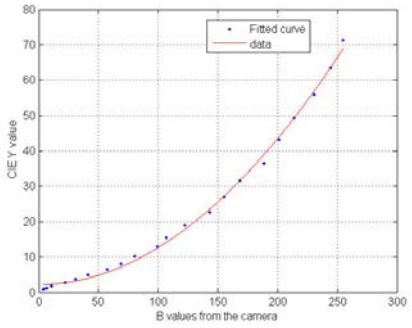

(c)

Fig. 3.32. (a) The gray balancing curve for R channel for the glossy media. (b) The gray balancing curve for G channel for the glossy media. (c) The gray balancing curve for B channel for the glossy media.

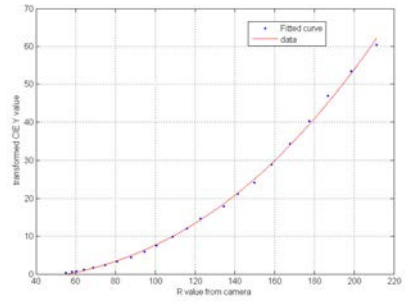

(a)

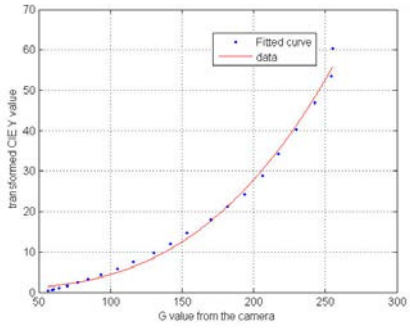

(b)

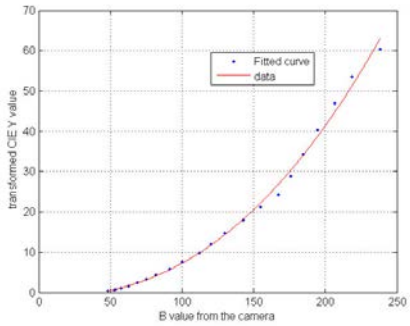

(c)

Fig. 3.33. (a) The gray balancing curve for R channel for the polyester media. (b) The gray balancing curve for G channel for the polyester media. (c) The gray balancing curve for B channel for the polyester media.

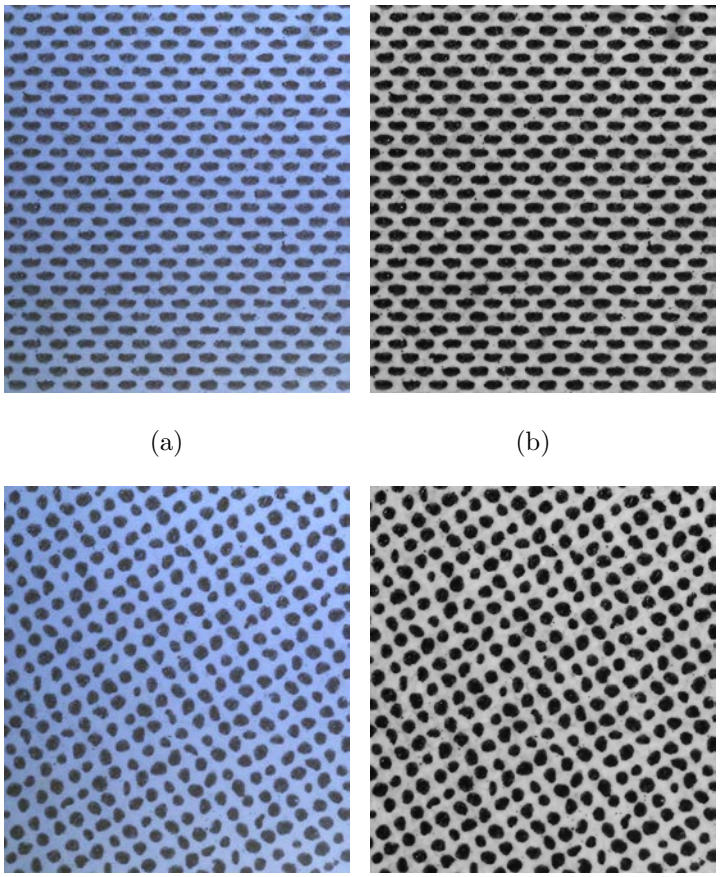

(a) (b)

(c) (d)

Fig. 3.34. The calibration results for images capturing from the glossy media. (a) A captured image of a regular halftone textures in camera RGB color space. (b) A calibrated image of a regular halftone textures in CIE Y. (c) A captured image of a irregular halftone textures in camera RGB color space. (b) A calibrated image of a irregular halftone textures in CIE Y.

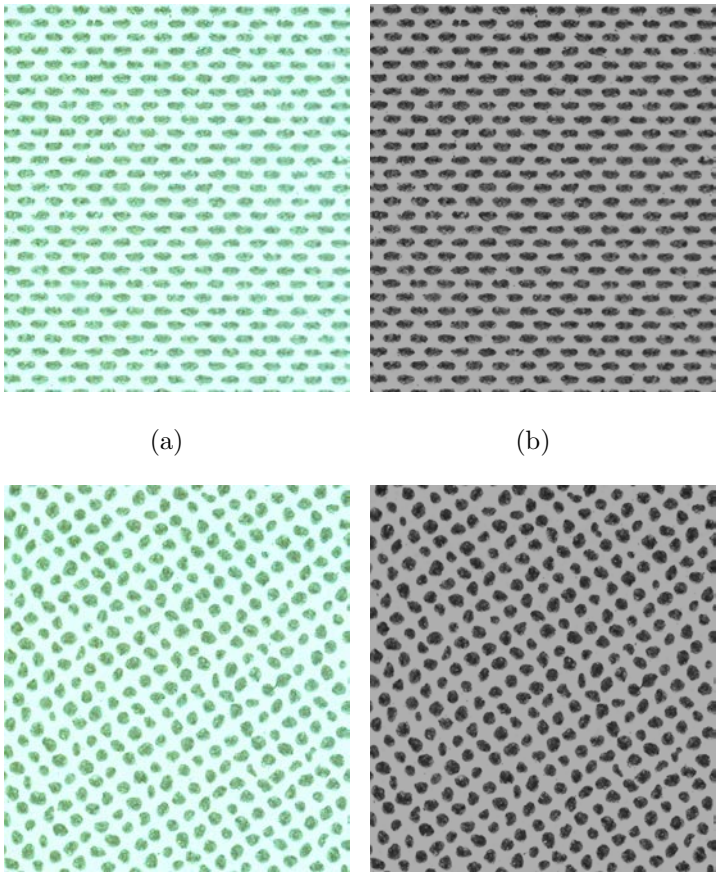

(a) (b)

(c) (d)

Fig. 3.35. The calibration results for images capturing from the polyester media. (a) A captured image of a regular halftone textures in camera RGB color space. (b) A calibrated image of a regular halftone textures in CIE Y. (c) A captured image of a irregular halftone textures in camera RGB color space. (b) A calibrated image of a irregular halftone textures in CIE Y.

3.5.4 Graininess Measurements

We perform two different experiments to understand how the property of the substrate affects the graininess measurement. First, we compare graininess of different halftone textures, regular and irregular that are on the same substrate either glossy or polyester. In our experiment, we apply Grainometer [59], a tool provided by HP Indigo partners to measure graininess of a given image. Figure. 3.36 (a) shows the graininess measurement between regular and irregular halftone textures on glossy media with different absorptance. In addition, Fig. 3.36 (b) shows the graininess measurement between regular and irregular halftone textures on polyester media with different absorptance. From these two plots, we can see that graininess of the irregular halftone pattern is higher than the graininess of the regular halftone pattern either glossy or polyester. In addition, the overall graininess of images capturing from the polyester media are lower than graininess of images capturing on the glossy media. This is because the polyester media is inherently smoother than the glossy media.

Second, we we compare graininess of the same halftone textures either regular or irregular, but they are on the different substrates. Figure. 3.37 (a) shows the graininess measurement between glossy and polyester media for regular halftone textures with different absorptance. In addition, Fig. 3.37 (b) shows the graininess measurement between glossy and polyester media for irregular halftone textures with different absorptance. From the results, we can see that smoothness of the substrate impacts graininess more when the absorptance is lower than 95/255. In addition, the print quality of halftone dots is better on glossy media than on the polyester media, and it might lead to the fact that the graininess of the printed pattern on the polyester media is higher than the graininess of the printed pattern on the glossy media when the absorptance is higher than 95/255.

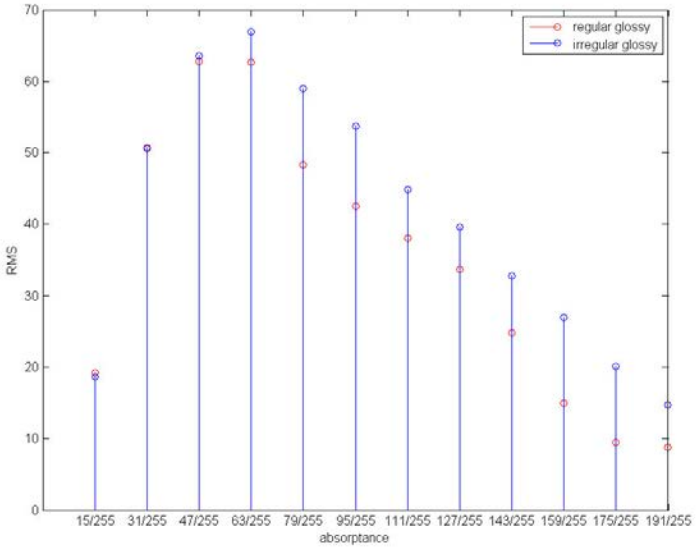

(a)

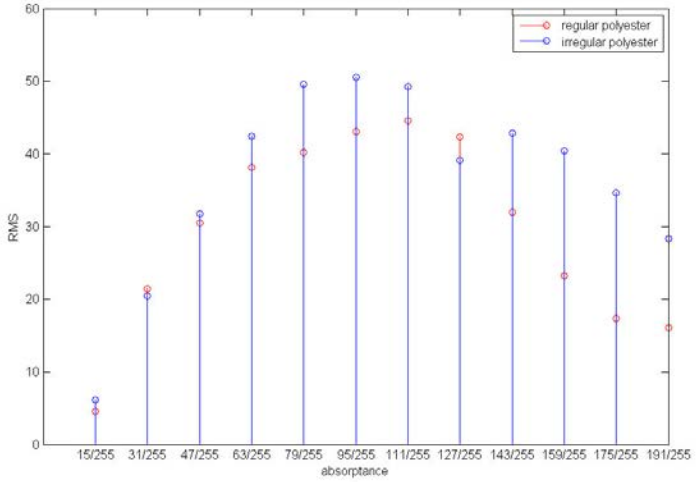

(b)

Fig. 3.36. (a) The graininess measurement between regular and irregular halftone textures on glossy media with different absorptance. (b) The graininess measurement between regular and irregular halftone textures on polyester media with different absorptance.

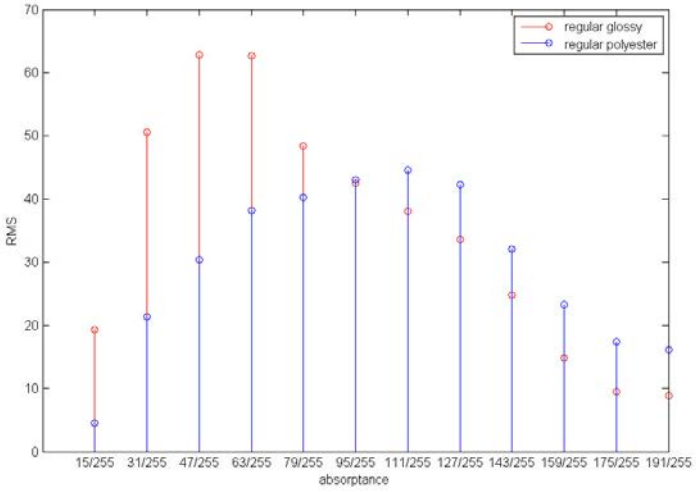

(a)

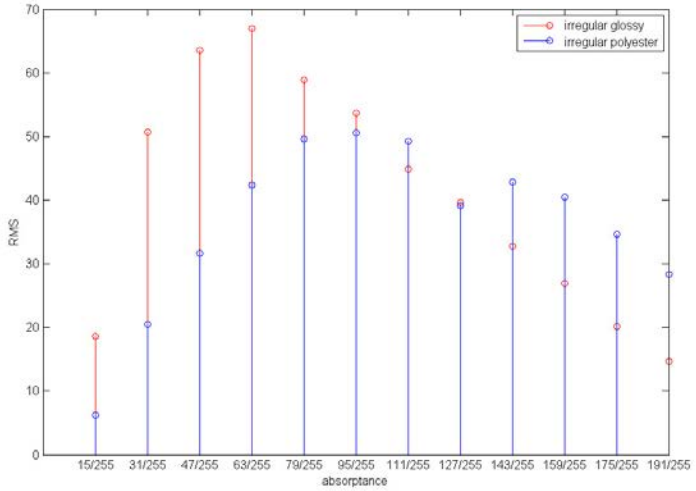

(b)

Fig. 3.37. (a) The graininess measurement between glossy and polyester media for regular halftone textures with different absorptance. (b) The graininess measurement between glossy and polyester media for irregular halftone textures with different absorptance.

3.6 Conclusions

With the emergence of high-end digital printing technologies, it is of interest to analyze the nature and causes of image graininess in order to understand the factors that prevent high-end digital presses from achieving the same print quality as commercial offset presses. In this chapter, we report on a study to understand the relationship between image graininess, and halftone technology and marking technology. First, we describe a Fourier-based analysis of regular and irregular periodic, clustered-dot halftone textures. With high-end digital printing technology, irregular screens can be considered since they can achieve a better approximation to the screen sets used for commercial offset presses. This is due to the fact that the elements of the periodicity matrix of an irregular screen are rational numbers. However, irregular halftone textures generate new frequency components near the spectrum origin; and these frequency components are low enough to be visible to the human viewer. On the other hand, regular halftone textures do not have these frequency components. Moreover, the metric for measuring nonuniformity of given halftone textures indicates that the nonuniformity of irregular halftone textures is higher than the nonuniformity of regular halftone textures. Next, a spatial-statistics-based analysis of regular and irregular periodic, clustered-dot halftone textures is conducted. The three spatial statistics, disparity between the centroids of dot clusters and lattice points, area of dot clusters and compactness of dot-clusters, indicate that irregular digital halftone textures have higher disparity between the location of centroids of dot clusters and lattice points, and have higher variance in the histogram of dot-cluster area. Moreover, the variance increases when the digital halftone textures are printed. In addition, the compactness measurement shows that irregular dot clusters are less compact than regular dot clusters. A clustered-dot halftone algorithm wants to produce clustered-dot as compact as possible. Even though the irregular digital dot cluster is less compact, the compactness of irregular printed dot cluster is increased because of the printing processes. Lastly, the experiments of graininess measurement on different

substrates are discussed. We print regular and irregular halftone textures on glossy and polyester media. From the experiments, we observed that the irregular printed halftone textures are grainier than regular printed halftone textures on both glossy and polyester media. In addition, the substrate characteristics affect graininess and the dot formation quality. Based on the analysis and experiments, we conclude that irregular halftone textures introduce image graininess in the spatial domain because of the non-integer elements of their periodicity matrix, and the finite addressability of the marking engine. In addition, the dot cluster shape of irregular halftone textures varies from dot to dot; and each dot cluster location of irregular halftone textures differs from each other, which would not be the case for regular halftone textures. Moreover, the irregular dot cluster is less compact. Finally, the marking technology provides inconsistency of print quality between substrates.

LIST OF REFERENCES

LIST OF REFERENCES

[1] P-J. Chiang, N. Khanna, A. K. Mikkilineni, M. V. O. Segovia, J. P. Allebach, G T. C. Chiu, and E. J. Delp, "Printer and Scanner Forensics: Models and Methods," in *Intelligent Multimedia Analysis for Security Applications*, H. T. Sencar, S. Velastin, N. Nikolaidis, S. Lian, eds. (Springer-Verlag, 2010), pp. 145–187.

[2] C.-L. Chen, G. T.-C. Chiu, and J. P. Allebach, "Banding Reduction in Electrophotographic Process Using Human Contrast Sensitivity Function Shaped Photoreceptor Velocity Control," J. Imaging Technol. **47**, 209–223 (2002).

[3] Y. Bang, Z. Pizlo and J. P. Allebach, "Banding Assessment with Controlled Halftoning: The Ten Printer Experiment," J. Imaging Technol. **50**, 522–529 (2006).

[4] O. Arslan, Z. Pizlo, and J. P. Allebach, "Softcopy banding visibility assessment," J. Imaging Technol. **5**, 271–28 (2007).

[5] G. Lin, J. Grice, and J. Allebach, "Banding Artifact Reduction in Electrophotographic Printers by Using Pulse Width Modulation," J. Imaging Technol. **46**, 326–337 (2002).

[6] H. Horikawa, I. Sugisaki, and M. Tashiro, "Relationship between fluctuation in mirror radius (within one polygon) and the jitter," Proc. SPIE **1454**, 46 (1991).

[7] G. Stutz, "Eliminating laser scanner artifacts in binary and continuous tone printing," Proc. SPIE **2383**, 427 (1995).

[8] A. H. Eid, M. N. Ahmed, and E. E. Rippetoe, "EP printer jitter characterization using 2D gabor filter and spectral analysis," in Proceedings of IEEE Conference on Image Processing (IEEE, 2008), pp. 1860.

[9] A. H. Eid, M. N. Ahmed, B. E. Cooper, and E. E. Rippetoe, "Characterization of Electrophotographic Print Artifacts: Banding, Jitter, and Ghosting," IEEE Trans. on Image Processing **20**, 1313–1326 (2011).

[10] Y.-T. Chen, T. Nelson, T. Ogle, H. Ren, M. Shaw, and J. P. Allebach, "Laser Scanner Jitter Characterization," Proc. of IS&T's NIP and Digital Fabrication Conference (IS&T, 2013), pp. 281–285.

[11] S. Haykin, *Communication System* (John Wiley & Sons, 2001).

[12] T. S. Rao, G. R. Arce and J. P. Allebach, "Analysis of ordered dither for arbitrary sampling lattices and screen periodicities," IEEE Trans. Acoustics, Speech, and Signal Processing **38**, 1981–2000 (1990).

[13] T.-C Chang, J. P. Allebach, "A New Framework for Characterization of Halftone Textures," IEEE Trans. on Image Processing **15** 1285–1299 (2006).

[14] N. Otsu, "A threshold selection from gray level histograms," IEEE Trans. Systems, Man and Cybernetics **9**, 62–66 (1979).

[15] A. Rosenfeld and A. C. Kak, *Digital Picture Processing* **2** (Academic, 1982).

[16] H. Santos-Villalobos, H. J. Park, R. Kumontoy, K. Low, M. Ortiz, J. P. Allebach, C. Kim, P. Choe, S. Leman, K. Oldenburger, M. Lehto and X. Lehto, "Web-based diagnosis tool for customers to selfsolve print quality issues," J. Imaging Sci. Technol. **54**, 1–13 (2010).

[17] W. Jang, M.-C. Chen, J. P. Allebach and G. T.-C. Chiu, "Print quality test page," J. Imaging Sci. Technol. **48**, 432–446 (2004).

[18] P. Goyala, M. Guptaa, C. Staelinb, M. Fischerb, O. Shachamc, T. Kashtic and J. P. Allebach, "Electrophotographic model based stochastic clustered-dot halftoning with direct binary search," Proc. IEEE Int'l. Conf. Image Processing (IEEE, Brussels, Belgium, 2011) pp. 1721–1724.

[19] Q. Lin, "Adaptive halftoning based on image content," US Patent 5,970,178 (1999).

[20] K. Kritayakirana, D. R. Tretter and Q. Lin,"Adaptive Halftoning Method and Apparatus," US Patent 6,760,126 (2004).

[21] J. Huang and A. Bhattacharjya, "An adaptive halftone algorithm for composite documents," Proc. SPIE **5293**, 425–433 (2004).

[22] H. Z. Hel-Or, X. M. Zhang and B. A. Wandell, "Adaptive cluster dot dithering," J. Electron. Imaging **8**, 133 (1999).

[23] S. J. Park, M. Shaw, G. Kerby, T. Nelson, D.-Y. Tzeng, V. Loewen, K. Bengtson and J. P. Allebach, "Halftone blending between smooth and detail screens to improve print quality with electrophotographic printers," Proc. SPIE **8292** 829210–829210–12 (2012).

[24] A. L. Oakley and A. C. Norris, "Page description languages: development, implementation and standardization," Electron. Publishing Origination, Dissemination and Design **1**, 79–96 (1988).

[25] W. S. Lovegrove and D. F. Brailsford, "Document analysis of pdf files: methods, results and implications," Electron. Publishing Origination, Dissemination and Design **8**, 207–220 (1995).

[26] Adobe Systems Incorporated, Portable Document Format Reference Manual (Addison-Wesley, Massachusetts, 2006).

[27] P.-J. Chiang, N. Khanna, A. K. Mikkilineni, M. V. O. Segovia, J. P. Allebach, G. T.-C. Chiu and E. J. Delp, "Printer and scanner forensics: models and methods," *Intelligent Multimedia Analysis for Security Applications*, edited by H. T. Sencar, S. Velastin, N. Nikolaidis, and S. Lian, (Springer-Verlag, Berlin, 2010), pp. 145–187, ISBN: 978-3-642-11754-1.

[28] C. Lee and J. P. Allebach, "The hybrid screen–improving the breed," IEEE Trans. Image Process. **19**, 435–450 (2010).

[29] F. Shafait, D. Keysers and T. M. Breuel, "Performance evaluation and benchmarking of six page segmentation algorithms," IEEE Trans. Pattern Analysis and Machine Intelligence **30**, 941–954 (2008).

[30] D. Keysers, F. Shafait and T. M. Breuel, "Document image zone classification – a simple high-performance approach," Proc. the Second Int'l. Conf. on Computer Vision Theory and Applications (INSTICC, Barcelona, Spain, 2007) pp. 44–51.

[31] P. Shadkami and N. Bonnier, "Watershed based document image analysis," Proc. the 12th Int'l. Conf. Advanced Concepts for Intelligent Vision Systems, Part I (SEE, Sydney, Australia, 2010) pp. 114–124.

[32] M. A. Moll, H. S. Baird and C. An, "Truthing for pixel-accurate segmentation," Proc. the 8th IAPR International Workshop on Document Analysis Systems (IEEE, Nara, Japan, 2008) pp. 379–385.

[33] H. Cheng and C. A. Bouman, "Multiscale bayesian segmentation using a trainable context model," IEEE Trans. Image Process. **10**, 511–525 (2001).

[34] C. S. Won, "Image extraction in digital documents," J. Electron. Imaging **17**, 1 (2008).

[35] M. Sezer Erkilinc, M. Jaber, E. Saber, P. Bauer and D. Depalov, "Text, photo, and line extraction in scanned documents," J. Electron. Imaging **21**, 033006 (2012).

[36] P. Chiu, F. Chen and L. Denoue, "Picture detection in document page images," Proc. the 2010 ACM Symposium on Document Engineering (ACM, Manchester, United Kingdom, 2010) pp. 211–214.

[37] Y.-T. Chen, D.-Y. Tzeng, T. Nelson, M. Shaw and J. P. Allebach,"Segmentation for better rendering of mixed-content pages," Proc. SPIE **8652**, 865209-865209-15 (2013).

[38] J. Shi and J. Malik, "Normalized cuts and image segmentation," IEEE Trans. Pattern Analysis and Machine Intelligence **22**, 511–525 (2000).

[39] E. Bernal, J. P. Allebach and J. Trask, "Model-based memory-efficient algorithm for compensation of toner overdevelopment in electrophotographic printers," J. Imaging Sci. Technol. **52**, 1–15 (2008).

[40] J. L. Trask, "Trapping methods and arrangements for use in printing color images," US Patent 6,549,303 (2004).

[41] H. Wang, M. Boutin, J. L. Trask, and J. P. Allebach, "A Joint Color Trapping Strategy for Raster Images," Proc. SPIE **7528**, 75280C–1–12 (2010).

[42] J. Canny, "A computational approach to edge detection," IEEE Trans. Pattern Analysis and Machine Intelligence **8**, 679–698 (1986).

[43] D. Marr and E. Hildreth, "Theory of edge detection," Proc. the Royal Society of London **207**, 187–217 (1980).

[44] R. Achanta, S. Hemami, F. Estrada, and S. Susstrunk, "Frequency-tuned salient region detection," Proc. IEEE Int'l. Conf. Computer Vision and Pattern Recognition (IEEE, Miami Beach, FL, 2009) pp. 1597–1604.

[45] X. Dong, K.-L. Hua, P, Majewicz, G. McNutt, C. A. Bouman, J. P. Allebach, I. Pollak, "Document page classification algorithms in low-end copy pipeline," J. Electron. Imaging **17**, 043011 (2008).

[46] R. M. Haralick, S. R. Sternberg, and X. Zhuang, "Image analysis using mathematical morphology," IEEE Trans. Pattern Analysis and Machine Intelligence **9**, 532–550 (1987).

[47] B. Tagansky, "Ink Development in HP Indigo Digital Presses," in Proceedings of IS&T's NIP and Digital Fabrication Conference (SPIE, 2008), pp. 799–802.

[48] S. G. W. C. Haines and K. Knox, "Digital Color Halftones," in Digital Color Imaging Handbook. Boca Raton, FL: CRC Press, 2002, pp. 385-490.

[49] P. Li and J. P. Allebach, "Tone-dependent error diffusion," IEEE Trans. Image Process. **13**, 201–215 (2004).

[50] D. J. Lieberman and J. P. Allebach, "A Dual Interpretation for Direct Binary Search and Its Implications for Tone Reproduction and Texture Quality," IEEE Trans. on Image Process. **9** 1950–1963 (2000).

[51] H. Mizes, "Graininess of Color Halftones," Proc. of NIP and Digital Fabrication Conference (IS&T, 2000), pp. 396–399.

[52] ISO (1996) International Organization for Standardization: Draft of International Standard ISO 13660.

[53] C. Tang, A. Veisb, R. Ulichney and J. Allebach, "Irregular Clustered-Dot Periodic Halftone Screen Design," Proc. SPIE **9015**, (2014).

[54] B. Mishra and Rene Rasmussen, "MicroUniformity: An Image Quality Metric For Measuring Noise," Proc. of Image Process., Image Quality, Image Capture, Systems Conference (IS&T, 2000), pp. 75–78.

[55] P. Kane and R. Cookingham, "A Color Grain Ruler for the Measurement of Print Graininess," Proc. of Image Process., Image Quality, Image Capture, Systems Conference (IS&T, 1998), pp. 192–195.

[56] S. H. Kim and J. P. Allebach, "Impact of HVS Models on Model-Based Halftoning," IEEE Trans. on Image Process. **11** 258–269 (2002).

[57] S. E. Susstrunk, J. M. Holm, and G. D. Finlayson, "Chromatic adaptation performance of different RGB sensors," Proc. SPIE **4300**, 172–183 (2001).

[58] C. Li, M. R. Luo and B. Rigg, "Simplification of the CMCCAT97," Proc. of Color and Imaging Conference (IS&T, 2000), pp. 56–60.

[59] O. Haik, T. Frank, T. Kashti, S. Moalem, I. Federman, R. Dagan, O. Perry and D. Kella, "Grainometer: A Novel Image Graininess Estimator," HP TechCon (2012).

[60] N. Otsu, "A threshold selection method from gray-level histograms". IEEE Trans. Sys., Man., Cyber. **9** 62–66 (1979).

VITA

VITA

Yi-Ting Chen received his B.S. degree in electronic engineering from National Chiao Tung University, Hsinchu, Taiwan, in 2009. He is currently pursuing his Ph.D. degree in electrical and computer engineering at Purdue University. His current research interests include digital image processing, color science, and digital imaging.